High-fidelity Modelling of an Electric Sport Utility Vehicle

by

Shinhoon Kim

A thesis
presented to the University of Waterloo
in fulfillment of the
thesis requirement for the degree of
Master of Applied Science
in
Systems Design Engineering

Waterloo, Ontario, Canada, 2015

I hereby declare that I am the sole author of this thesis. This is a true copy of the thesis, including any required final revisions, as accepted by my examiners.

I understand that my thesis may be made electronically available to the public.

Abstract

The development and validation of a high-fidelity dynamic model of an electric sport utility vehicle (SUV) is presented. The developed model of the electric vehicle system consists of two main subsystems: the high-fidelity vehicle dynamics model, and the high-fidelity electrical powertrain subsystem that is comprised of an alternating-current (AC) electric motor, a 3-phase inverter, and motor controllers. The high-fidelity models are developed in MapleSim and Simulink. Specifically, the high-fidelity vehicle dynamics model is developed using the MapleSim multibody and tire dynamics libraries. A simple longitudinal model is developed in Simulink to cross-validate the high-fidelity MapleSim model by comparing the vehicle dynamics responses of the two models.

The electrical powertrain components are developed and implemented in the following order: the AC electric motor is developed first followed by the 3-phase voltage source inverter. Motor controllers are developed next, and lastly the electrical powertrain subsystem is assembled by combining the AC electric motor, the 3-phase inverter, and the motor controllers. Previous research results and literature on AC electric motors are studied thoroughly to develop an AC electric motor model suitable for electric vehicle applications. The 3-phase voltage source inverter is developed to convert a constant voltage signal into 3-phase AC voltage signals that are used by the AC electric motor. Lastly, the motor controllers are designed to control the electric motor responses, such as developed motor torque or speed. At each stage of the powertrain component model developments, the developed models are verified by studying their simulation results. Experimental motor data from vehicle testing is available, so the experimental torque-speed curves are used to tune the AC electric motor parameters.

Once all the individual components are developed and validated, the high-fidelity electric vehicle system is created in Simulink by assembling the MapleSim vehicle dynamics model and the electrical powertrain subsystem which is developed in Simulink. For the models developed in MapleSim, they are exported as Simulink blocks so that they could be run alongside with the Simulink models. A driver controller is included to calculate required reference motor torque to track a reference speed input. A brake module is designed to simulate a brake system found in an electric vehicle where regenerative and mechanical brake systems cooperate to deliver braking torque. The electric vehicle system model is simulated using the driving cycles that represent city, highway, and aggressive driving scenarios. The simulation results, such as the vehicle's longitudinal speed and developed motor torque and currents, are presented and studied to verify that the electric vehicle system can operate under different driving scenarios.

Acknowledgements

I would like to thank ...

my supervisors Prof. Nasser Lashgarian Azad and Prof. John McPhee for their guidance and financial support throughout this work.

Dr. Joydeep Banerjee for his expertise and kindness when helping me with the MapleSim implementations.

Dr. Andrew Hall for his help with the vehicle dynamics aspect of this work and his thoughtful advice on making this work better.

All members of the Motion Research Group (MORG) for providing me valuable feedback during weekly meetings.

and, last but not least, my parents and my brother for their support and encouragement.

Dedication

To my family

Table of Contents

7 Conclusions   **85**

List of Tables

List of Figures

Chapter 1

Introduction

This chapter explains the thesis's main problem statement and the research objectives. The key approaches taken to complete the research are discussed, and it is followed by the organization of the thesis. The benefits of building an electric vehicle's prototype in modelling and simulation environments are briefly explained.

1.1   Problem statement

Electric vehicles are viewed as environmental-friendly and alternative fuel vehicles in today's automobile industry. They have more efficient drivetrain components compared to a vehicle with an internal combustion engine (ICE). For example, electric motors are energy efficient and lighter than ICEs, and electric vehicles generally have smaller and lighter transmission components than ICE powered vehicles. The main disadvantage of electric vehicles is the energy storage component which is a rechargeable battery. Most consumer electric vehicles use rechargeable batteries as the main energy storage component, and a large number of battery cells are needed in electric vehicles to get a similar driving range to ICE powered vehicles. Since the utilization of rechargeable batteries greatly influences the overall cost and the driving range of electric vehicles, there have been extensive contributions from the academic and industrial communities to develop affordable and long-range electric vehicles by using different types of batteries or reducing the number of batteries used in a vehicle. Battery research activities have been very successful at improving the energy density of battery cells. Plans to increase the manufacturing capacities of battery factories will serve to reduce the cost of cells, and therefore the cost of electric vehicles. It can be foreseen that battery-powered electric vehicles will play an important role in the future of the automotive industry

with the potential launch of long-range electric vehicles with a competitive price tag. Hydrogen-fuel powered electric vehicles have emerged as an alternative electric vehicle that overcomes the disadvantages of battery-powered electric vehicles by using hydrogen gas and fuel cells to produce electricity. But, hydrogen gas refuelling stations are not widely available, and there are safety doubts about storing a hydrogen gas in a highly pressurized hydrogen gas tank located in a vehicle.

An electric vehicle's configuration is dependent on the available powertrain components, such as electric motors, batteries, and powertrain controllers. The latest battery-powered electric vehicles use lithium-ion battery cells, but if improved and more energy dense battery cells become commercially available in the near future, the next generation of electric vehicles will be equipped with different types of battery cells. Different types of electric motors are also currently available for electric vehicle applications, such as direct-current (DC) electric motors, and AC synchronous and asynchronous electric motors. Electric vehicle engineers and designers should consider advantages and disadvantages of each powertrain component to design the electrical powertrain system which is efficient, powerful, and commercially viable in terms of cost. Physical prototypes can be built to test different combinations of components, but it will be a time-consuming and expensive exercise. Using high-fidelity mathematical models to build an electric vehicle's prototype in a virtual modelling and simulation environment, such as MapleSim, can be a time-saving and inexpensive alternative approach. The reference vehicle used to model the high-fidelity electric vehicle is the 2012 Toyota Rav4 EV.

1.2   Research objectives

The research objectives are to develop high-fidelity powertrain components found in the reference electric vehicle, which are an AC induction motor, a 3-phase voltage source inverter, and motor controllers. The high-fidelity vehicle dynamics model is developed and it is used to build the electric vehicle system that includes the high-fidelity powertrain components. The high-fidelity models are developed in the modelling and simulation environments, such as Maple, MapleSim, Simulink, and MATLAB.

1.3 Approach

Various references are collected and studied thoroughly to derive the dynamic equations of the powertrain components. Krause et al. [1] and K. Bose [2] presented the dynamic model of the AC induction motor which was originally shown by G. Kron [3]. The dynamic direct-quadrature (d-q) equivalent circuit of the AC induction motor is used to derive the motor's dynamic equations which are based on the synchronously rotating reference frame (d^e-q^e). The developed motor model is a voltage-based model instead of a current-based model where the voltages are independent variables, and the developed torque is calculated from the dependent variables, such as the currents and flux linkages. To control the AC induction motor's speed or torque, the field-oriented control techniques invented by F. Blaschke [4] and K. Hasse [5] are studied thoroughly, and the corresponding speed and torque controllers are designed to control the developed induction motor model. Since a battery pack used in an electric vehicle provides DC power, a 3-phase inverter is required to convert constant power into 3-phase AC power that is used by the AC induction motor. The developed motor model is a voltage-based model, so a 3-phase voltage source inverter is studied and designed. Once all the powertrain components are developed and verified, the electric vehicle system is created by combining the high-fidelity vehicle dynamics model with the high-fidelity powertrain models. The electric vehicle system is tested for different driving scenarios, such as city, highway, and aggressive driving schedules collected by the U.S. Environmental Protection Agency.

1.4 Thesis organization

This thesis first presents the literature review and relevant backgrounds on electric vehicle configurations, and different types of electric motors with their speed and torque controllers. In the third chapter, the simplified longitudinal vehicle dynamics model and the high-fidelity MapleSim vehicle dynamics model are developed and validated. The electrical powertrain components' development and implementation process is explained and validated in Chapter 4. The motor controllers are developed next, and the electrical powertrain subsystem is assembled and simulated in Chapter 5. The electric vehicle system is assembled using the components developed in the previous chapters, and the electric vehicle system is simulated for different driving scenarios in Chapter 6. The final chapter concludes the thesis and the contributions of this research are summarized. Recommended future work is also summarized in the final chapter.

Chapter 2

Literature Review and Background

This chapter reviews available literature and research results that are applicable to the current topic. The first section presents different electric vehicle configurations that are introduced to the public. The second section reviews different modelling methods used for the electrical powertrain components, such as the AC induction motor and the 3-phase pulse-width-modulation (PWM) inverter. Lastly, different control schemes used on the electrical powertrain components are discussed.

2.1 Electric vehicle history

The first primitive electric carriage that had non-rechargeable primary cells was created by the Scottish inventor, Robert Anderson, in 1830 [6]. Thomas Davenport constructed the first DC electric motor in North America, and he is credited with building the first practical battery powered electric locomotive [7]. During the 1900s, electric vehicles had occupied a major portion of automobile market share in North America. For example, electric vehicles represented about 30 percent of all vehicles found in New York City, Boston, and Chicago [8]. The downfall of electric vehicles was first started by the introduction of mass-produced vehicles with an ICE by Henry Ford in 1908 which is famously known as the Model T [8]. Vehicles with a gasoline ICE were more powerful and had a longer driving range compared to electric vehicles, and most importantly, gasoline fuel was more readily available and inexpensive than electricity. Starting from the 1920s, electric vehicles started to disappear from automobile markets, and eventually electric vehicles were replaced by ICE powered vehicles [6].

Electric vehicles regained interest from governments and automotive manufacturers around the world when the price of oil was increasing at a rapid rate starting in the

1970s. For example, California passed the Zero Emission Vehicle Mandate in 1990 to force automotive manufacturers to produce and sell electric vehicles [6]. During that time, General Motors had successfully built a practical consumer electric car, called the EV1. The EV1's drivetrain and battery technology are still used in latest electric vehicles on the road today. The EV1's first generation was equipped with an AC induction motor with lead-acid battery packs. The second generation reduced its curb weight and improved its driving range by using nickel metal hydride (NiMH) battery packs. During the 2000s, the public had once again lost interest in electric vehicles due to its known disadvantages, such as a short driving distance and long charging duration. At the same time, Toyota and Honda introduced hybrid vehicles equipped with both electrical and mechanical drivetrains. These vehicles were good alternative fuel vehicles for consumers who were looking for a fuel efficient car that had a similar driving distance compared to ICE powered vehicles. As the oil price fluctuates everyday and environmental concerns arise from vehicle emissions in urban areas, such as carbon monoxide and nitrogen oxides, efficient electric vehicles that produce no tailpipe emissions are still needed in the present world. With advancements of battery technologies, such as latest lithium-ion battery cells, today's latest electric vehicles can travel a long distance per charge, and they have faster charging time compared to previous generation electric vehicles [9]. In the following sections, different electric vehicle configurations that are available in today's automobile market are presented.

2.2 Battery powered electric vehicle

An electric vehicle's configuration is designed based on a choice of the main energy source. Small electric vehicles, such as electric golf and shopping carts, are commonly equipped with a DC electric motor and lead-acid battery packs. Lead-acid batteries are the most inexpensive rechargeable battery in terms of kilowatt per hour charge, but they have low energy density compared to latest battery technologies, so they are only used for short-range electric vehicles [6]. Salameh et al. [10] presented a mathematical model of lead-acid batteries derived from the equivalent battery circuit, and they verified the developed battery model using experimental results. Nickel-based batteries were the next promising battery technology to be used in place of lead-acid batteries in electric vehicles. NiMH batteries have a higher energy density than lead-acid batteries, so they were deemed suitable for medium-range electric vehicles. NiMH battery packs were used in the second generation of the GM EV1, and they are still used in the Toyota Prius hybrid vehicles. Taniguchi et al. [11] explained the NiMH

battery development process for hybrid and electric vehicle applications. The latest compact sized electric vehicles are equipped with lithium-ion battery packs. Lithium-ion batteries have higher energy density, longer lifetime, and shorter charging time compared to lead-acid and NiMH batteries, but are significantly more expensive than the previous battery technologies. There have been many research activities to model a lithium-ion battery cell. Rong et al. [12] presented a mathematical lithium-ion battery model that predicts the remaining battery capacity; the electrical circuit battery model is presented by Chen et al. [13]; and Dao et al. [14] presented a physics-based lithium-ion battery model based on porous-electrode theory. In a survey done by Seaman et al. [15], they presented circuit-based and chemistry-based battery models intended for hybrid and electric vehicle applications. The Nissan Leaf, the world's bestselling electric car, has an AC synchronous motor with lithium ion battery packs. The electric vehicle from Tesla Motors and the Toyota's electric SUV have an AC asynchronous motor paired with lithium-ion battery packs. A summary of lead-acid, NiMH, and lithium-ion battery parameters are found from [6, 9] and listed in Table 2.1.

Table 2.1: Parameters for Lead-acid, NiMH, and Li-ion batteries

Battery type	Specific energy $\left[\frac{Wh}{kg}\right]$	Energy density $\left[\frac{Wh}{L}\right]$	Specific power $\left[\frac{W}{kg}\right]$	# of life cycles 80% discharge
Lead-acid	20-35	54-95	250	800
NiMH	70-95	150	200	1000
Lithium-ion	80-130	153	300	>1000

2.3 Hydrogen fuel powered electric vehicle

Lithium-ion batteries are commonly used in today's electric vehicles. They are lighter and have higher specific energy and power compared to NiMH battery packs, but the lithium-ion battery packs still require a considerable amount of time to fully charge [16]. Thus, the current battery powered electric vehicle is not suitable for a long distance travel since it would need to charge its battery pack frequently. Automotive manufacturers and researchers are seeking a new storage component that has higher energy density and shorter charging time than the battery pack currently used in electric vehicles. A hydrogen fuel powered electric vehicle is equipped with a hydrogen gas tank which is the main energy storage component, a stack of fuel cells, and an electric motor [17]. A fuel cell is an electrochemcial energy conversion device that uses hydrogen

fuel and oxygen to produce a DC voltage [18]. To understand how electricity is generated from fuel cells, chemical reactions in an acid electrolyte fuel cell between hydrogen and oxygen are explained [18]. At the fuel cell's anode, hydrogen gas H_2 ionizes which in turn releases electrons e^- and protons H^+.

$$2H_2 \longrightarrow 4H^+ + 4e^- \tag{2.1}$$

On the cathode side, oxygen O_2 reacts with electrons and protons to produce water H_2O.

$$O_2 + 4e^- + 4H^+ \longrightarrow 2H_2O \tag{2.2}$$

From the above chemical equations, the electrolyte, which is a polymer membrane that separates the anode and cathode, must only pass protons and keep electrons, so that electrons will flow through the external circuit to reach the cathode. Larminie et al. [6] showed the chemical process in the acid electrolyte fuel cell between the hydrogen gas and oxygen, which summarized in Figure 2.1.
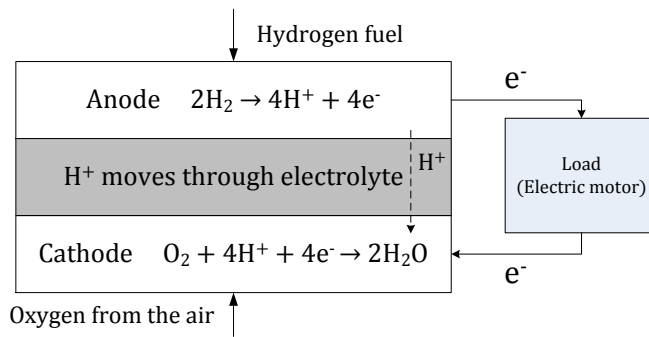
Figure 2.1: Chemical reactions in the fuel cell

A pressurized gas tank is used in hydrogen fuel powered electric vehicles to store hydrogen gas. A hydrogen gas tank's rate of refilling is faster, and its energy density is greater compared to a lithium-ion battery [9]. However, hydrogen gas refuelling infrastructures are not widely available, and there are safety concerns about having a highly pressurized gas tank in a vehicle. Toyota and Hyundai Motor have introduced consumer hydrogen gas powered electric vehicles, and the development process for Toyota fuel cell hybrid electric vehicles is presented in Aso et al. [19].

2.4 Electric traction motor

In electric vehicles, an electric motor is used in place of an ICE to produce traction torque. The popular electric motors used in electric vehicle applications are: brushed DC electric motors, permanent magnet AC synchronous motors, and AC induction motors.

2.4.1 Brushed DC motor

Brushed DC electric motors are used in electric vehicle applications because of their low cost and simplicity in implementation of motor controllers. The shortcoming of brushed DC motors for electric vehicle applications is mainly due to its durability. A commutator makes physical contacts with carbon brushes which causes degradation on the components. These components require frequent maintenance services, and the motor's life time is low for high intensity applications, such as variable speed or torque applications. However, due to its inexpensive cost and ease of control implementation, Gupta et al. [20] implemented the variable speed drive of a brushed DC motor for low cost electric vehicles.

2.4.2 AC synchronous motor

As the name of the AC synchronous motor indicates, the motor must rotate at a synchronous speed which is related to the supply power frequency. The basic principle of an AC synchronous motor is that a magnetic field produced from a stator attempts to align with a magnetic field produced from a rotor which is excited by a DC power supply. At steady-state operation, a rotor's magnetic field has aligned with a stator's magnetic field, hence the motor rotates at its synchronous speed. There are two main types of AC synchronous motor depending on how a rotor is excited: a wound rotor produces a magnetic field from a DC current, and a permanent magnet rotor produces a magnetic field from itself [2]. Since a permanent magnet AC synchronous motor (PMSM) does not need an external excitation, a PMSM is frequently used in variable speed drive applications. The PMSM modelling process and simulation results are presented in detail by Pillay and Krishnan [21], and Zhong et al. [22] showed a mathematical model of the PMSM for direct torque control applications. PMSMs are widely used in automotive industries for electric and hybrid vehicle applications where Toyota extensively uses a PMSM for its hybrid electric vehicle lineup [23].

2.4.3 AC induction motor

AC induction motors are widely used in industry as a main workforce because they are economical, rugged, and reliable [2] compared to other DC and AC machines. A squirrel-cage AC induction motor has a simple rotor structure in which a rotor is made from ferromagnetic steels, and its structure resembles a squirrel cage. Similar to AC synchronous motors, there is an AC induction motor with a wound rotor, but a squirrel-cage AC induction motor is commonly used due to its inherent ruggedness coming from a simple rotor structure. As the name of the induction motor indicates, a rotor's magnetic field is *induced* from a stator's magnetic field created by a 3-phase power supply. A rotor's magnetic field attempts to align with a synchronously rotating stator magnetic field, and a slip between rotor and stator magnetic fields develops motor torque. Due to the advantages of induction motors over other DC and AC machines, there has been much research activity on modelling and simulating induction motor models for variable speed and torque applications. A simple per-phase equivalent circuit model of the induction motor is adequate to predict motor operations in steady-state conditions. For highly dynamic performance applications, such as variable speed and torque drives, the dynamic direct-quadrature (*d-q*) model of the induction motor is used. The dynamic *d-q* model was originally used when developing induction motor's variable speed drives, such as a field-oriented controller. For current automotive applications, Tesla Motors is using an AC induction motor for all of its vehicle lineups. Since the reference vehicle, the Toyota Rav4 EV, has an AC induction motor from Tesla Motors, different modelling methods for an AC induction motor are explored.

Per phase equivalent circuit

A per phase equivalent circuit of an induction motor is used to predict a motor's performance at steady-state conditions. A simplified per phase equivalent circuit was presented by K. Bose [2], and it is shown in Figure 2.2. Using the simplified circuit, the torque equation as a function of slip can be derived.

Using the torque equation, a motor's torque-speed curve can be plotted. The torque equation also can be used to find the magnitudes of starting torque and breakdown torque [2].

$$T_e = 3(\frac{P}{2})\frac{R_r}{S\omega_e}\frac{V_s^2}{(R_s + R_r/S)^2 + \omega_e^2(L_{ls} + L_{lr})^2} \tag{2.3}$$

where P is a number of poles of the motor, and R_r, R_s, L_{lr}, and L_{ls} are the motor parameters included in the simplified per phase circuit. S is the per unit slip which is
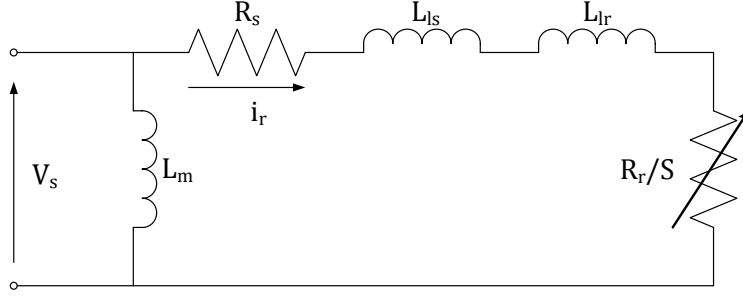
Figure 2.2: Simplified per phase equivalent induction motor circuit

defined as

$$S = \frac{\omega_e - \omega_r}{\omega_e} \tag{2.4}$$

where ω_e is the supply electrical speed or the synchronous speed (rad/s), and ω_r is the rotor electrical speed (rad/s). The magnitude of starting torque can be found by setting $S = 1$.

$$T_{starting} = 3(\frac{P}{2})\frac{R_r}{\omega_e}\frac{V_s^2}{(R_s + R_r)^2 + \omega_e^2(L_{ls} + L_{lr})^2} \tag{2.5}$$

The breakdown torque is the maximum torque developed by the induction motor before the torque decreases as the motor accelerates to a higher speed. The magnitude of breakdown torque can be found by first differentiating Equation (2.3) with respect to S and equating it to zero to find the slip S_m at breakdown torque.

$$S_m = \pm\frac{R_r}{\sqrt{R_s^2 + \omega_e^2(L_{ls} + L_{lr})^2}} \tag{2.6}$$

The positive component of S_m is substituted into Equation (2.3) to find the breakdown torque equation.

$$T_{breakdown} = \frac{3}{4}\frac{P}{\omega_e}\frac{V_s^2}{\sqrt{R_s^2 + \omega_e^2(L_{ls} + L_{lr})^2} + R_s} \tag{2.7}$$

The regenerative breakdown torque can be found by substituting the negative component of S_m into Equation (2.3). By using a per phase equivalent circuit, the motor's performance, such as staring and breakdown torque, can be predicted at steady-state conditions.

10

Dynamic d-q circuit

Since the per phase equivalent circuit is only valid in steady-state conditions, the dynamic d-q circuit is used to model the motor transient behaviours. A three-phase motor model can be represented as an equivalent two-phase motor model which is known as the dynamic d-q circuit model. There are two axes: d^s-q^s are the stator direct and quadrature axes, and d^r-q^r are the rotor direct and quadrature axes. This is illustrated in Figure 2.3(b). Depending on the choice of reference frame, the motor's dynamic equations derived from the dynamic d-q circuit can be further simplified. There are three main reference frames that researchers have used to develop the AC induction motor model. They are the stationary stator reference frame, rotating rotor reference frame, and synchronously rotating reference frame. Each reference frame has its own advantages and disadvantages depending on the intended application, so the reference frame should be selected carefully.

(a) 3-phase stator and rotor circuits   (b) 2-phase stator and rotor circuits
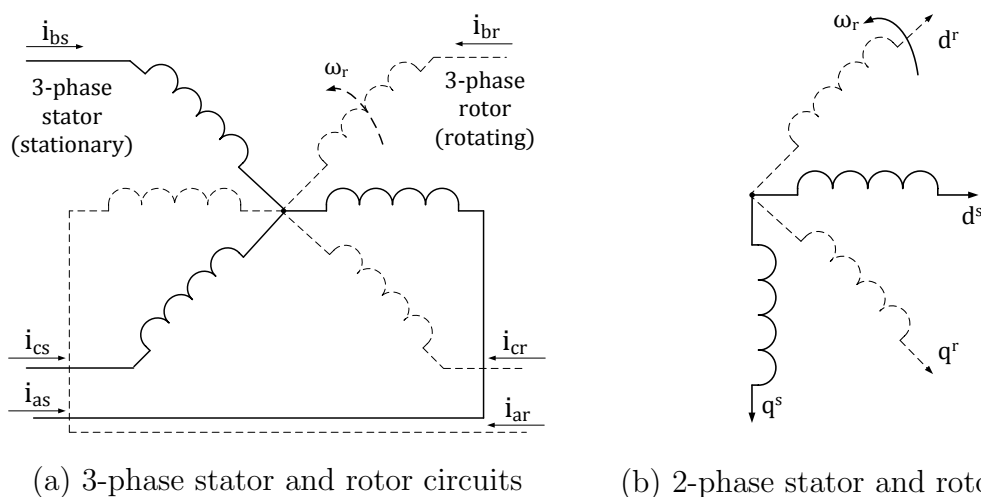
Figure 2.3: Simplified 3-phase and 2-phase induction motor circuits

Stationary stator reference frame

A stationary stator reference frame is fixed to a stator, and its d-axis is aligned with one of the stator's 3-phase (A-B-C) windings. Since its d-axis is always aligned with a stator's phase A winding, stator's d-axis variables would be exactly the same as physical stator phase A variables. Using the stationary stator reference frame has the benefit of not using any transformation methods to study motor's stator variables during simulations since the stator d-axis variables would be always identical to the

stator phase A variables [24]. Also, H.C. Stanley [25] referred rotor variables onto the stationary stator reference frame to eliminate time-varying inductances in an induction motor's voltage equations.

Rotating rotor reference frame

Similar to the stationary stator reference frame, a rotating rotor reference frame's d-axis is aligned with a rotor's phase A winding. Using a rotating rotor reference frame is useful when studying rotor variables during simulation since rotor phase A variables can be directly obtained from d-axis rotor variables.

Synchronously rotating reference frame

R.H. Park [26] first introduced the method to transform a synchronous motor's 3-phase stator winding variables, such as voltages, currents, and flux linkages, into fictitious windings rotating with the rotor at a synchronous speed. Referring the stator variables to a reference frame fixed in the rotor is called Park's transformation. This has the effect of eliminating all time-varying inductances in the synchronous motor's voltage equations. The synchronous motor has time-varying inductances because of a relative motion between stator and rotor circuits, and the circuits itself have varying magnetic reluctance [1]. G. Kron [3] referred the AC induction motor's stator and rotor variables in the reference frame rotating at a synchronous speed to eliminate the time varying inductances. The two reference frames used by Park and Kron have identical rotational speed which is a motor's synchronous speed. An arbitrary reference frame rotating at a synchronous speed is called a synchronously rotating reference frame, and it had been extensively used to model induction motors for control applications since the stator and rotor variables are in terms of DC quantities. Ozpineci et al. [27] demonstrated a Simulink implementation of an induction motor model derived from its dynamic d-q circuit models. The induction motor's dynamic d-q models are extensively used for variable speed applications [28, 29, 30], and variable torque applications [31, 32, 33].

2.5   AC induction motor control

An AC induction motor is used to power the Toyota Rav4 EV. Different modelling methods for an induction motor were explained in the previous section, and in this section, different speed and torque control schemes of an induction motor are explained. Compared to DC motors, the complexity of AC motor controllers is high because of the

inherent coupling effect that exists in AC motors. The coupling effect is caused from the fact that torque and flux are functions of voltage or current and frequency [2]. The induction motor's scalar control technique, which is known as an open-loop voltages per hertz (V/Hz) controller, is explained first followed by the explanation of vector control.

2.5.1   Open loop V/Hz control

For variable speed applications of the AC machines, the open-loop V/Hz controller is widely used because of its simplicity and availability [2]. Since the rotor electrical speed ω_r is approximately equal to the supply electrical speed ω_e which is also known as the motor's synchronous speed, ω_e is used as the primary control variable to adjust the motor's speed. The supplied voltage V_s^* is then directly calculated using ω_e and the gain factor G to keep the flux at a constant value ($\psi_s = V_s^*/\omega_e$). The open loop V/Hz controller's performance at a low speed is poor since the supplied voltage becomes small relative to the voltage drop across the stator resistance. To overcome this, the boost voltage can be added when the reference speed is small to increase the supplied voltage. The simple open loop V/Hz control's block diagram is displayed on Figure 2.4. Kataoka et al. [34] implemented the open loop V/Hz controller for an induction motor whereas Szabó et al. [35] implemented the controller on a synchronous electric motor.
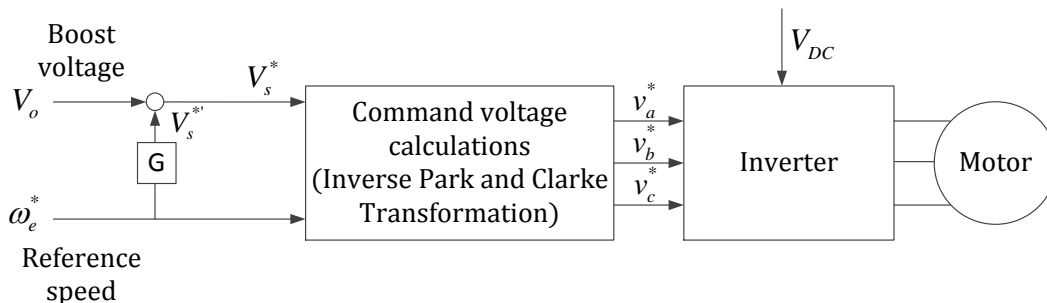
Figure 2.4: Open loop V/Hz speed control

2.5.2   Direct field-oriented control

Scalar control, such as the open loop V/Hz controller, is relatively simple to implement, but the inherent coupling effect that exists in the induction motor results in sluggish speed or torque response. Field-oriented control was introduced at the beginning of the 1970s, and it was demonstrated that synchronous and asynchronous

13

machines can perform like separately excited DC machines [2]. There are two general types of field-oriented control. The first one is direct field-oriented (DFO) control invented by Blaschke [4], and the second control method is called indirect field-oriented (IFO) control invented by Hasse [5]. DFO is discussed in this section, and IFO is explained in the next section.
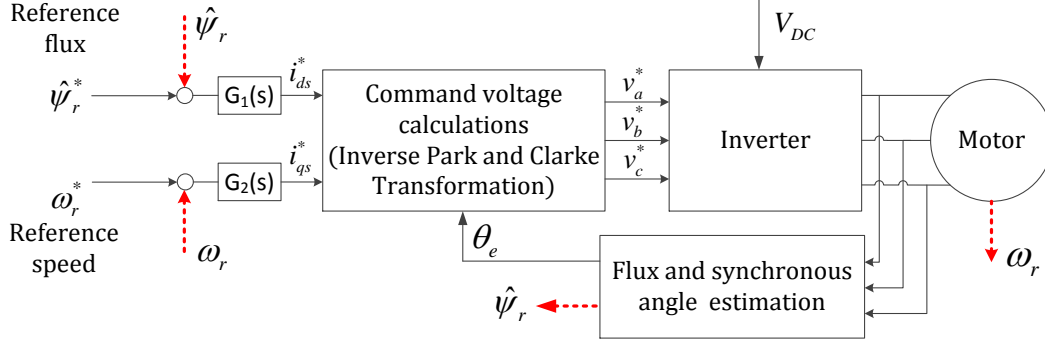
Figure 2.5: Direct field-oriented control

DFO control is designed based on the dynamic d-q induction motor model based on the d^e-q^e frame, and its block diagram is shown in Figure 2.5. The vector control variables, i_{ds}^{e*} and i_{qs}^{e*}, are controlled independently and they are calculated using the transfer functions, $G_1(s)$ and $G_2(s)$, which are shown in the figure. They are converted to 3-phase stationary variables, i_a^*, i_b^*, and i_c^*, using the unit vector magnitudes, $\sin\theta_e$ and $\cos\theta_e$ where the synchronous angle θ_e is the angle between the d-axis of the synchronously rotating reference frame and the d-axis of the stationary reference frame attached to a stator.

$$\cos\theta_e = \frac{\psi_{dr}^s}{\hat{\psi}_r} \tag{2.8a}$$

$$\sin\theta_e = \frac{\psi_{qr}^s}{\hat{\psi}_r} \tag{2.8b}$$

$$\hat{\psi}_r = \sqrt{\psi_{dr}^{s\,2} + \psi_{dr}^{s\,2}} \tag{2.8c}$$

where ψ_{dr}^s and ψ_{qr}^s are the measured or estimated direct and quadrature rotor flux linkages referred in the stationary stator reference frame. $\hat{\psi}_r$ is the estimated rotor flux linkage calculated using ψ_{dr}^s and ψ_{qr}^s. The unit vector magnitudes, $\sin\theta_e$ and $\cos\theta_e$, are calculated based on the rotor flux linkage vectors.

14

2.5.3 Indirect field-oriented control

IFO control is similar to DFO control method, and its block diagram is shown in Figure 2.6. The main difference is how the synchronous angle θ_e is calculated. For an induction motor, the synchronously rotating axes d^e-q^e always have the relative velocity to the rotating rotor axes d^r-q^r, which is called the slip speed ω_{sl}. The slip speed is calculated from the estimated rotor flux linkage $\hat{\psi}_r$, the reference quadrature stator current i_{qs}^{e*}, and the gain factor G_3. The synchronous speed ω_e is then calculated by adding the slip speed ω_{sl} and the rotor speed ω_r together. For rotor flux-oriented control, the synchronous angle is found by integrating the synchronous speed.

$$\omega_{sl} = G_3 \frac{i_{qs}^{e*}}{\hat{\psi}_r} \tag{2.9a}$$

$$\omega_e = \omega_r + \omega_{sl} \tag{2.9b}$$

$$\theta_e = \int \omega_e dt \tag{2.9c}$$

$\hat{\psi}_r$ is the estimated rotor flux linkage calculated from the direct stator current i_{ds}^e feedback signal.

$$\hat{\psi}_r = L_m i_{ds}^e \tag{2.10}$$
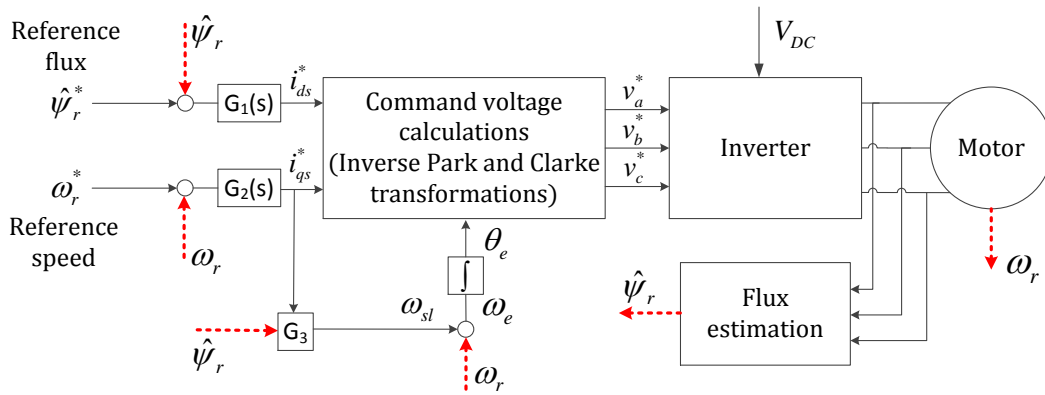
Figure 2.6: Indirect rotor field-oriented control

2.6 Reference electric vehicle

The reference vehicle used to model the high-fidelity electric SUV is the 2012 Toyota Rav4 EV. The first generation Toyota Rav4 EV was introduced in 1997 which was equipped with an AC electric motor and NiMH battery packs [36]. Except for the electrical powertrain system difference, the first generation Rav4 EV was identical to a second generation gasoline Rav4. Toyota converted the third generation gasoline Rav4 to develop and produce the 2012 Rav4 EV. Tesla Motors contributed to the development and production of the 2012 Rav4 EV by supplying the electrical powertrain components, including the AC induction motor, lithium-ion battery packs, and powertrain controllers to Toyota. Table 2.2 summarizes the mechanical and electrical specifications of the 2012 Toyota Rav4 EV [37, 38].

Table 2.2: Mechanical and electrical specifications of the 2012 Toyota Rav4 EV

Mechanical		Electrical	
Drive type	Front-wheel Drive (FWD)	Motor type	AC induction motor
Curb mass	1830 kg	Powertrain max. output	115 kW @ 300 rpm
Overall height /width /length	1684/1816/4574 mm	Motor max. output	300 kW @ 7000 rpm at 900A
Front/rear track	1560/1560 mm	Motor max. torque	385 N·tm
Wheelbase	2641.6 mm	Motor max. speed	14500 rpm
Coeff. of drag	0.3	Traction battery type	Lithium-ion
Transmission	Fixed gear open-differential Gear ratio: 9.73	Battery max. output	129 kW
Brake	Disc	Battery usable energy	41.8 kWh
Front/rear suspension	MacPherson Double-wishbone	Battery max. voltage	386 V
Maximum speed	135 km/h (Eco) 160 km/h (Sport)	Battery min. voltage	276 V

Chapter 3

Electric Vehicle Modelling

In this chapter, the development of a high-fidelity vehicle dynamics model of the Toyota Rav4 EV is presented in detail. The Toyota Rav4 EV's vehicle dynamics is presented in both the Simulink longitudinal vehicle dynamics model and high-fidelity MapleSim vehicle dynamics model. The Simulink longitudinal vehicle dynamics model is first developed using the Toyota Rav4 EV specifications. The development of the high fidelity MapleSim vehicle dynamics model is presented, and the two simulations results are compared in the last section.

3.1   Longitudinal vehicle dynamics

The reference vehicle is a front-wheel driven vehicle, and its free body diagram (FBD) is shown in Figure 3.1. Using the FBD, the total forces acting on the vehicle can be calculated. F_R is the total resistance force, assumed to act at the height of the vehicle's centre of gravity, F_x is the total traction force produced by two front tires, and F_{fN} and F_{rN} are the front and rear tire normal forces. Lastly, F_g is the total gravitational force acting on the vehicle.

$$\sum F_x = m_v \ddot{x} \tag{3.1a}$$

$$F_x - F_R - F_g \sin\theta = m_v \ddot{x} \tag{3.1b}$$

The aerodynamic resistance force F_{aero} is due to aerodynamic drag which can be estimated from the air density ρ, a vehicle's coefficient of drag C_d, and a vehicle's frontal area A_{ref}. The rolling resistance force F_{res} is generated from the rolling resistance of

17
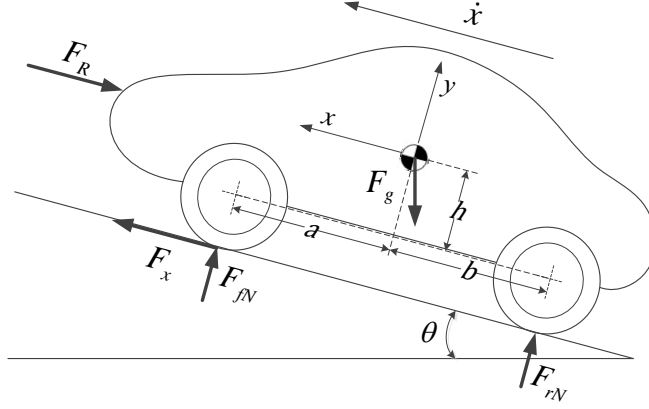
Figure 3.1: FBD of a front-wheel drive vehicle

tires that can be estimated from the vehicle weight $m_v g$, the coefficient of friction μ_r, and the slope of the road θ. The key modelling assumptions for the longitudinal vehicle model are that the vehicle only moves in a straight line, and the only degree of freedom of the model is the longitudinal speed which is denoted as $\dot{x}$.

$$F_R = F_{aero} + F_{res} \tag{3.2a}$$

$$F_{aero} = \frac{1}{2}\rho C_d A_{ref} \dot{x}^2 \tag{3.2b}$$

$$F_{res} = \mu_r m_v g \cos(\theta) \tag{3.2c}$$

The longitudinal vehicle dynamics model has longitudinal weight transfer calculations that adjust the front and rear tire's normal forces [39]. The weight transfer model considers longitudinal acceleration, slope of the road, and aerodynamic and gradient resistance forces which are assumed to act through the vehicle's centre of gravity (CG). The front and normal tire's normal weights are calculated using:

$$F_{fN} = \frac{bF_g\cos(\theta) - h\left(F_R + F_g\sin(\theta) + m_v\ddot{x}\right)}{a+b} \tag{3.3a}$$

$$F_{rN} = \frac{aF_g\cos(\theta) + h\left(F_R + F_g\sin(\theta) + m_v\ddot{x}\right)}{a+b} \tag{3.3b}$$

where h is the CG height, a is the distance between the front axle and the CG, and b is the distance between the rear axle and the CG as depicted on Figure 3.1.

18

3.1.1 Differential and transmission

The Toyota Rav4 EV has a single speed fixed gear box and an open-differential connecting an electric motor to two front wheels. The dynamic model of the drivetrain is illustrated in Figure 3.2. The differential and transmission are simple static models that consider the efficiency and torque/speed ratio of each system. The key modelling assumptions for the drivetrain's dynamic model are: the clutch and torque converters are always fully engaged, and the vehicle is only driven in a straight line, so the left and right applied wheel torque and angular speeds will be equal.
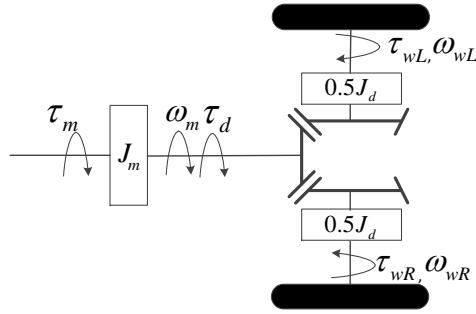
Figure 3.2: Dyanmic model of the electric vehicle drivetrain

From Figure 3.2, the drivetrain dynamic equations are derived.

$$\tau_m - \tau_d = J_m \ddot{\theta}_m \tag{3.4}$$

where τ_m is the motor input torque, and τ_d is the differential input torque. J_m is the rotational moment of inertia of the motor, and θ_m is the angular rotation of the motor.

For a straight line driving simulation, the applied left and right wheel torque will be equal ($\tau_w = \tau_{wR} = \tau_{wL}$), and the left and right wheel speed will be equal ($\omega_w = \omega_{wR} = \omega_{wL}$), so the dynamic equations relating the differential and the front wheel are:

$$\frac{1}{2}\eta_d B_d \tau_d - \tau_w = \frac{1}{2} J_d \ddot{\theta}_w \tag{3.5a}$$

$$\dot{\theta}_w = \frac{\dot{\theta}_m}{B_d} \tag{3.5b}$$

where B_d is the differential ratio, η_d is the transmission efficiency, J_d is the rotational moment of inertia of the differential, τ_w is the front wheel torque, and lastly θ_w is the angular rotation of the front wheel.

19

3.1.2 Tire model

The tire model is the linear dynamic longitudinal tire model presented by Pacejka [40], and the model is only valid under small longitudinal slip conditions. The tire's dynamic equation is defined as:

$$\dot{u} + \frac{V_x}{\sigma_\kappa} u + V_{sx} = 0 \tag{3.6}$$

where u is the longitudinal deflection, V_x is the wheel centre's longitudinal speed, and σ_κ is the tire's relaxation length calculated using the longitudinal slip stiffness $C_{F\kappa}$ and the longitudinal tire stiffness at road level C_{Fx}.

$$\sigma_\kappa = \frac{C_{F\kappa}}{C_{Fx}} \tag{3.7}$$

V_{sx} is the slip velocity which is defined as:

$$V_{sx} = V_x - r_{eff}\dot{\theta}_w \tag{3.8}$$

where r_{eff} is the tire's effective rolling radius. Finally, the longitudinal traction force generated from the tire is defined as:

$$F_x = C_{Fx}\kappa' = C_{Fx}\frac{u}{\sigma_\kappa} \tag{3.9}$$

where κ' is the longitudinal slip. The sum of the moments acting on the front wheel is shown in Figure 3.3, and it is used to derive the spin dynamics of the front wheel.

$$\tau_w - r_{eff}F_x = J_w\ddot{\theta}_w \tag{3.10}$$

where J_w is the rotational moment of inertia of the wheel.
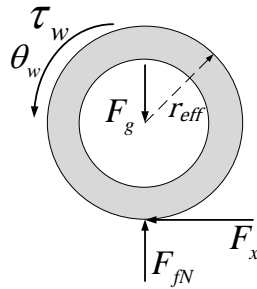
Figure 3.3: FBD of a front wheel

20

3.1.3 Implementation and results

The Simulink longitudinal vehicle dynamics model is developed by combining Equations (3.1) to Equations (3.3) into a Simulink block. Similarly, the drivetrain dynamic equations and tire dynamic equations presented in the previous sections are combined into Simulink blocks to come up with the Simulink drivetrain and tire models. Illustration of the three Simulink blocks are shown in Figure 3.4 with their inputs and outputs.
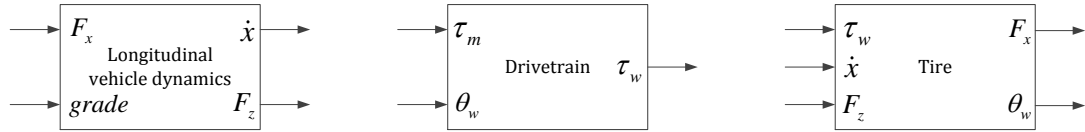
Figure 3.4: Illustrations of the Simulink vehicle dynamics components

The three blocks are assembled on a Simulink workplace to create the longitudinal vehicle dynamics system. A reference speed profile is used as the input to the vehicle system, and a simple driver model calculates the reference motor torque from the difference between the reference and actual vehicle speed. An electric motor model is not included in the system. It is assumed that an infinite amount of motor torque is available, so the reference motor torque calculated from the driver model goes directly into the drivetrain block. The complete Simulink longitudinal vehicle dynamics system is shown in Figure 3.5.
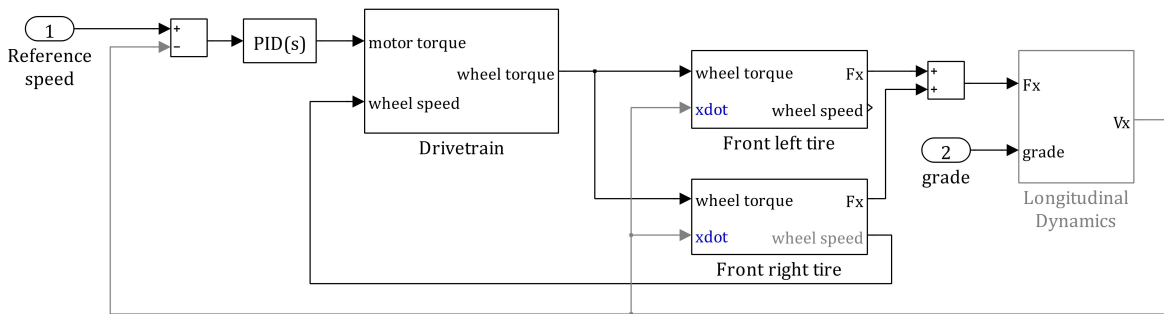
Figure 3.5: Simulink implementation of the longitudinal vehicle dynamics

The Toyota Rav4 EV vehicle and tire parameters listed in Table 2.2 are used to simulate the Simulink longitudinal vehicle dynamics system. A simple reference speed profile is applied, and the vehicle's responses — the vehicle speed $\dot{x}$, applied wheel torque τ_w and front right tire's normal force F_{fN} — are measured and plotted in Figure 3.6.

21

From the simulation results, the applied wheel torque and front right tire normal force are in accordance with the vehicle acceleration. When the vehicle is accelerating, the applied wheel torque undergoes a positive step change, and the front tire's normal force decreases due to the backward weight transfer. Similarly when the vehicle is decelerating, the applied wheel torque undergoes a negative step change, and the front tire's normal force increases due to the forward weight transfer.
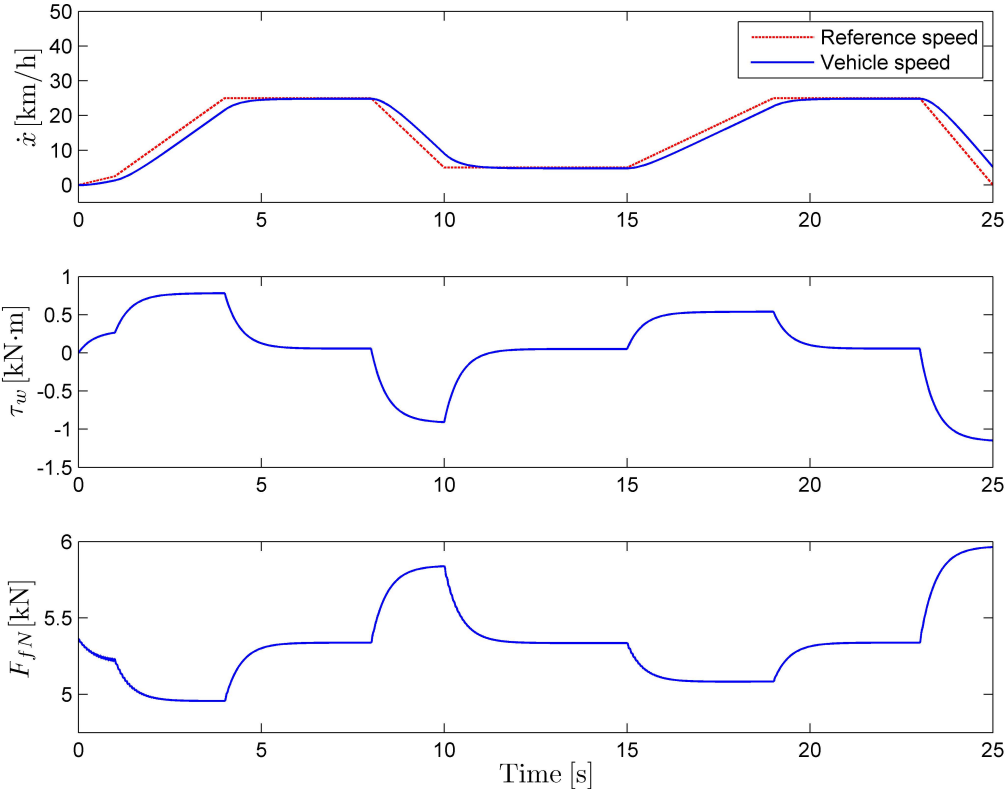
Figure 3.6: Simulation results – Simulink longitudinal vehicle dynamics model

3.2 MapleSim vehicle dynamics model

MapleSim is a multi-domain modelling and simulation environment that gives access to symbolic equations. Users can drag and drop built-in MapleSim components that represent physical models, such as a rigid mass, revolute and prismatic joints, to build kinematic or dynamic models. The high-fidelity vehicle dynamics model of the Toyota

Rav4 EV is developed in MapleSim, and its three-dimensional representation captured from the MapleSim visualization window is shown in Figure 3.7.

The vehicle is a four wheeled vehicle that has two wheels at the front and two wheels at the rear. Each wheel has one independent vertical suspension, adding 4 degrees of freedom (DOF) to the overall system. The chassis is a rigid body with 6 DOF, and 4 DOF come from the rotation of the four wheels. Overall, the system has 14 DOF which are sufficient to predict the longitudinal dynamics of the vehicle. Tires are standard car tires, and they are modelled using the Pacejka 2002 model developed by Pacejka [40]. The MapleSim components that are used to develop the high-fidelity vehicle dynamics model are explained in detail in the following sections.
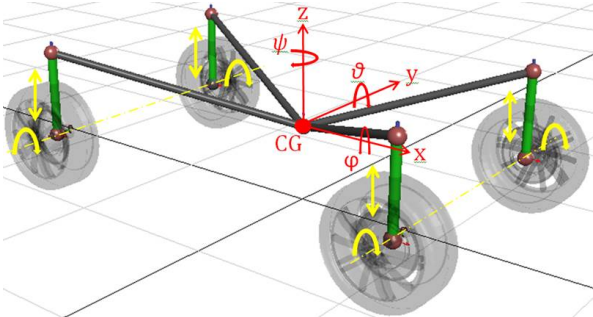
Figure 3.7: Three-dimensional representation of the MapleSim vehicle model

3.2.1 Vehicle chassis components

The vehicle's chassis is modelled using a MapleSim rigid body component that has a body fixed coordinate xyz attached at its centre of mass as illustrated on Figure 3.7.

Figure 3.8: MapleSim rigid body and rigid body frame components

The mass of rigid body m and its moment of inertia matrix $[I]$ are used as the main parameters for a MapleSim rigid body component. Also, the initial conditions are assigned to set initial linear displacement and velocity, and initial angular displacement and velocity with respect to the ground frame. MapleSim rigid bodies are used as the hard-points in the vehicle chassis, such as the chassis's centre of gravity, the start and end locations of the suspensions, and lastly the point where the wheel is connected to the suspension. The rigid bodies are connected to one another using a MapleSim rigid

23

body frame where the rigid body frame provides a fixed displacement and orientation between the two connected rigid bodies.

3.2.2   Suspension components

Prismatic joint

The four independent suspensions are modelled using MapleSim built-in prismatic joint blocks. A prismatic joint allows one translational DOF between the two connected frames.
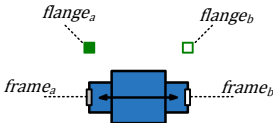
Figure 3.9: MapleSim prismatic joint

There are four prismatic joint parameters: the unit vector $\hat{e}_1$ that assigns the joint's translational direction, the spring and damping constants, K_s and K_d, and lastly the spring's unstretched length L_0. Also, there are two initial conditions that can be assigned which are the joint's initial length and speed.

Revolute joint

MapleSim revolute joints are used to connect the four wheels to the four independent suspensions. A revolute joint only allows one rotational DOF between the two frames. Similar to the MapleSim's prismatic joint parameters, there are four revolute joint parameters: the unit vector $\hat{e}_1$ that assigns the joint's rotational direction, the rotational spring and damping constants, K_s and K_d, and lastly the rotational spring's unstretched angle θ_0. Two initial conditions are assigned to set the joint's initial angular position and velocity.
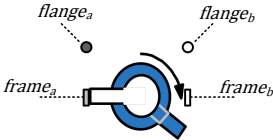
Figure 3.10: MapleSim revolute joint

3.2.3 Differential and transmission components

MapleSim ideal gear components are used to connect an electric motor to the front wheels, and a MapleSim ideal gear block is shown in Figure 3.11. The component is an ideal gearbox with one driving shaft, which is connected to $flange_a$, and one driven shaft that is connected to $flange_b$. In the ideal gear box, there is no associated inertia, elasticity, damping, and backlash. For the MapleSim vehicle dynamics model, the $flange_a$ is connected to the electric motor, and the $flange_b$ is connected to the front wheels.
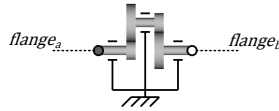
Figure 3.11: MapleSim ideal gear

This component is represented by following equations.

$$\theta_a = r\theta_b \tag{3.11a}$$

$$r\tau_a = -\tau_b \tag{3.11b}$$

where r is the gear ratio.

3.2.4 Tire components

MapleSim built-in standard tire components and Pacejka tire models are used. Kinematic tire parameters and tire normal forces are internally calculated by the MapleSim standard tire component. From the standard tire component shown in Figure 3.12, the tire's longitudinal and lateral slip angles, the tire's central linear and rotational speed, and the tire's normal forces are calculated.
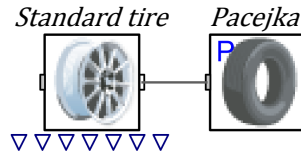
Figure 3.12: MapleSim standard tire and tire force components

In MapleSim, many different tire force models are available, such as Linear, Calspan, Fiala, and Pacejka tire models. Since the Pacejka tire model is widely used in vehicle

dynamics simulations due to its advantages over other tire models [40], the Pacejka tire model is selected to be used in the high-fidelity MapleSim vehicle dynamics model.

3.2.5   Implementation and results

Using the MapleSim components introduced in the previous sections, the front-wheel driven vehicle with four independent suspensions is developed in a MapleSim user interface as depicted in Figure 3.13. The four prismatic joint blocks are used to model the four independent suspensions. The four standard tire components and Pacejka tire models are included and they are connected to the wheel carrier, which is modelled as a mass-less rigid body, using the four revolute joints as shown in the figure. The input to the system is the same reference speed profile used during the Simulink longitudinal vehicle dynamics simulations. A MapleSim PID controller block is used as a driver model to calculate the reference motor torque from the difference between the reference and vehicle speed feedback signals. The reference motor torque is magnified through the ideal gear block which is then applied onto the revolute joint to rotate the wheel by the applied wheel torque. Lastly, the resistance force calculation block shown in the figure calculates the magnitude of aerodynamic resistance force and applies it to the rigid body which is the vehicle's CG.
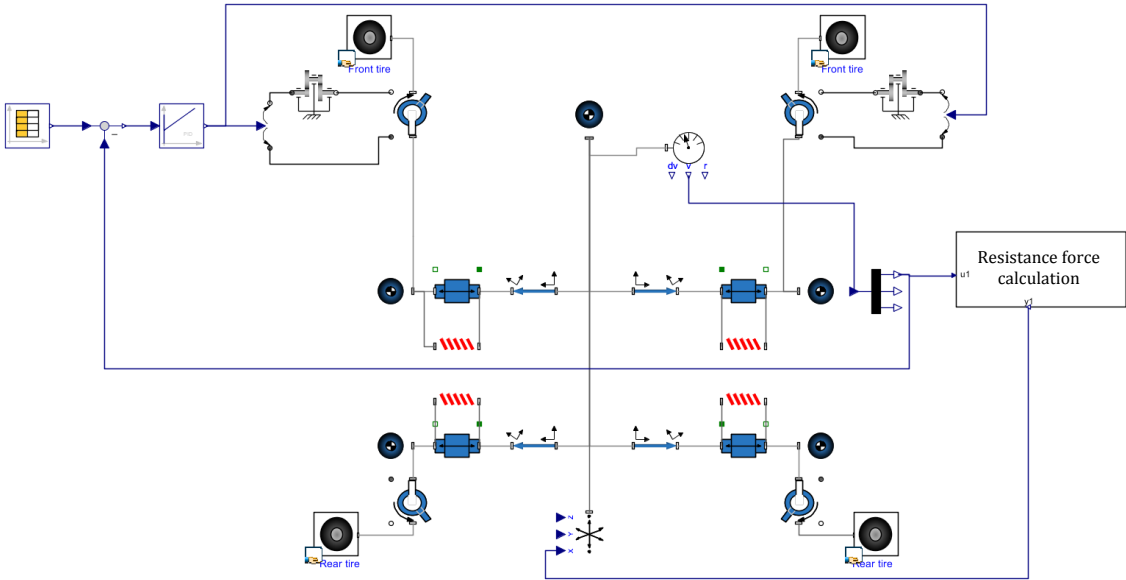
Figure 3.13: High-fidelity MapleSim vehicle dynamics model of the Toyota Rav4 EV

The same vehicle and simulation parameters are used in the following simulations.

The PID controllers gains are also identical in the Simulink and MapleSim vehicle dynamics simulations. On Figure 3.14, the simulation results of the Simulink and MapleSim vehicle dynamics models are plotted together. Since the MapleSim vehicle model has more detailed components, such as the suspensions and tire models, its responses contain higher order dynamics than the Simulink vehicle dynamics model. However, the two responses overlap each other very closely, and their wheel torques and right front wheel normal force profiles are very similar to each other.
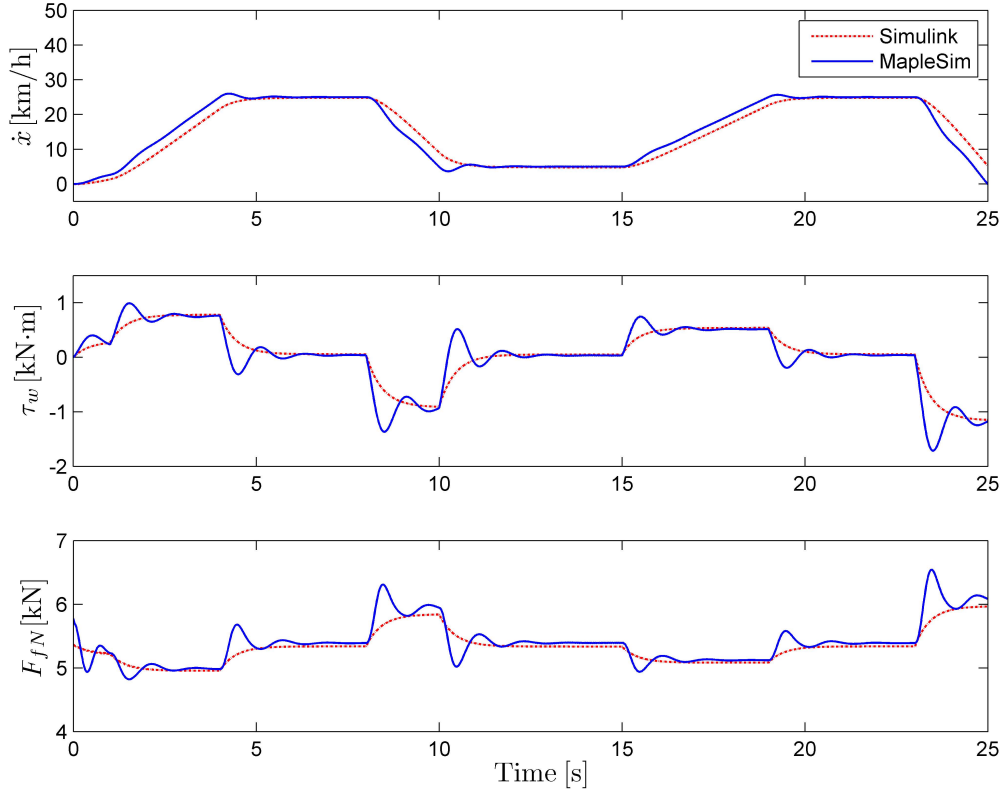
Figure 3.14: Comparison of the Simulink and MapleSim vehicle dynamics simulations

Chapter 4

Electrical Powertrain Modelling

The Toyota Rav4 EV's electrical powertrain system consists of the AC induction motor and its motor controller, the 3-phase PWM DC/AC inverter, and lithium-ion battery packs. The mathematical representations of the AC induction motor's dynamic equations are explained first followed by explanations of the 3-phase PWM DC/AC voltage source inverter. The development of a lithium-ion battery model and its battery management system is not covered in this work, and instead, a constant voltage input is used.

4.1   Asynchronous AC induction motor

AC induction motors are widely used in industry because of their reliability and robustness, low maintenance cost, and high efficiency compared to DC machines [41]. Particularly, a squirrel-cage induction motor is the most widely used AC mechanical power source in industry due to its simple structure compared to wound AC induction motors [41]. AC induction motor models can be developed using different reference frames, such as a stationary reference frame, a rotating reference frame attached to a rotor, and a synchronously rotating reference frame. The selection of the induction motor's reference frame has to be carefully considered since each reference frame has its own advantages and disadvantages [24]. For motor control applications, it is desirable to develop the induction motor model using the synchronously rotating reference frame (d^e-q^e) because all the time-varying inductances in the voltage equations can be eliminated, and thus, the motor variables will only have DC components.

   The following section introduces the two key transformation techniques used to transform three-phase stationary signals into two-phase synchronously rotating sig-

nals. Clarke [42] presented the Clarke transformation to convert three-phase stationary signals into two-phase stationary signals. R.H. Park [26] introduced the coordinate transformation method to convert two-phase stationary signals into two-phase signals rotating at a synchronous speed.

4.1.1 Clarke transformation

In a 3-phase AC motor, there are three stationary stator windings and three rotating rotor windings which will generate 3-phase AC motor variables, such voltages, currents, and flux linkages. Using the Clarke transform [42], three-phase stationary reference frame (a-b-c) signals are converted into two-phase stationary frame (d^s-q^s) signals as illustrated in Figure 4.1. The d^s and q^s axes are always orthogonal to each other.
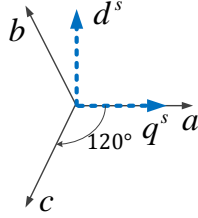
Figure 4.1: Clarke transformation

The q^s-axis is always aligned with the a-axis which results in the following Clarke transformation matrix, $\mathbf{K_s}$, that converts the three-phase stationary current signals (i_a, i_b, i_c) into the two-phase stationary current signals (i_{qs}^s, i_{ds}^s).

$$
\begin{bmatrix} i_{qs}^s \\ i_{ds}^s \\ i_{os}^s \end{bmatrix} = \mathbf{K_s} \begin{bmatrix} i_a \\ i_b \\ i_c \end{bmatrix} = \frac{2}{3} \begin{bmatrix} 1 & -\frac{1}{2} & -\frac{1}{2} \\ 0 & -\frac{\sqrt{3}}{2} & \frac{\sqrt{3}}{2} \\ \frac{1}{2} & \frac{1}{2} & \frac{1}{2} \end{bmatrix} \begin{bmatrix} i_a \\ i_b \\ i_c \end{bmatrix}
\tag{4.1}
$$

where i_{os}^s is the zero sequence component. The corresponding inverse Clarke transformation is shown below which converts the two-phase stationary current signals into the three-phase stationary current signals.

$$
\begin{bmatrix} i_a \\ i_b \\ i_c \end{bmatrix} = (\mathbf{K_s})^{-1} \begin{bmatrix} i_{qs}^s \\ i_{ds}^s \\ i_{os}^s \end{bmatrix} = \begin{bmatrix} 1 & 0 & 1 \\ -\frac{1}{2} & -\frac{\sqrt{3}}{2} & 1 \\ -\frac{1}{2} & \frac{\sqrt{3}}{2} & 1 \end{bmatrix} \begin{bmatrix} i_{qs}^s \\ i_{ds}^s \\ i_{os}^s \end{bmatrix}
\tag{4.2}
$$

4.1.2 Park transformation

R.H Park [26] introduced the method to transform two-phase stationary reference frame signals into two-phase rotating reference frame signals rotating at an arbitrary angular speed. It is important to note that an AC induction motor is an asynchronous machine, so the rotor's rotational speed cannot reach a motor's synchronous speed. The relative speed between the synchronously rotating frame and the rotor's rotating frame always exists, and it is called the slip speed ω_{sl}.

The reference frame $(d^e\text{-}q^e)$ is rotating at the motor's synchronous speed, and the synchronous speed is defined as

$$\omega_e = \omega_r + \omega_{sl} \tag{4.3}$$

The motor's synchronous speed can be calculated by adding the slip speed ω_{sl} and the rotor speed ω_r. The angle (θ_e) between the stationary and synchronously rotating frame is used in the forward Park transformation matrix to transform the two-phase stationary current signals into the two-phase synchronously rotating current signals (i^e_{qs}, i^e_{ds}).
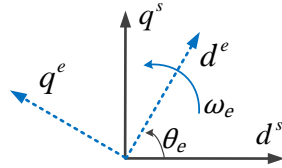
Figure 4.2: Park transformation

The orthogonality of the two axes, d^e and q^e, is retained while they are rotating at a synchronous speed. The transformation matrix, $\mathbf{K^e_s}$, is used for the forward Park transformation.

$$\begin{bmatrix} i^e_{qs} \\ i^e_{ds} \end{bmatrix} = \mathbf{K^e_s} \begin{bmatrix} i^s_{qs} \\ i^s_{ds} \end{bmatrix} = \begin{bmatrix} \cos\theta_e & -\sin\theta_e \\ \sin\theta_e & \cos\theta_e \end{bmatrix} \begin{bmatrix} i^s_{qs} \\ i^s_{ds} \end{bmatrix} \tag{4.4}$$

The corresponding inverse Park transformation is

$$\begin{bmatrix} i^s_{qs} \\ i^s_{ds} \end{bmatrix} = (\mathbf{K^e_s})^{-1} \begin{bmatrix} i^e_{qs} \\ i^e_{ds} \end{bmatrix} = \begin{bmatrix} \cos\theta_e & \sin\theta_e \\ -\sin\theta_e & \cos\theta_e \end{bmatrix} \begin{bmatrix} i^e_{qs} \\ i^e_{ds} \end{bmatrix} \tag{4.5}$$

4.1.3 Reference frame selection

The synchronously rotating reference frame which has the angular speed of ω_e is used to develop the dynamic equations of the AC induction motor. R.J. Lee et al. [24] proposed the outline for selecting a suitable induction motor's reference frame depending on different induction motor applications. The synchronously rotating reference frame is selected to construct the motor's dynamic equations because the time varying inductances in the voltage equations can be eliminated [3]. Also, the stator and rotor's magnetic fields are rotating at the synchronous speed ω_e, so referring the stator and rotor's variables, such as voltages, current, and flux linkages, to the synchronously rotating reference frame has the effect of converting the stator and rotor's variables into DC quantities. This is especially beneficial when developing motor controllers because the classical control theory, such as a proportional-integral-derivative controller, can be used. The variable speed controllers, such as direct and indirect field-oriented controllers which will be discussed in the next section, are originally developed based on the dynamic d^e-q^e induction motor model.

Table 4.1: Summary of the reference frame used to model the induction motor

Reference frame speed	Interpretation	Initial frame	Final frame	Transformation method and matrix
0	Stationary 3-phase variables referred to the stationary 2-phase reference frame	a-b-c	d^s-q^s	Clarke $\mathbf{K_s}$
0	Stationary 2-phase variables referred to the stationary 3-phase reference frame	d^s-q^s	a-b-c	Inverse Clarke $(\mathbf{K_s})^{-1}$
ω_e	Stationary 2-phase variables referred to the synchronously rotating 2-phase reference frame	d^s-q^s	d^e-q^e	Park $\mathbf{K_s^e}$
ω_e	Synchronously 2-phase rotating variables referred to the stationary 2-phase reference frame	d^e-q^e	d^s-q^s	Inverse Park $(\mathbf{K_s^e})^{-1}$

Table 4.1 summarizes the two transformation methods that are used to convert three-phase stationary signals to two-phase synchronously rotating signals. Also, their

corresponding inverse transformation matrices are shown. The motor's synchronous speed ω_e is updated in each simulation step using Equation (4.3).

4.1.4 Dynamic model of the AC induction motor

There are different ways to formulate an induction motor's model. Some researchers have developed induction motor models with respect to the stator reference frame or the rotating reference frame attached to the rotor [33]. The dynamic equivalent circuits shown in Figure 4.3 are based on the synchronously rotating reference frame d^e-q^e, and the dynamic equations of the induction motor are derived and listed in this section.
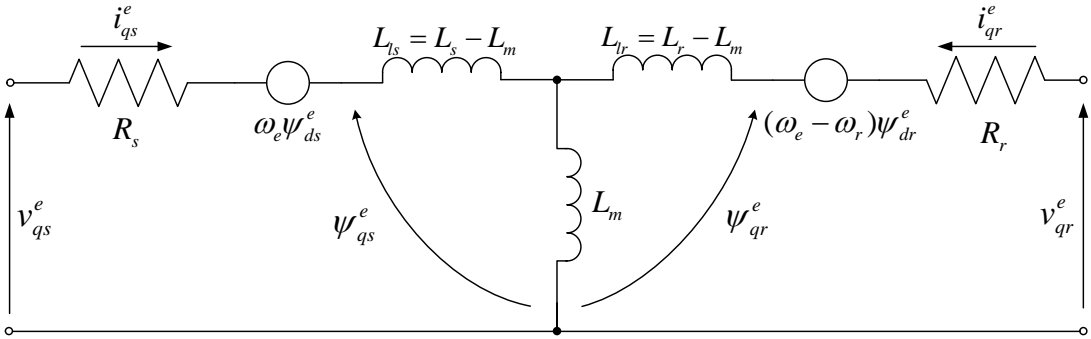
(a) A quadrature component of the induction motor's circuit
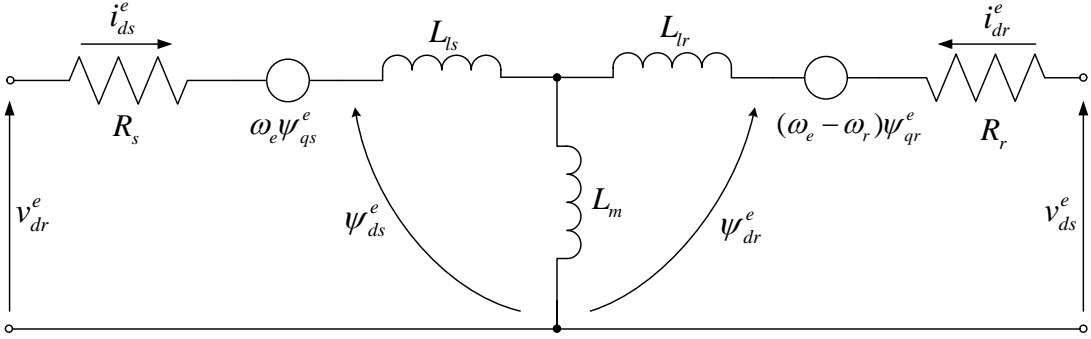
(b) A direct component of the induction motor's circuit

Figure 4.3: AC induction motor's dynamic equivalent circuit

Kron et al. [3] referred the stator and rotor variables such as voltages, currents, and flux linkages in a synchronously rotating reference frame. The motor's voltage

equations are expressed in a synchronously rotating reference frame.

$$v_{qs}^e = R_s i_{qs}^e + \frac{d}{dt}\psi_{qs}^e + \omega_e \psi_{ds}^e \tag{4.6a}$$

$$v_{ds}^e = R_s i_{ds}^e + \frac{d}{dt}\psi_{ds}^e - \omega_e \psi_{qs}^e \tag{4.6b}$$

$$v_{qr}^e = R_r i_{qr}^e + \frac{d}{dt}\psi_{qr}^e + (\omega_e - \omega_r)\psi_{dr}^e \tag{4.6c}$$

$$v_{dr}^e = R_r i_{dr}^e + \frac{d}{dt}\psi_{dr}^e - (\omega_e - \omega_r)\psi_{qr}^e \tag{4.6d}$$

The voltage equations are defined in terms of flux linkages per second ψ. They are redefined using flux linkages which are noted as F instead of the flux linkages per second ψ.

$$F_{qs}^e = \omega_b \psi_{qs}^e \tag{4.7a}$$

$$F_{ds}^e = \omega_b \psi_{ds}^e \tag{4.7b}$$

$$F_{qr}^e = \omega_b \psi_{qr}^e \tag{4.7c}$$

$$F_{dr}^e = \omega_b \psi_{dr}^e \tag{4.7d}$$

where ω_b is the motor's base speed. Now Equations (4.6) are redefined as

$$v_{qs}^e = R_s i_{qs}^e + \frac{1}{\omega_b}\frac{d}{dt}F_{qs}^e + \frac{\omega_e}{\omega_b}F_{ds}^e \tag{4.8a}$$

$$v_{ds}^e = R_s i_{ds}^e + \frac{1}{\omega_b}\frac{d}{dt}F_{ds}^e - \frac{\omega_e}{\omega_b}F_{qs}^e \tag{4.8b}$$

$$0 = R_r i_{qr}^e + \frac{1}{\omega_b}\frac{d}{dt}F_{qr}^e + \frac{(\omega_e - \omega_r)}{\omega_b}F_{dr}^e \tag{4.8c}$$

$$0 = R_r i_{dr}^e + \frac{1}{\omega_b}\frac{d}{dt}F_{dr}^e - \frac{(\omega_e - \omega_r)}{\omega_b}F_{qr}^e \tag{4.8d}$$

where v_{qr}^e and v_{dr}^e are set to zero for a squirrel-cage induction motor [27]. The flux linkage expressions can be derived from the dynamic d^e-q^e circuit model shown in Figure 4.3 in terms of stator and rotor currents. Note that the flux linkages F are expressed by

33

multiplying original flux linkages per second ψ by the base speed ω_b.

$$F_{qs}^e = X_{ls}i_{qs}^e + X_m(i_{qs}^e + i_{qr}^e) \tag{4.9a}$$

$$F_{qr}^e = X_{lr}i_{qr}^e + X_m(i_{qs}^e + i_{qr}^e) \tag{4.9b}$$

$$F_{ds}^e = X_{ls}i_{ds}^e + X_m(i_{ds}^e + i_{dr}^e) \tag{4.9c}$$

$$F_{dr}^e = X_{lr}i_{dr}^e + X_m(i_{ds}^e + i_{dr}^e) \tag{4.9d}$$

where X_m is the mutual reactance, and X_{ls} and X_{lr} are the stator and rotor's leakage reactance that are defined as

$$X_m = \omega_b L_m \tag{4.10a}$$

$$X_{ls} = \omega_b L_{ls} \tag{4.10b}$$

$$X_{lr} = \omega_b L_{lr} \tag{4.10c}$$

L_m, L_{ls}, and L_{lr} are the mutual inductance, stator leakage inductance, and rotor leakage inductance, respectively. The current equations are obtained by expressing Equations (4.9) as a function of the flux linkages.

$$i_{qs}^e = \frac{F_{qs}^e - F_{qm}^e}{X_{ls}} \tag{4.11a}$$

$$i_{qr}^e = \frac{F_{qr}^e - F_{qm}^e}{X_{lr}} \tag{4.11b}$$

$$i_{ds}^e = \frac{F_{ds}^e - F_{dm}^e}{X_{ls}} \tag{4.11c}$$

$$i_{dr}^e = \frac{F_{dr}^e - F_{dm}^e}{X_{lr}} \tag{4.11d}$$

$$F_{qm}^e = X_m(i_{qs}^e + i_{qr}^e) \tag{4.11e}$$

$$F_{dm}^e = X_m(i_{ds}^e + i_{dr}^e) \tag{4.11f}$$

where F_{qm}^e and F_{dm}^e are the direct and quadrature magnetizing flux linkages. The current and equations, Equations (4.11), are substituted into the voltage equations (4.8)

to obtain:

$$v_{qs}^e = \frac{R_s}{X_{ls}}(F_{qs}^e - F_{qm}^e) + \frac{1}{\omega_b}\frac{d}{dt}F_{qs}^e + \frac{\omega_e}{\omega_b}F_{ds}^e \tag{4.12a}$$

$$v_{ds}^e = \frac{R_s}{X_{lr}}(F_{ds}^e - F_{dm}^e) + \frac{1}{\omega_b}\frac{d}{dt}F_{ds}^e - \frac{\omega_e}{\omega_b}F_{qs}^e \tag{4.12b}$$

$$0 = \frac{R_r}{X_{lr}}(F_{qr}^e - F_{qm}^e) + \frac{1}{\omega_b}\frac{d}{dt}F_{qr}^e + \frac{(\omega_e - \omega_r)}{\omega_b}F_{dr}^e \tag{4.12c}$$

$$0 = \frac{R_r}{X_{lr}}(F_{dr}^e - F_{dm}^e) + \frac{1}{\omega_b}\frac{d}{dt}F_{dr}^e - \frac{(\omega_e - \omega_r)}{\omega_b}F_{qr}^e \tag{4.12d}$$

The magnetizing flux linkages can be expressed in terms of the flux linkages only.

$$F_{qm}^e = X_{m1}\left(\frac{F_{qs}^e}{X_{ls}} + \frac{F_{qr}^e}{X_{lr}}\right) \tag{4.13a}$$

$$F_{dm}^e = X_{m1}\left(\frac{F_{ds}^e}{X_{ls}} + \frac{F_{dr}^e}{X_{lr}}\right) \tag{4.13b}$$

where

$$X_{m1} = (\frac{1}{X_m} + \frac{1}{X_{ls}} + \frac{1}{X_{lr}})^{-1} \tag{4.14}$$

Finally, the stator and rotor's ordinary differential equations for the flux linkages are obtained.

$$\frac{dF_{qs}^e}{dt} = \omega_b\left[v_{qs}^e - \frac{\omega_e}{\omega_b}F_{ds}^e + \frac{R_s}{X_{ls}}\left(F_{qm}^e - F_{qs}^e\right)\right] \tag{4.15a}$$

$$\frac{dF_{ds}^e}{dt} = \omega_b\left[v_{ds}^e - \frac{\omega_e}{\omega_b}F_{qs}^e + \frac{R_s}{X_{ls}}\left(F_{dm}^e - F_{ds}^e\right)\right] \tag{4.15b}$$

$$\frac{dF_{qr}^e}{dt} = \omega_b\left[-\frac{(\omega_e - \omega_r)}{\omega_b}F_{dr}^e + \frac{R_r}{X_{lr}}\left(F_{qm}^e - F_{qr}^e\right)\right] \tag{4.15c}$$

$$\frac{dF_{dr}^e}{dt} = \omega_b\left[\frac{(\omega_e - \omega_r)}{\omega_b}F_{qr}^e + \frac{R_r}{X_{lr}}\left(F_{dm}^e - F_{dr}^e\right)\right] \tag{4.15d}$$

The applied stator voltages are v_{qs}^e and v_{ds}^e. The variables F_{qr}^e and F_{dr}^e denote direct-quadrature components of the rotor flux linkages. Similarly, the variables F_{qs}^e and F_{dr}^s denote direct-quadrature components of the stator flux linkages. The superscript, e, is used to indicate that the variables are expressed in the synchronously rotating reference frame. The subscripts, d and q, denote that the corresponding variable is either the direct d or the quadrature q component.

The induction motor's torque is developed from the interaction between air gap flux

linkages and rotor current which can be expressed as the following vector form.

$$T_e = \frac{3}{2}(\frac{P_p}{2})\bar{F}_m^e \times \bar{I}_r^e \tag{4.16}$$

where $\bar{F}_m^e = [F_{qm}^e \ F_{qm}^e \ 0]$ and $\bar{I}_r^e = [i_{qr}^e \ i_{dr}^e \ 0]$. The torque equation can be expressed in terms of the mutual flux linkages and the rotor currents.

$$T_e = \frac{3}{2}\left(\frac{P_p}{2}\right)\frac{1}{\omega_b}\left(F_{dm}^e i_{qr}^e - F_{qm}^e i_{dr}^e\right) \tag{4.17}$$

The other several torque equations can be derived in terms of the stator flux linkages and currents, and the rotor flux linkages and currents.

$$T_e = \frac{3}{2}\left(\frac{P_p}{2}\right)\frac{1}{\omega_b}\left(F_{ds}^e i_{qs}^e - F_{qs}^e i_{ds}^e\right) \tag{4.18a}$$

$$T_e = \frac{3}{2}\left(\frac{P_p}{2}\right)\frac{1}{\omega_b}\left(F_{qr}^e i_{dr}^e - F_{dr}^e i_{qr}^e\right) \tag{4.18b}$$

Lastly, the motor's angular speed is calculated using

$$\frac{d\omega_r}{dt} = \left(\frac{P_p}{2J_m}\right)(T_e - T_L) \tag{4.19}$$

where J_m is the motor's rotational moment of inertia, P_p is the motor's number of poles, and T_L is the load torque. Equations (4.11) - Equation (4.19) are used in a MapleSim custom component worksheet to develop the induction motor model in MapleSim. This is a straightforward and convenient method to create a model since symbolic equations are directly entered in a MapleSim custom component worksheet. Once all of the motor dynamic equations, parameters, and initial conditions have been entered, the input and output ports for the custom component can be defined. For the MapleSim induction motor model, the input variables are: the reference stator voltage, v_{qs}^e and v_{ds}^e, the angular electrical speed of the input power ω_e, and the disturbance torque T_L. The output variables are: the stator current and flux linkages, and developed motor torque and speed. After setting up the motor model's input and output ports, the MapleSim induction motor model is generated, and it is exported as a Simulink component using a Simulink component generation worksheet in MapleSim. Figure 4.4 shows the exported MapleSim induction motor model in Simulink which is paired with the Clarke and Park transformation blocks. The Simulink implementation shown in Figure 4.4 is used to

validate the MapleSim induction motor model using the motor parameters listed in Table 4.2.
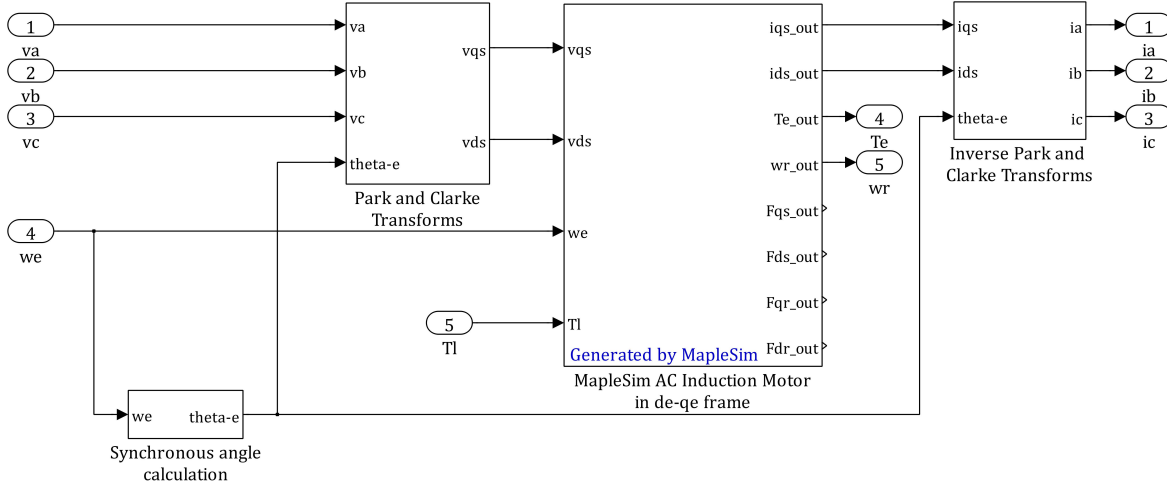
Figure 4.4: MapleSim induction motor model

4.1.5 Implementation and results

To test the MapleSim induction motor model shown in Figure 4.4, the induction motor is simulated in Simulink using the motor parameters listed in Table 4.2. The reference induction motor is a 50 HP machine and its parameters are found in [1]. The MapleSim induction motor model is simulated by applying a 3-phase 380 V at 60 Hz AC signal.

Table 4.2: Induction motor parameters used in the free acceleration simulation

Machine rating				p	R_s	R_r	X_{ls}	X_{lr}	X_m	J_m
hp	volts	rpm	N·m		$[\Omega]$	$[\Omega]$	$[\Omega]$	$[\Omega]$	$[\Omega]$	$[kg{\cdot}m^2]$
50	460	1705	198	4	0.087	0.228	0.302	0.302	13.08	1.662

The induction motor is freely accelerated from stall with no load torque ($T_L = 0$) other than its rotational inertia. The simulation results are displayed in Figure 4.5. One phase of the motor terminal currents, and the output angular speed and torque are plotted. During the motor's acceleration period, the magnitude and frequency of the motor's terminal current is rapidly increasing. As the motor decelerates, the motor current's magnitude and frequency diminishes to a smaller value. The motor accelerates until 2.5 seconds and reaches the steady-state speed which is about 376 rad/s. The oscillations in the motor torque response during initial transitions are caused due to

37

the interaction between the stator and rotor flux linkages [43]. It is important to
check that the motor torque response is in accordance with the response of the motor
currents. The current response's magnitude and frequency increases as the magnitude
of the developed torque increases.
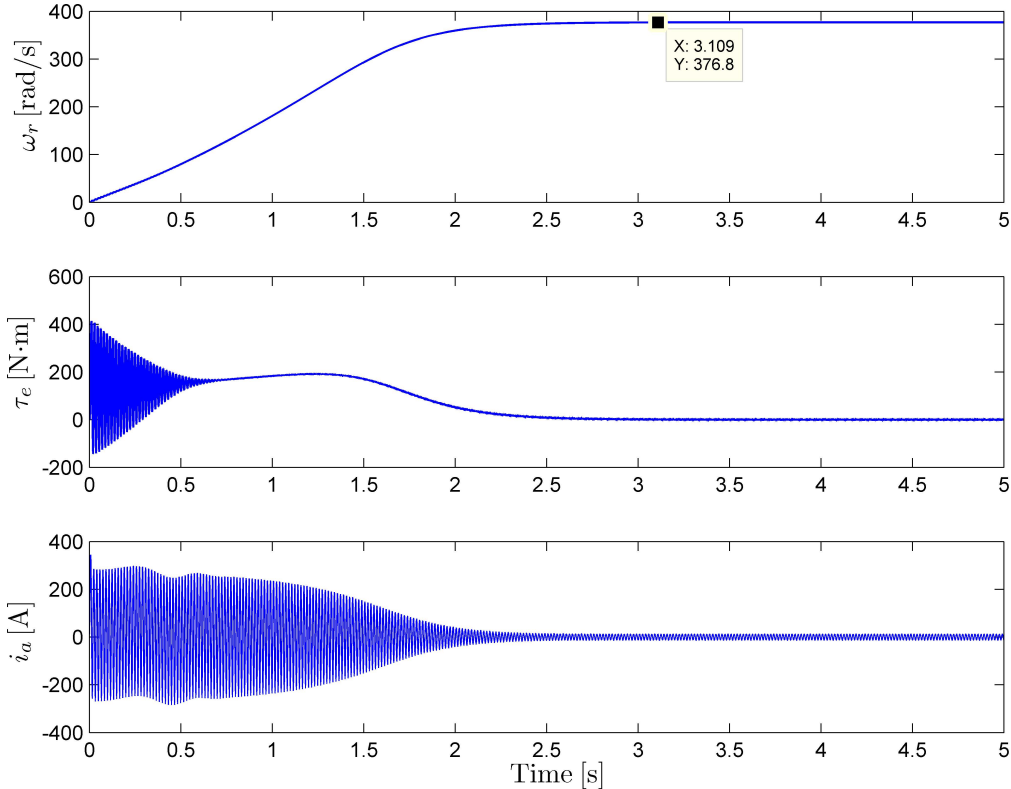
Figure 4.5: Torque and speed profiles during free acceleration simulation

An external load torque is applied to observe the induction motor's dynamic be-
haviour when a load torque is present, and the corresponding simulation results are
shown in Figure 4.6. Initially, the motor has accelerated to its base speed (376 rad/s)
and remains at the base speed until the load torque is applied. The load torque is
first increased from 0 N·m to 190 N·m, which is slightly less than the motor's rated
torque. It remains at 190 N·m for 4 seconds, so that the motor finds the new operating
point. After 4 seconds, the load torque is decreased from 190 N·m to 0 N·m. The
motor's torque response is shown in the second plot of Figure 4.6 where the load torque
is graphically shown using dotted line, and the motor's output is shown using straight
line. When the load torque is first introduced, the motor reacts by increasing its output

torque to overcome the load torque. Since the motor speed is calculated from the difference between the developed torque and load torque, the motor speed decreases until the load torque is present. Also, the motor current response is in accordance with the motor torque response since the motor current increases as the motor torque increases.
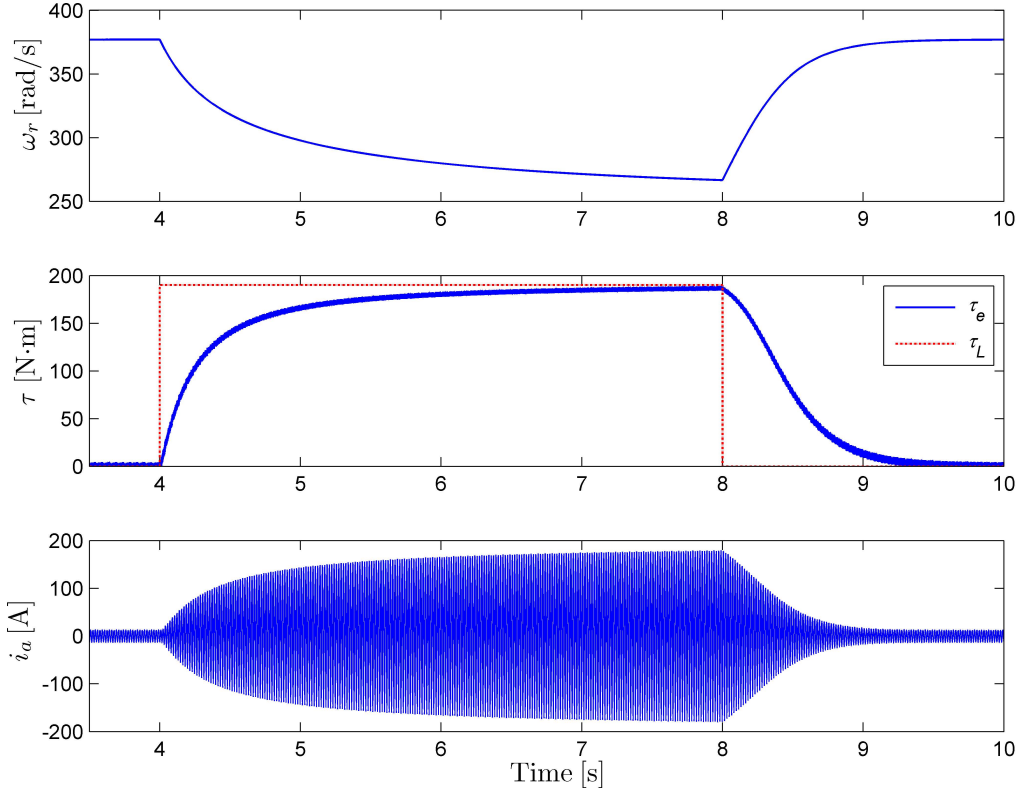
Figure 4.6: Dynamic performance of the induction motor when step load torque is applied

4.2   3-Phase PWM DC/AC Inverter

A DC/AC inverter is needed to convert the battery DC voltage to 3-phase AC voltages which are used by the AC induction motor. Pulse-width modulation (PWM) is the process used to modify a width of output pulse train signals with respect to a control signal [44]. A sinusoidal wave voltage with a desired frequency is used as the PWM's

control signal to generate the output sinusoidal voltage which can be used to power AC machines.

Figure 4.7 shows an example of a three-phase voltage source inverter using power resistors, such as insulated-gate bipolar transistors (IGBT) [44]. To understand operation principles of a 3-phase voltage source inverter, a single-phase voltage source inverter shown in Figure 4.8 is first explained and implemented.
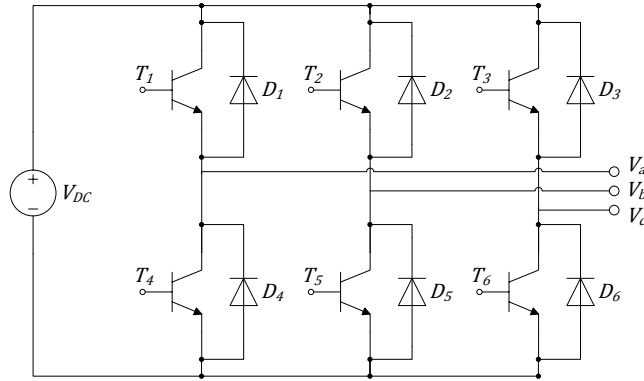
Figure 4.7: A three-phase voltage source inverter

In a PWM inverter, a comparator is used to compare the input voltage $v_{in}(t)$ to a reference signal, and depending on a comparator's result, power transistors are turned on or off. Figure 4.8(a) is a single-phase full bridge voltage source inverter that has two main set of switches, which are T_{1a}, T_{1b}, T_{2a}, and T_{2b} (T_{1a} and T_{1b} are activated/deactivated at the same time). The first comparator, *Comparator 1*, turns on or off the switches, T_{1a} and T_{1b}, based on the result of the following comparison.

- If $v_{in}(t)$ is greater than $v_x(t)$, then turn off T_{1a} and T_{1b}

- If $v_{in}(t)$ is less than $v_x(t)$, then turn on T_{1a} and T_{1b}

The second comparator, *Comparator 2*, compares $v_{in}(t)$ to the second reference voltage $v_y(t)$. It turns on or off the switches, T_{2a} and T_{2b}, based on the same logic explained above. The output of the single-phase voltage source inverter $v_{load}(t)$ is calculated by subtracting $v_u(t)$, which is the voltage across T_{2b} transistor, from $v_v(t)$, which is the voltage across T_{1b}. The two reference voltage signals are shown in Figure 4.8(b). $v_x(t)$ and $v_y(t)$ are triangular waves with the same amplitude and period, but $v_y(t)$ has a 180° phase delay compared to $v_x(t)$.

(a) Construction of a single-phase
voltage source inverter

(b) The reference voltage signals $v_x(t)$
and $v_y(t)$
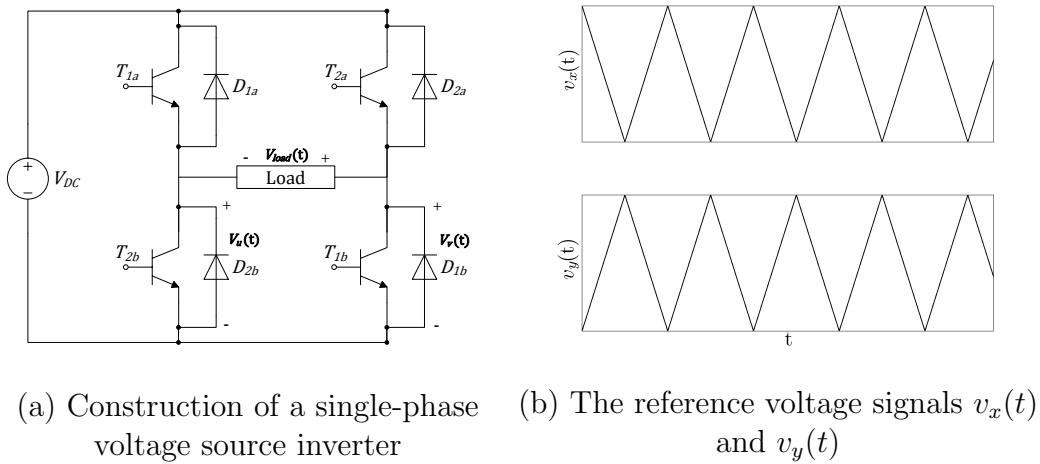
Figure 4.8: A single-phase voltage source inverter

The single-phase voltage source inverter's operation is summarized and shown in Figure 4.9. The voltage across the two resistors (T_{1b} and T_{2b}) are plotted on the first and second plot. By subtracting $v_u(t)$ from $v_v(t)$, the single-phase inverter's output voltage is calculated and plotted on Figure 4.9. Using the single-phase inverter's operational principle, the three-phase voltage source inverter is constructed by assembling three single-phase voltage source inverters together.
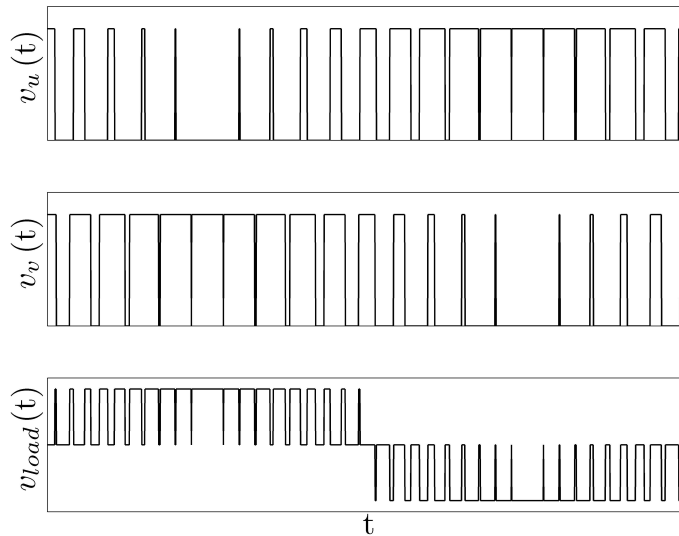
Figure 4.9: Operation of the single-phase voltage source inverter

41

4.2.1 Low pass filter

Since the inverter's load voltage is a chopped AC voltage signal with zero DC components as illustrated in Figure 4.9, a filter is needed to convert the chopped AC voltage signals into smooth sinusoidal waves. To achieve this, a first order ideal low pass filter is first used. The first order low pass filter's transfer function, $H(s)$, is defined as

$$H(s) = \frac{1}{1 + \frac{s}{\omega_c}} \tag{4.20}$$

where ω_c is a cutoff frequency. Since the first order low pass filter is an ideal filter which does not exist in real life, second order low pass filters are frequently used in place of ideal first order low pass filters because they can provide an inexpensive approximation to ideal first order low pass filters [45]. One of the popular low pass filter circuit designs is the Sallen-Key topology [46] which consists of an operational amplifier, resistors and capacitors. The Sallen-key low pass electrical circuit is shown in Figure 4.10, and its second-order transfer function is found from [45].

$$H(s) = \frac{k\omega_c^2}{s^2 + \frac{\omega_c}{Q}s + \omega_c^2} \tag{4.21a}$$

$$\omega_c = \frac{1}{RC} \tag{4.21b}$$

$$Q = \frac{1}{3 - k} \tag{4.21c}$$

Equations (4.21) contains the three filter parameters where k is a gain, and Q is a quality factor. In the case of the Sallen-Key low pass electrical circuit, the cutoff frequency is determined based on the resistance and capacitance.
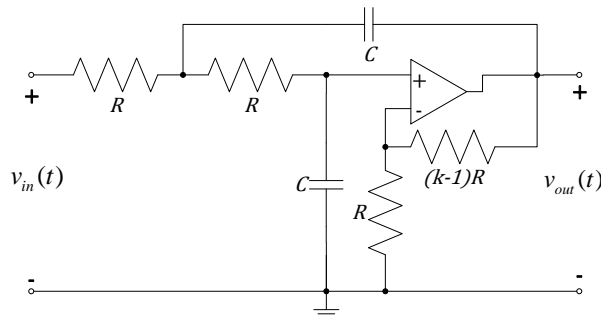
Figure 4.10: Low pass Sallen-Key filter

4.2.2 Implementation and results

The three-phase voltage source inverter is implemented as shown in Figure 4.11. The three single-phase inverter blocks (*T*1-*T*2, *T*3-*T*4, and *T*5-*T*6) in Figure 4.11 are identical except the input voltages are different. Ideal Simulink switches are used in place of the IGBTs as illustrated in Figure 4.11(b).

(a) Simulink three-phase voltage source inverter

(b) Inside of the single-phase inverter block (T1-T2)
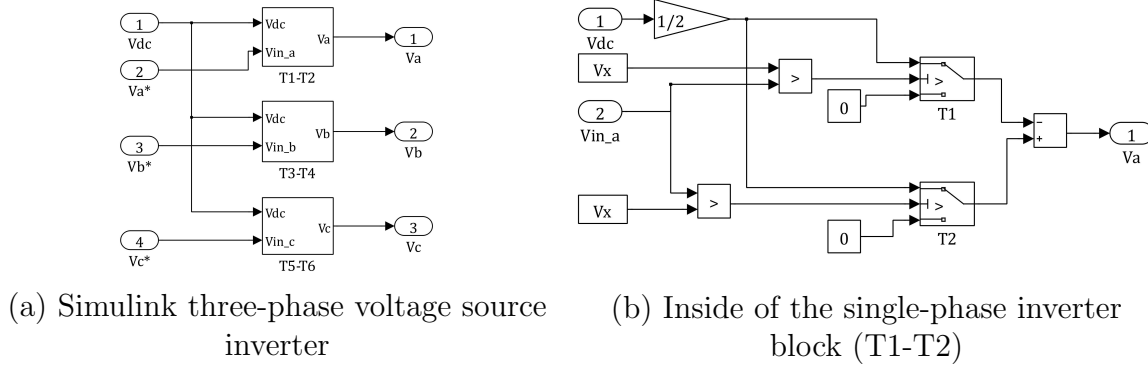
Figure 4.11: Simulink three-phase voltage source inverter

The single-phase voltage source inverter is simulated to convert 100 V DC voltage into one phase AC voltage signal, and its simulation results are shown in Figure 4.12. The two reference voltage signals are triangular waves with unity amplitude and switching frequency of 100 Hz. The control input voltage v_{in} is a sinusoidal wave with unit amplitude and frequency of 10 Hz, and it is depicted as black points in the first plot.
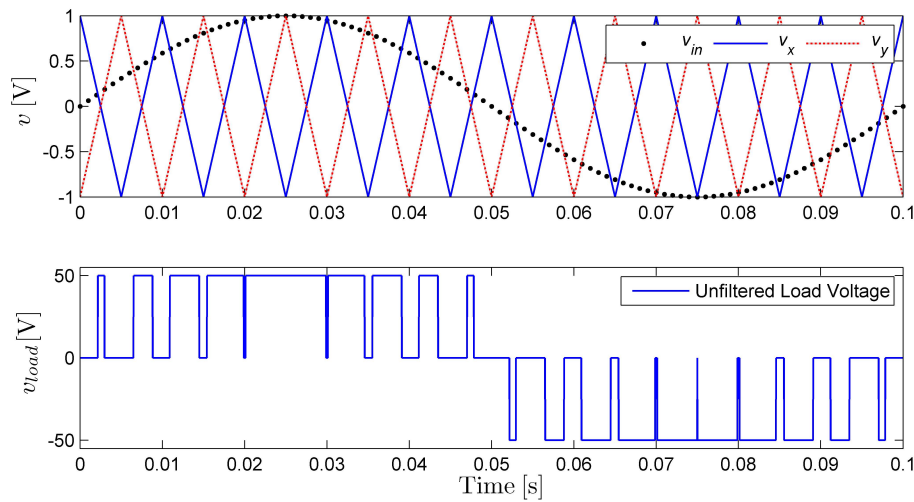
Figure 4.12: Simulation of the single-phase inverter

43

The second plot in Figure 4.12 shows the single-phase inverter's output voltage which looks like chopped AC voltage signals. To apply the single-phase inverter's output voltage to the induction motor, the voltage signals need to be filtered as explained in the previous section. The single-phase inverter with the first order low pass filter is simulated, and the switching frequency of 500 Hz and the cutoff frequency of 75 Hz are used. Figure 4.13 compares unfiltered and filtered voltage signals. The filtered voltage signal lags the ideal voltage signal because an integral term from the low pass filter causes a delay.
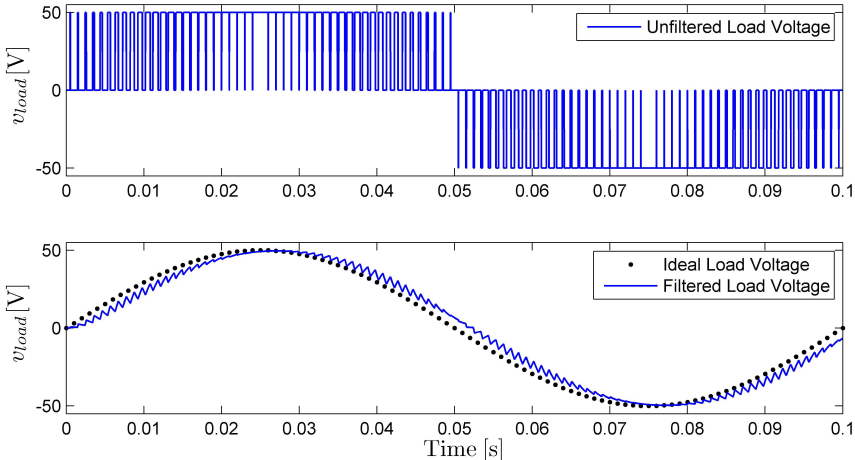
Figure 4.13: Simulation of the single-phase inverter with the low pass filter

Finally, the three-phase voltage source inverter shown in Figure 4.11 with the low pass filter is simulated to convert a 100 V DC voltage signal to 3-phase AC voltage signals. The same switching and cut-off frequencies from the previous simulation are used, and the three-phase inverted and filtered voltage signals are shown in Figure 4.14.
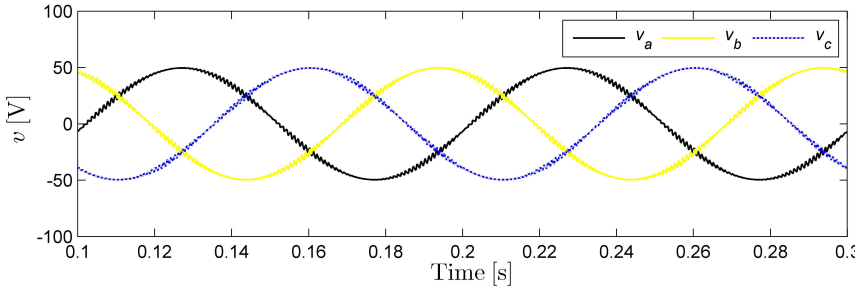
Figure 4.14: Simulation results – 3-phase DC/AC voltage source inverter

44

Chapter 5

AC Induction Motor Control

DC electric motors have been widely used for variable speed and torque applications because of their simplicity in motor control [9]. DC motors, however, require frequent maintenance, and they are not suitable for applications like an electric vehicle application where high torque and speed responses are needed. An open loop constant Voltages per Hertz (V/Hz) is a scalar controller for AC machines, and it is widely used as the variable speed drive when high dynamic performance from an AC motor is not required. But, the open loop V/Hz controller's performance is limited, and it is negatively influenced by the inherent coupling effects that exist in AC motors where torque and flux linkages are functions of voltage or current and frequency [2].
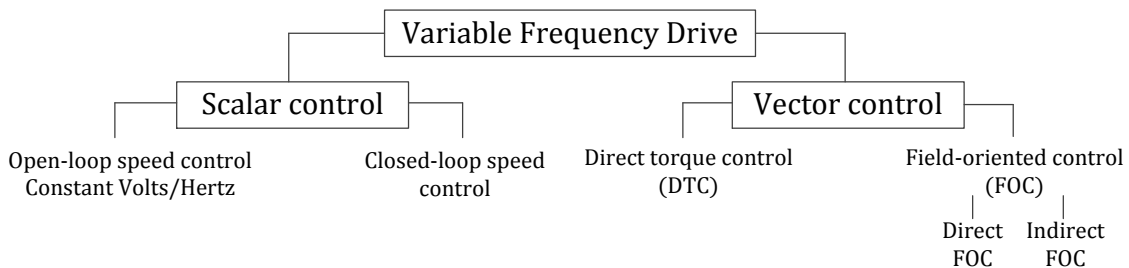
Figure 5.1: Overview of the various VFD controllers for AC motors

The introduction of vector control in the beginning of the 1970s increased the AC motor's popularity for variable speed applications. Vector-controlled AC motors could be operated like a DC motor [2] where torque and field components are independent from one another. Field-oriented control (FOC), that is a sub-branch of vector control, was first proposed by F. Blaschke [4] and K. Hasse [5]. F. Blaschke invented direct FOC, and K. Hasse is credited with the invention of indirect FOC. Direct and indirect

FOC have similar structures other than the method used to estimate the synchronous speed.

In this Chapter, a separately excited DC motor's structure and its control principle are discussed. The open loop V/Hz controller is implemented to control the speed of the induction motor model developed in Chapter 4. Lastly, the indirect FOC controllers are implemented and explained in the last section.

5.1   DC motor operation and control

A separately excited DC motor's cutout and electrical circuit representation are shown in Figure 5.2. The field flux, λ_f, is generated from the field component of the motor's electrical circuit. The field flux is aligned with the stator's d^s-axis as depicted in Figure 5.2(a). The commutator in the DC motor produces the armature current i_a in the rotor winding that is always aligned with the stator's q^s-axis. Since i_a and λ_f are decoupled in nature and the two vectors are always orthogonal to each other, they can be controlled independently [41]. This implies that the DC motor's torque can be controlled by adjusting its torque component i_a without affecting its flux. Similarly, the field current i_f can be controlled by adjusting its field component λ_f only.
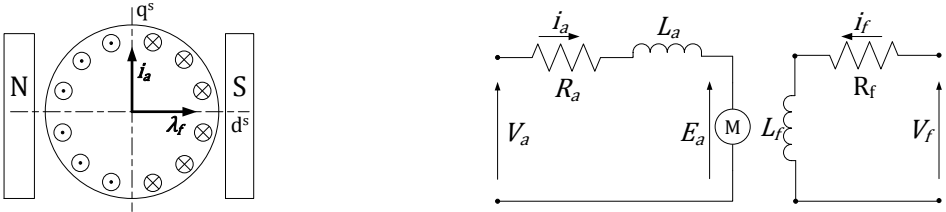
(a) Simplified representation of a DC motor

(b) A separately excited DC motor's electrical circuit

Figure 5.2: Graphical representation of a DC motor

The separately excited DC motor's developed torque is defined as

$$T_m = k_T \lambda_f i_a \tag{5.1}$$

where k_T is a motor torque constant.

5.2 Scalar speed control – open loop Volts/Hertz

Scalar control is used when high dynamic performance from AC motors is not required, such as controlling the speed of pumps and ventilators [34, 35]. Open loop constant V/Hz control is frequently used in industry due to its simplicity and ease of implementation. The speed controller can be implemented on synchronous and asynchronous AC motors without many modifications [35]. As the name of the controller indicates, it is an open loop feed-forward controller where the controller does not require any feedback signals. The main goal of the open loop constant V/Hz controller is to maintain constant rated stator flux density while changing the motor speed by varying the applied stator voltage and frequency.

From the steady-state stator voltage equation of the AC machine explained by Szabó et al. [35], the following expression is derived:

$$\lambda_s = \frac{1}{2\pi} \frac{V_s}{f_s} \tag{5.2}$$

where λ_s is the stator flux, V_s is the stator voltage, and f_s is the stator reference frequency. To keep the stator flux constant, the stator voltage and frequency need to be increased or decreased at the same rate.

The following equation is used to determine the reference stator voltage:

$$v_s^* = \frac{\omega_e^*}{\omega_{rated}} = \frac{1}{2\pi f_{rated}} \omega_e^* \tag{5.3}$$

where ω_e^* and ω_{rated} are the motor's synchronous and rated angular speed. The open loop constant V/Hz controller's block diagram is shown in Figure 5.3.

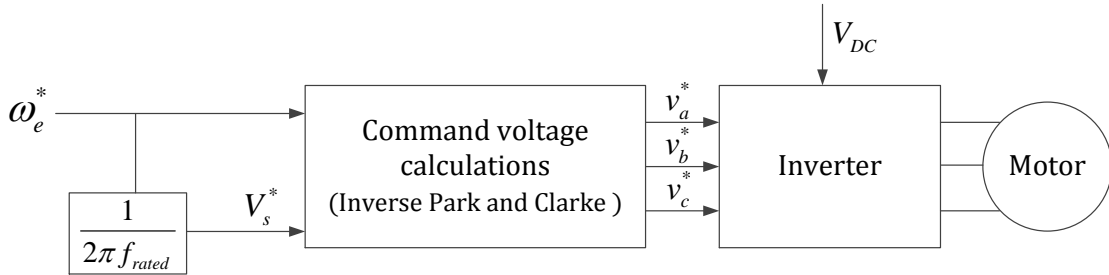Figure 5.3: Open loop V/Hz speed controller

The reference synchronous speed ω_e^* is used as the reference speed input to control the rotor's angular speed ω_r. From the synchronous speed equation (Equation (4.3)), the synchronous speed is calculated by subtracting the slip speed from the rotor angular speed. The slip speed is usually within 5% of the synchronous speed for typical AC motors [41]. Since the synchronous and rotor speed are approximately equal, using the synchronous speed as the reference speed input has the effect of controlling the rotor angular speed. Using Equation (5.3) and Figure 5.3, the open loop constant V/Hz controller is implemented with the AC induction motor and 3-phase voltage source inverter models explained in Chapter 4. The reference speed input is the desired motor's synchronous speed ω_e^* which is converted to the reference stator voltage using Equation (5.3).
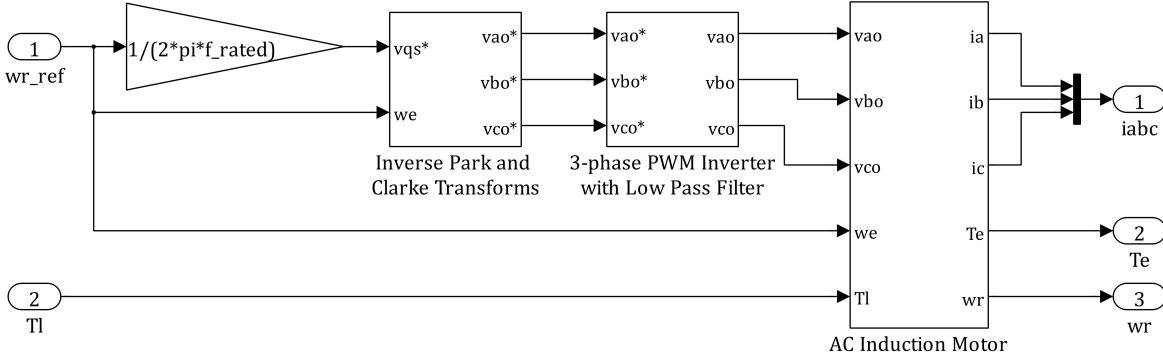
Figure 5.4: Implementation of the open loop V/Hz controller in Simulink

Figure 5.4 shows the Simulink implementation, and its simulation results are shown in Figure 5.5. The reference input, the desired motor's synchronous speed, is highlighted in the second plot using a dotted line. The open loop constant V/Hz controller has a good speed tracking performance when the desired motor's synchronous speed is high. When the step load torque is introduced, the motor reacts accordingly by producing an extra amount of torque to overcome the load torque. The controller's speed tracking performance, however, becomes poor when the reference synchronous speed is low. During the initial start up period which is from 0 to 5 seconds, the motor fails to follow the reference speed, and also, the corresponding developed torque abruptly fluctuates during that period. This is the main drawback of the open loop constant V/Hz control, which makes the controller not suitable for controlling the motor at low speed. When the motor is operating at low speed, the magnitude of the voltage-drop is of comparable magnitude to the computed reference stator voltage which leads to poor speed tracking performance at a low speed [35].
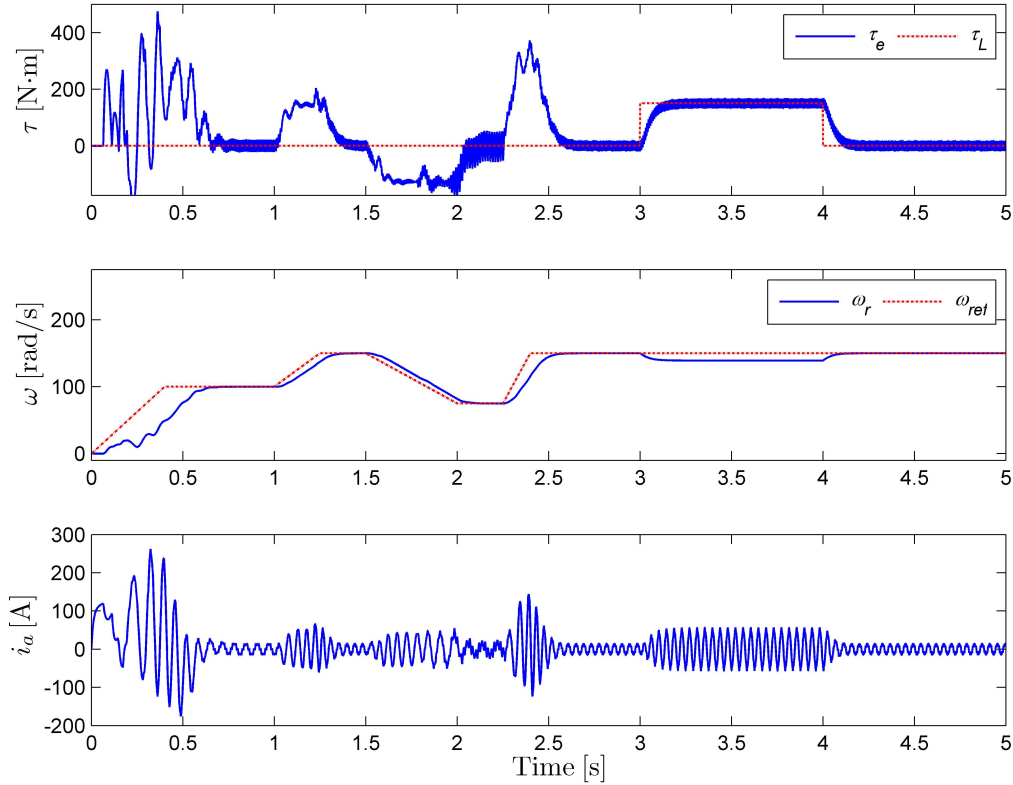
Figure 5.5: Simulation results of the open loop V/Hz controller

5.3 Vector control – field-oriented control

The induction motor's torque equations (Equations (4.18)) in terms of the stator and rotor variables were defined in Chapter 4. Expressing the torque equation using the synchronously rotating reference frame explains the possible relationship between the separately excited DC motor and the vector-controlled AC induction motor, and benefits of using the vector control technique. Using the synchronously rotating reference shown in Figure 5.6, the stator or air gap flux linkage ψ_s^s vector is aligned with the d^e-axis of the d^e-q^e frame. Thus, the direct stator flux linkage expressed in the d^e-q^e frame, ψ_{ds}^e, is equal to ψ_s^s whereas the quadrature stator flux linkage expressed in the d^e-q^e frame, ψ_{qs}^e, is equal to zero.

Since ψ_{qs}^e is equal to zero, the torque equation defined in Equation (4.18)(a) can be
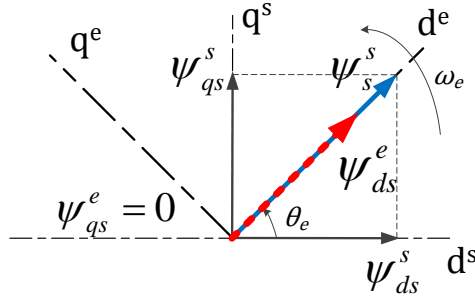
Figure 5.6: ψ_s^s aligned with synchronosuly rotating reference frame

rewritten as

$$T_e = k_T \psi_{ds}^e i_{qs}^e \tag{5.4a}$$

$$k_T = \frac{3}{2}\left(\frac{P_p}{2}\right) \tag{5.4b}$$

where k_T is an induction motor equivalent motor torque constant. The redefined torque equation resembles the separately excited DC motor torque equation shown in Equation (5.1) where ψ_{ds}^e and i_{qs}^e correspond to the field and torque components of the induction motor. From the separately excited DC motor's operation principle discussed in Section 5.1, the DC motor's torque and field components are found to be decoupled in nature. They could be controlled independently without affecting the developed torque or the field current. By referring to the induction motor variables in the d^e-q^e frame, the field component ψ_{ds}^e and torque component i_{qs}^e are decoupled since ψ_{ds}^e is aligned with the d^e-axis, and i_{qs}^e is aligned with the q^e-axis as shown in Figure 5.6. Thus, the vector controlled induction motor can be operated like a DC motor where good torque and speed performances are expected for variable speed and torque applications. The list of key steps taken during the FOC is shown below.

1. Depending on the type of controller, such as a speed or torque controller, calculate the reference components, v_{qs}^e and v_{ds}^e, in the synchronously rotating reference frame using the reference inputs, T_{ref} or ω_{ref}, and ψ_{ref}.

2. Find the angular position of the rotor θ_r, and update the synchronously rotating reference frame angle θ_e.

3. Using the inverse Park and Clarke transformations with θ_e, convert v_{qs}^e and v_{ds}^e into v_a, v_b, and v_c which become the inputs to the 3-phase voltage source inverter.

5.3.1   Indirect field-oriented speed controller

In the area of field-oriented control, there are the two main control techniques: direct and indirect field-oriented control [4, 42]. Direct field-oriented (DFO) control utilizes magnetic feedback information to estimate the synchronous speed. The alternative approach to DFO control is indirect field-oriented (IFO) control. The rotor's angular position is used as the feedback information where an encoder is used to measure the rotor's angular speed, and the synchronous speed is calculated by adding the rotor's angular speed to the estimated slip speed. Generally, the velocity feedback signal is a cleaner signal than a magnetic feedback signal, so IFO control is inherently more robust than DFO control [47].

The rotor's angular position is determined by integrating the angular speed of the rotor.

$$\theta_r = \int \omega_r dt \tag{5.5}$$

Having the accurate synchronous speed is very important since the synchronous angle is used in the Park transformation to convert three-phase stationary signals into two-phase synchronously rotating signals. The synchronous speed is estimated by adding the slip speed to the angular speed of the rotor. The slip speed ω_{sl} is estimated by

$$\omega_{sl} = \frac{L_m R_r}{L_r \psi_{ref}} i_{qs}^{e} {}^* \tag{5.6}$$

where i_{qs}^{e*} is the reference quadrature component of the stator current calculated from the controllers that will be explained in the following sections. Lastly, ψ_{ref} is the reference rotor flux linkage. The derivation of the slip speed estimation is shown in the following subsection called the flux linkage estimation.

Finally, the synchronous angle is calculated by integrating Equation (4.3).

$$\theta_e = \int (\omega_r + \omega_{sl}) dt \tag{5.7}$$

The overall IFO speed control architecture is shown in Figure 5.7. There are four main control blocks used in IFO speed control: the flux and velocity controllers, and V^d and V^q regulators.
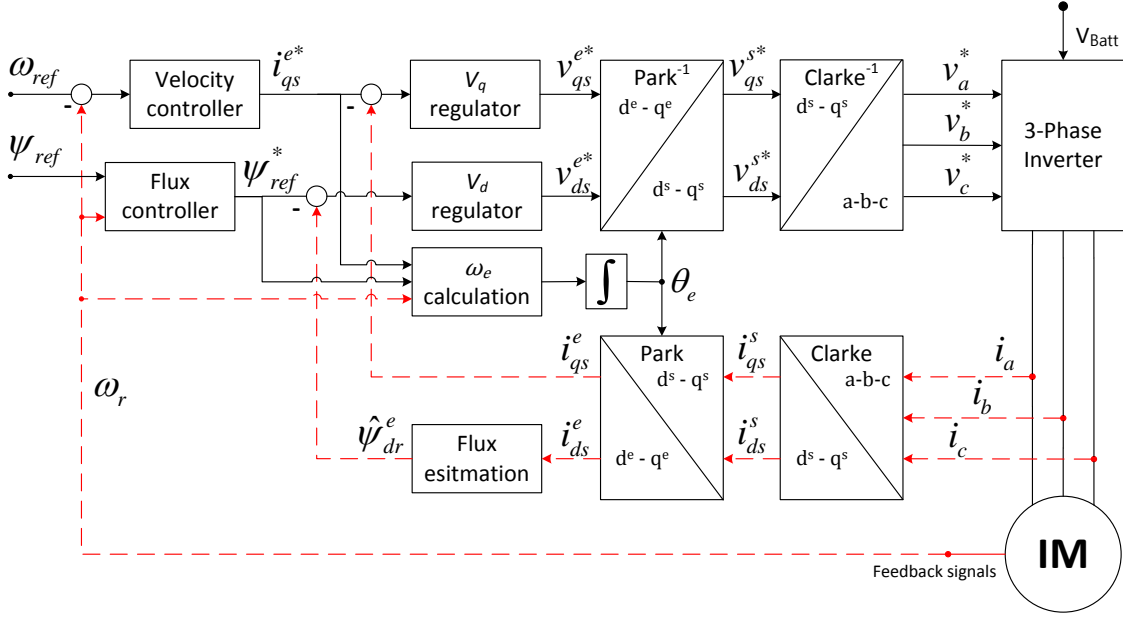
Figure 5.7: Overall indirect field-oriented speed control architecture

Flux controller

The induction motor's torque output is constant up to the base (rated) speed, and this region is called the *constant torque area*. However, when the induction motor rotates faster than its base speed, the motor torque gradually decreases due to a reduced magnetic field in the motor. This region is called the *field weakening region*, and the motor power is constant in the region. Equation (5.8) is used to calculate the adjusted reference flux linkage ψ^*_{ref} based on the motor's angular speed ω_r and its base speed ω_b, and the equation is also used in [33, 41].

$$
\psi^*_{ref} = \begin{cases} \psi_{ref}, & \text{if } \omega_m \leq \omega_b. \\ \frac{\omega_b}{|\omega_r|}\psi_{ref}, & \text{otherwise.} \end{cases} \tag{5.8}
$$

The adjusted reference flux ensures that the stator voltage remains under its rated value while the motor is operating in the field weakening region. The flux controller block shown in Figure 5.7 receives two inputs which are the reference flux linkage ψ_{ref}, and the rotor's angular speed ω_r, and they are used to calculate the adjusted reference flux linkage. Equation (5.8) has limitations if the adjusted reference flux linkage needs to be decreased at a faster rate. This can be overcome by using an exponential function with

a negative power. The equation is modified to incorporate the exponential function and the constant K_f to calculate the adjusted reference flux linkage.

$$\psi_{ref}^* = \begin{cases} \psi_{ref}, & \text{if } \omega_m \leq \omega_b. \\ e^{\frac{K_f(\omega_b - |\omega_r|)}{\omega_b}} \psi_{ref}, & \text{otherwise.} \end{cases} \tag{5.9}$$

where K_f is a constant used to change the rate of decrease of ψ_{ref}^* in the field weakening region. For the motor's angular speed plotted in Figure 5.8, Equation (5.8) and Equation (5.9) are used to calculate the adjusted reference flux linkages. The base speed is 378 rad/s (60 Hz), so the adjusted reference flux linkage is constant up to the base speed, and it starts to decrease when the motor is rotating faster than the base speed. Using Equation (5.9) with different values of K_f, various ψ_{ref}^* profiles are possible as shown in Figure 5.8.
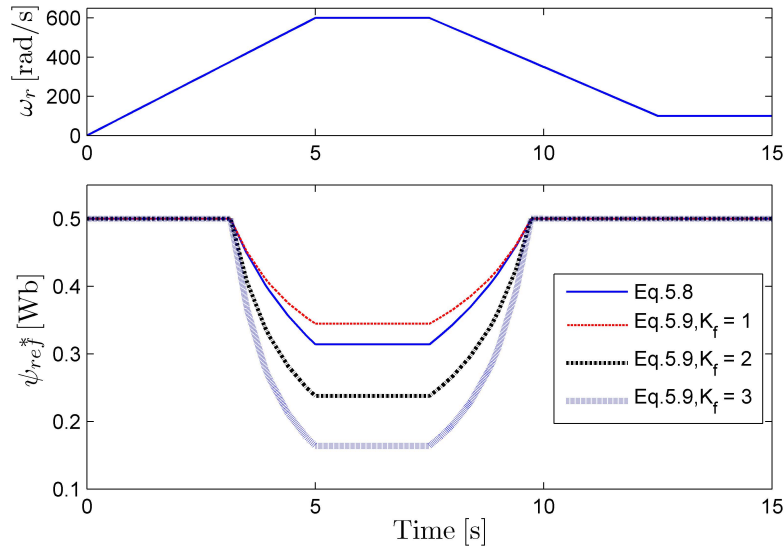

Figure 5.8: Adjusted reference flux linkage profiles using the different gains

Velocity controller

The velocity controller uses a proportional-integral (PI) controller to calculate the reference quadrature stator current in the synchronously rotating reference frame.

$$i_{qs}^{e\ *} = (K_{pv} + \frac{K_{iv}}{s})(\omega_{ref} - \omega_r) \tag{5.10}$$

53

where K_{p_v} and K_{iv} are the PI controller's proportional and integral gains.

V^d and V^q regulators

The V^d regulator uses a PI controller to calculate the reference direct stator voltage in the synchronously rotating reference frame.

$$v_{ds}^{e\,*} = (K_{pd} + \frac{K_{id}}{s})(\lambda_{ref}^* - \lambda_{ref}) \tag{5.11}$$

where K_{pd} and K_{id} are the PI controller's proportional and integral gains. The V^q regulator also uses a PI controller to calculate the reference quadrature stator voltage in the synchronously rotating reference frame.

$$v_{qs}^{e\,*} = (K_{pq} + \frac{K_{iq}}{s})(i_{qs}^{e\,*} - i_{qs}^e) \tag{5.12}$$

where K_{pq} and K_{iq} are the PI controller's proportional and integral gains.

Flux linkage estimation

Flux linkages are estimated since they are hard to measure, and for the case of the rotor flux linkages, it may not be accessible for instrumenting sensors to measure rotor flux linkages. Thus, the rotor flux linkages are estimated using the induction motor's voltage equations derived in Chapter 4. Since it is more convenient to measure data from the stator (stationary component of the motor) than the rotor (rotating component), it is desirable to estimate the flux linkages using the stator variables, such as the stator currents. This flux linkage estimation method is used for rotor flux-based IFO control only. K. Bose [2] presented the rotor flux linkage estimation for rotor flux-based IFO control, and he also showed the stator flux linkage estimation method for stator flux-based DFO control.

The rotor's voltage equations are listed in Equations (5.13). In case of a squirrel cage induction motor, v_{qr}^e and v_{dr}^e are equal to zero.

$$v_{qr}^e = R_r i_{qr}^e + \frac{d}{dt}\psi_{qr}^e + (\omega_e - \omega_r)\psi_{dr}^e = 0 \tag{5.13a}$$

$$v_{dr}^e = R_r i_{dr}^e + \frac{d}{dt}\psi_{dr}^e - (\omega_e - \omega_r)\psi_{qr}^e = 0 \tag{5.13b}$$

The rotor flux linkage equations from Chapter 4 were

$$\psi^e_{qr} = \frac{F^e_{qr}}{\omega_b} = \frac{(X_{lr} + X_m)}{\omega_b} i^e_{qr} + \frac{X_m}{\omega_b} i^e_{qs} \tag{5.14a}$$

$$\psi^e_{dr} = \frac{F^e_{dr}}{\omega_b} = \frac{(X_{lr} + X_m)}{\omega_b} i^e_{dr} + \frac{X_m}{\omega_b} i^e_{ds} \tag{5.14b}$$

The above equations can be simplified since $L_r = \frac{(X_{lr}+X_m)}{\omega_b}$ and $L_m = \frac{X_m}{\omega_b}$, and they are rewritten as

$$i^e_{qr} = \frac{\psi^e_{qr}}{L_r} - \frac{L_m}{L_r} i^e_{qs} \tag{5.15a}$$

$$i^e_{dr} = \frac{\psi^e_{dr}}{L_r} - \frac{L_m}{L_r} i^e_{ds} \tag{5.15b}$$

Since the rotor currents are inaccessible for measurements, i^e_{qr} and i^e_{dr} in Equations (5.13) are replaced using Equations (5.15).

$$R_r \frac{\psi^e_{qr}}{L_r} - R_r \frac{L_m}{L_r} i^e_{qs} + \frac{d}{dt}\psi^e_{qr} + (\omega_e - \omega_r)\psi^e_{dr} = 0 \tag{5.16a}$$

$$R_r \frac{\psi^e_{dr}}{L_r} - R_r \frac{L_m}{L_r} i^e_{ds} + \frac{d}{dt}\psi^e_{dr} - (\omega_e - \omega_r)\psi^e_{qr} = 0 \tag{5.16b}$$

When the rotor variables are referred to in the synchronously rotating reference frame, the direct rotor flux linkage ψ^s_r is aligned with the d^e-axis which makes ψ^e_{qr} equal to zero. Equations (5.16) can be simplified by equating ψ^e_{qr} and $\dot{\psi}^e_{qr}$ to zero. Using Equation (5.16)(a), the expression for estimating the rotor flux linkages is

$$\frac{d\hat{\psi}^e_{dr}}{dt} + \frac{R_r}{L_r}\hat{\psi}^e_{dr} = R_r \frac{L_m}{L_r} i^e_{ds} \tag{5.17}$$

The equation for estimating slip speed is found from Equation (5.16)(b) by setting ψ^e_{qr} and $\dot{\psi}^e_{qr}$ equal to zero.

$$\omega_{sl} = \omega_e - \omega_r = \frac{L_m R_r}{L_r \psi^e_{dr}} i^e_{qs} \tag{5.18}$$

5.3.2   Indirect field-oriented torque controller

The goal of the IFO speed controller explained in Section 5.3.1 is to force the induction motor to follow the reference angular speed input as shown in Figure 5.7. To simulate

a vehicle model for different drive cycles, a driver controller, such as a proportional-integral-derivative controller, is commonly used to make a vehicle to follow reference drive cycles. The output of the driver controller is the reference motor torque which becomes one of the inputs in the drivetrain system. It is necessary to have the reference motor torque as the input instead of the reference speed which was used in the previous section. The IFO speed controller is modified and renamed as the IFO torque controller where it takes the reference motor torque as the input.

In the IFO speed controller, the motor speed ω_r and estimated rotor flux linkage $\hat{\psi}_{dr}^e$ are used as the feedback signals. For the IFO torque controller, the velocity controller is replaced with the torque controller, and the developed motor torque τ_e is added to the list of feedback signals. Similar to the velocity controller, a PI controller is used in the torque controller to calculate the reference quadrature stator current $i_{qs}^{e}{}^*$. The structure of V^d and V^q regulators remain identical, but the PI controller gains are modified. The overall IFO torque architecture is shown in Figure 5.9.
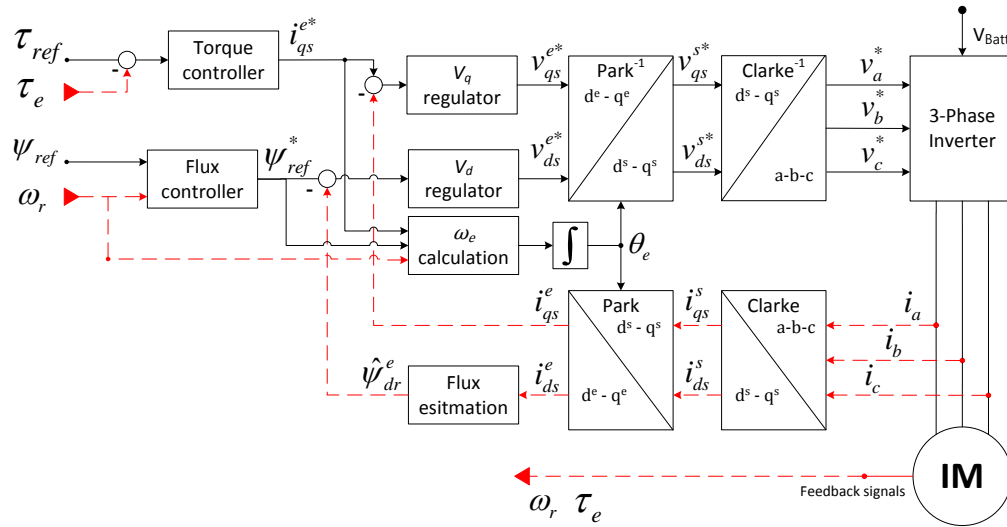

Figure 5.9: Overall indirect field-oriented torque control architecture

Torque controller

The torque controller uses a PI controller to calculate the reference quadrature stator current in the synchronously rotating reference frame.

$$i_{qs}^{e}{}^* = (K_{p_t} + \frac{K_{it}}{s})(\tau_{ref} - \tau_e) \tag{5.19}$$

56

where K_{p_t} and K_{it} are the PI controller's proportional and integral gains.

5.3.3 Implementation and results

The IFO speed and torque controllers explained in the previous sections are implemented in Simulink. The speed controller's implementation is explained in detail, and the simulation results are shown to verify that the controller is working properly. The IFO torque controller adopts identical components from the IFO speed controller, so its implementation is similar to the IFO speed controller with few modifications. The IFO torque controller's simulation results are discussed thoroughly, and the impact of the flux controller in the IFO torque controller is highlighted.

IFO speed controller implementation

Figure 5.10 shows the IFO speed controller implementation in Simulink. The grey coloured signals in Figure 5.10(a) are the feedback signals from the induction motor. The motor's angular speed, the quadrature stator current, and the direct stator flux linkage are used as the feedback signals. The structure of the velocity controller, and the V^q and V^d regulators are similar, so only the velocity controller's structure is shown in Figure 5.10(b).
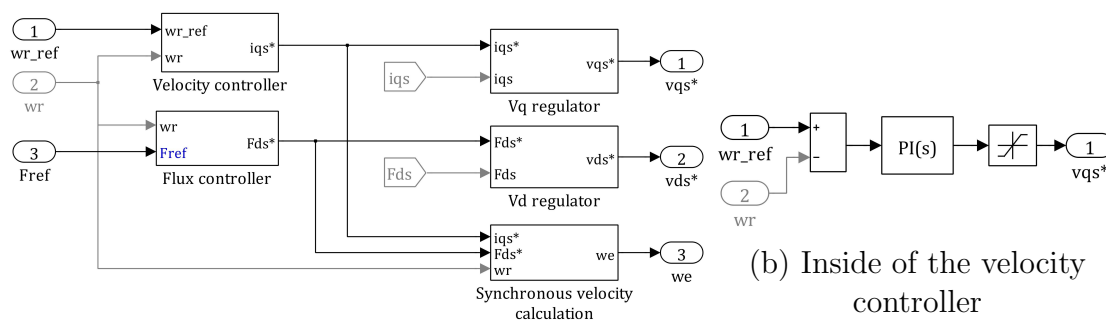
(a) The four controllers that are used to control the
motor's angular speed

(b) Inside of the velocity
controller

Figure 5.10: Main controllers in the IFO speed control

The internal structure of the synchronous speed calculation and flux controller blocks are shown in Figure 5.11, and they are implemented using Equation (4.3), Equation (5.6) and Equation (5.8), respectively.

Using the controllers explained in this section, the electrical powertrain system with the IFO speed controller is simulated in Simulink where the main goal is to follow a

(a) Inside of the synchronous speed
calculation block
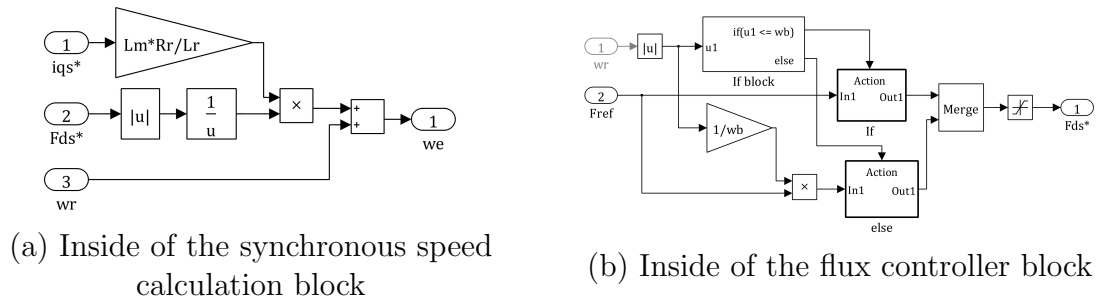

(b) Inside of the flux controller block

Figure 5.11: Synchronous speed calculation and flux controller blocks

specific reference motor angular speed profile. Figure 5.12 shows the overall system implementation in Simulink where it has four main subsystems: the IFO speed controller, the inverse Park and Clarke transformations, the 3-phase PWM inverter with the low pass filter, and lastly the AC induction motor.
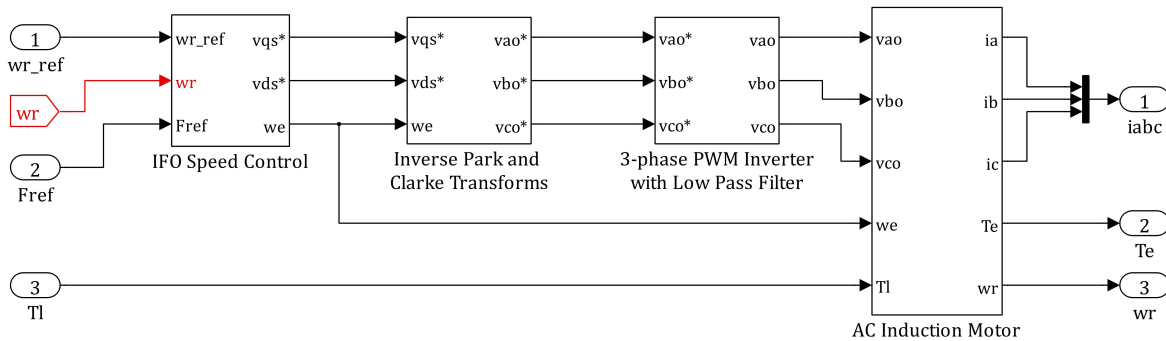
Figure 5.12: IFO speed controller with the electrical powertrain components

IFO speed controller simulation results

The motor parameters shown in Table 4.2 are used in the following simulation. Also, the PI controller gains used in the simulation are listed in Table 5.1 with additional simulation and powertrain parameters.

Table 5.1: PI control gains and additional parameters used in IFO speed controller simulation

PI control gains						Additional parameters		
K_{p_v}	K_{p_d}	K_{p_q}	K_{iv}	K_{id}	K_{iq}	ω_b [Hz]	v_{DC} [V]	ψ_{ref} [Wb]
10	10	10	1	1	1	60	380	0.47

The velocity controller gains, K_{p_v} and K_{iv} are manually tuned through repeated simulation attempts until the error between the reference and rotor angular speed is reduced to a small value. Controlling the V^d regulator's gains, K_{pd} and K_{id}, affect how the estimated flux linkage tracks the reference flux linkage. Similar to the velocity controller's gains, the V^d regulator's gains are manually tuned from repeated simulation trials until the error between the reference and estimated flux linkages has minimized. The reference flux linkage value (0.47 Wb) is obtained from Dilmi et al. [33] where they used an induction motor for hybrid electric vehicle applications. The constant DC voltage is supplied to the inverter with a certain switching frequency. The IFO speed controller's speed tracking performance is excellent since the rotor angular speed tracks the reference angular speed very closely which can be seen from Figure 5.13. The corresponding developed torque τ_e is highly responsive, and the torque response resembles a unit step input when the motor is accelerating.

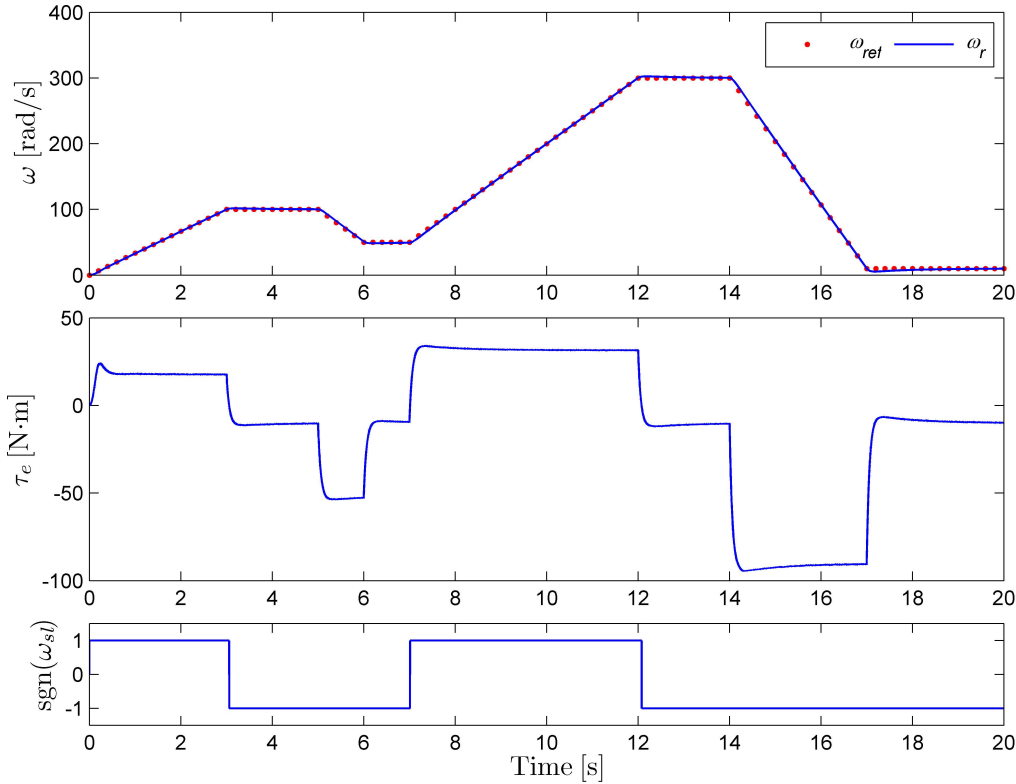Figure 5.13: Simulation results of the electrical powertrain system with the IFO speed controller

The plot of $signum(\omega_{sl})$ is plotted to study the motor's operation modes during the simulation. When the motor is acting as a generator, ω_{sl} is negative, which indicates that the rotor angular speed is faster than the synchronous speed. If ω_{sl} is positive then the motor is operating in the motoring mode, producing positive torque. One phase of the motor currents i_a is plotted in Figure 5.14 to study changes of the motor current when the motor is operating at different speeds. It was seen from the motor torque equation that motor current and torque are related to each other. When the motor is accelerating, the magnitude of developed torque will increase which causes the motor current's magnitude and frequency to increase as seen from Figure 5.14. Once the motor output torque becomes small, the motor current's magnitude and frequency reduces to a smaller value. Also, the estimated flux linkage $\hat{\psi}_{dr}^e$ is plotted with the actual flux linkage ψ_{dr}^e calculated from the MapleSim AC induction motor model. The estimated flux linkage remains around the reference flux linkage value, 0.47 Wb, which indicates that the V^d regulator's performance is satisfactory. The flux linkage estimation equation that was derived in Section 5.3.1 works well since the estimated flux linkage is close to the actual flux linkage as shown in Figure 5.14.
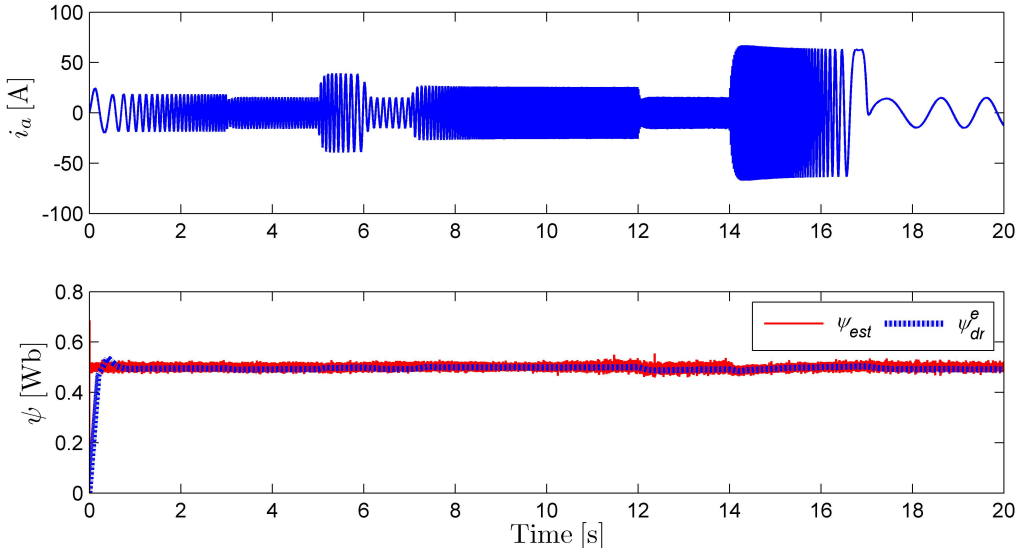

Figure 5.14: Simulation results – the electrical powertrain system with the IFO speed controller

IFO torque controller implementation and results

Similar to the IFO speed controller implementation, the IFO torque controller is implemented with the electrical powertrain components shown in Figure 5.15.
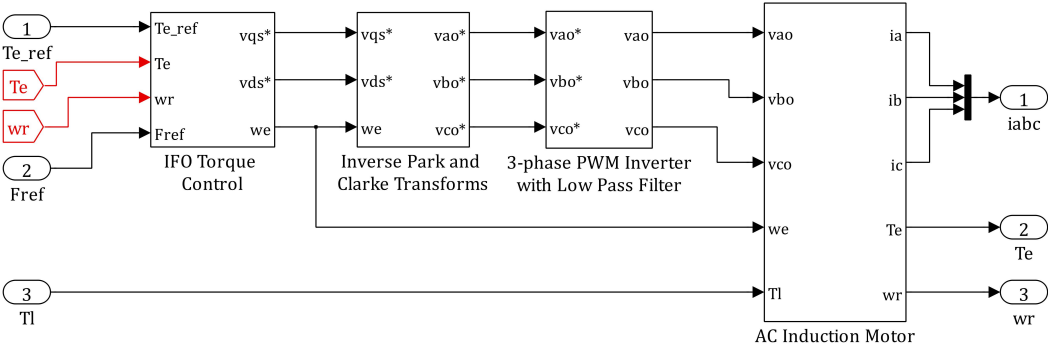
Figure 5.15: IFO torque controller with the electrical powertrain components

The same motor parameters used in the IFO speed controller simulation are used in the IFO torque controller simulation. Initially, the PI controller gains from the IFO speed controller are used as the control gains for the IFO torque controller, and the initial simulation results are shown in Figure 5.16.

Figure 5.16: Initial simulation results – IFO torque controller

The IFO torque controller's performance is satisfactory since the developed torque follows the reference motor torque. However, sharp undershoots are observed when

the torque response undergoes a step change at 2.5 and 4 seconds. Undershoots and overshoots are not desirable for variable torque applications because they can cause unintended outcomes. Undershoots and overshoots can be avoided by changing the torque controller's proportional gain to zero. After setting $K_{pt} = 0$, the torque t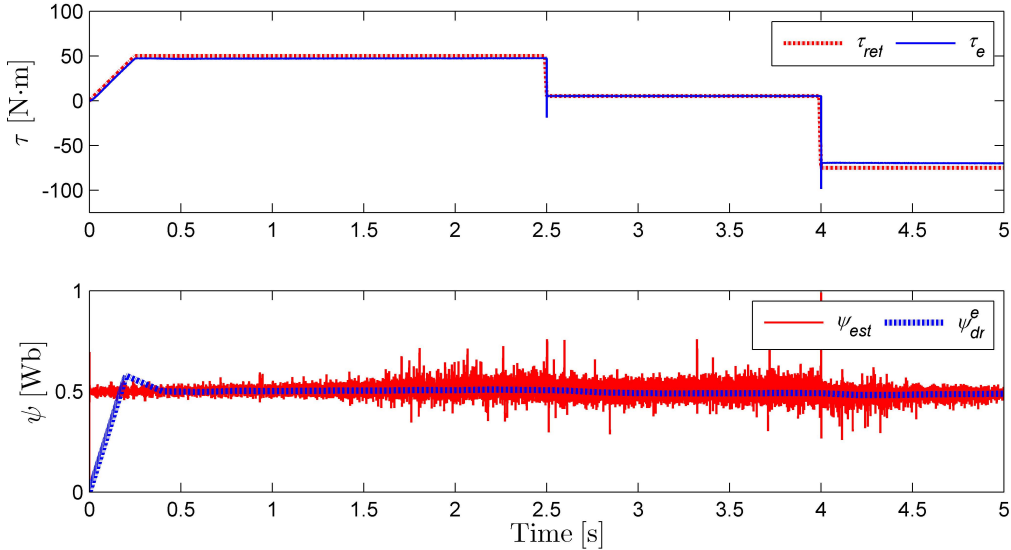racking performance became poor, so K_{it} is increased to improve the torque tracking performance. The value of K_{id} is increased to improve the estimated flux linkage's tracking performance. The modified control gains are listed in Table 5.2.

Table 5.2: Final PI control gains used in the IFO torque controller

PI control gains					
K_{pt}	K_{pd}	K_{pq}	K_{it}	K_{id}	K_{iq}
0	10	10	50	10	1

Using the modified control gains, the undershoots are eliminated from the torque response as displayed in Figure 5.17. Also the estimated flux linkage is proximate to the actual flux linkage as seen from the figure.
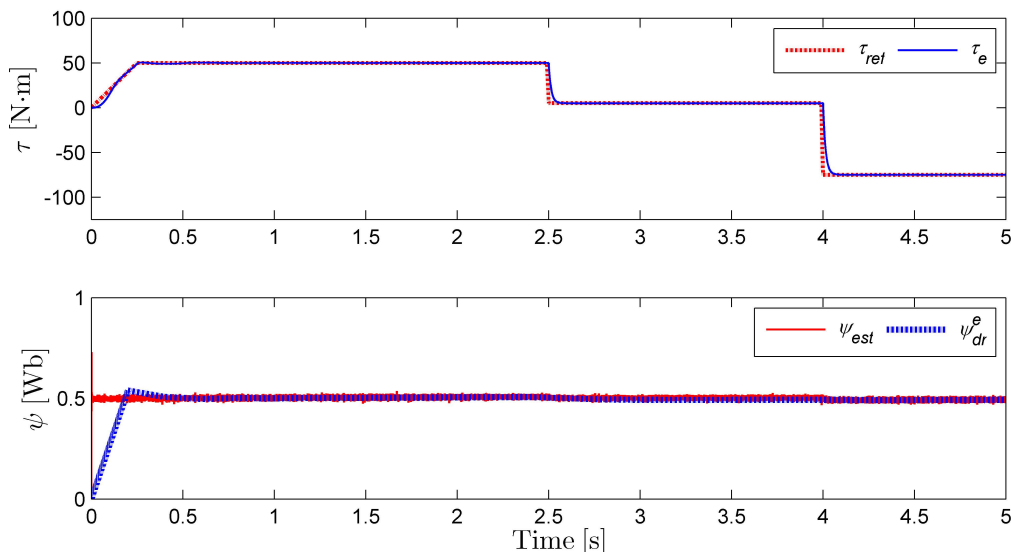

Figure 5.17: Simulation results – IFO torque controller with the modified control gains

The different reference torque input and the final control gains listed in Table 5.2 are used in the following simulation results shown in Figure 5.18. This particular reference torque input is selected because it will make the motor rotate faster than its base or rated speed (ω_b).
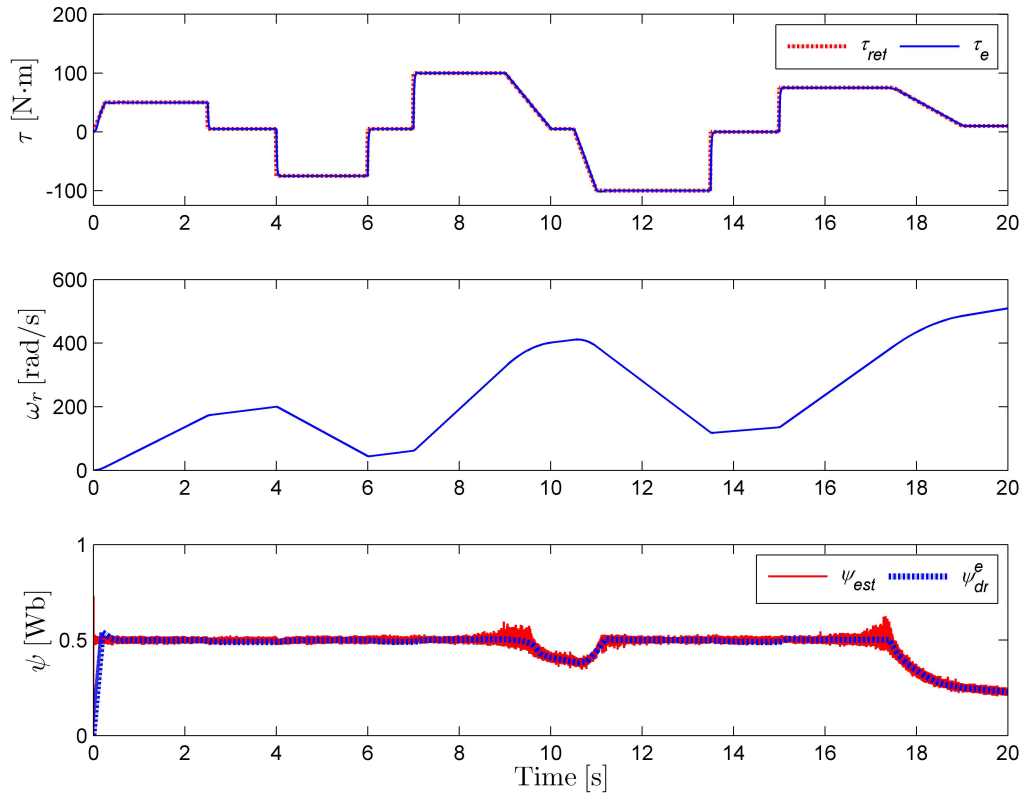
Figure 5.18: Final simulation results – IFO torque controller

The reference flux linkage is plotted at the bottom of Figure 5.18 to show how the flux controller adjusts the reference flux linkage based on the motor's speed. Once the motor exceeds its base speed at about 9 or 17 seconds, the flux controller reduces the reference flux linkage as shown in the figure. To show the effect of the flux controller, the system is simulated without the flux controller, and corresponding simulation results are shown in Figure 5.19. Since the flux controller is excluded from the IFO torque controller, the reference flux is constant regardless of the motor angular speed. The output motor torque abruptly fluctuates at about 17 seconds which is when the motor speed exceeds its base speed. The main function of the flux controller is to decrease the reference flux linkage gradually when the motor speed exceeds its base speed. When the motor rotates faster than its base speed, it is said to be operating in the flux weakening region. In this region, it is necessary to decrease the reference flux linkage to stop the stator voltage from increasing. Figure 5.20 shows the direct and quadrature components of the reference stator voltages during the two previous simulations. It can

be clearly noted that the system without the flux controller has abrupt fluctuations in the reference stator voltages when the motor speed exceeds its base speed. The reference stator voltages displayed on Figure 5.20(a) has no abrupt fluctuations compared to Figure 5.20(b), and this is mainly due to having the flux controller in the IFO torque controller.
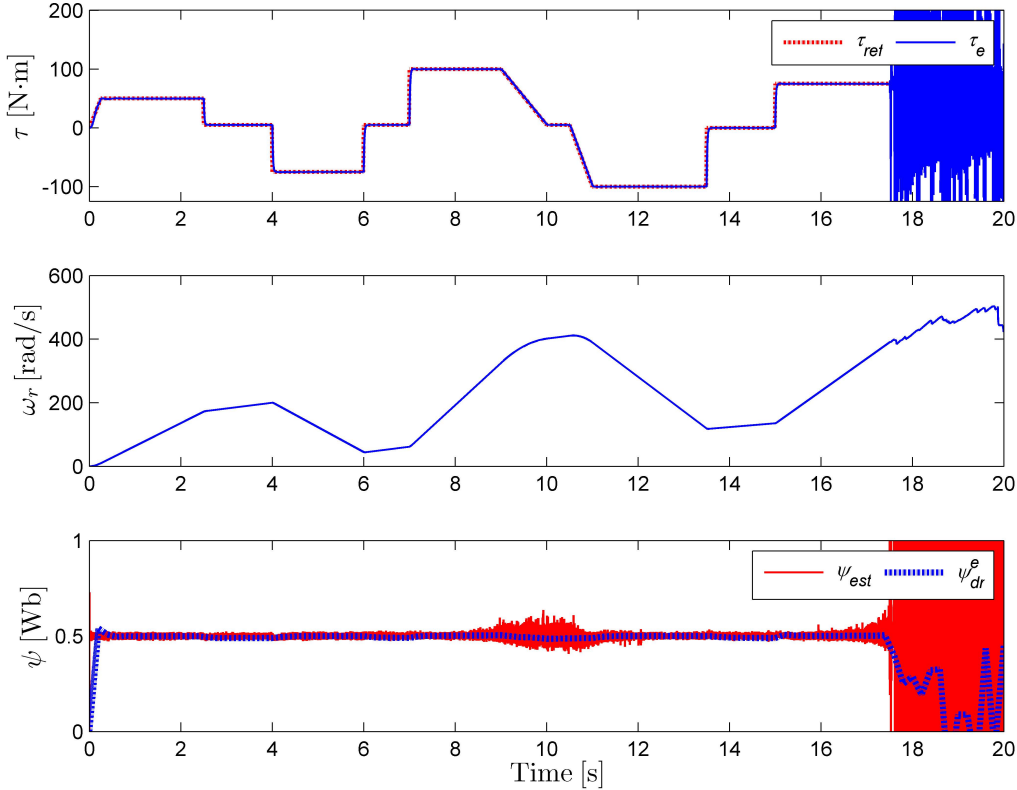

Figure 5.19: Simulation results – IFO torque controller without the flux controller
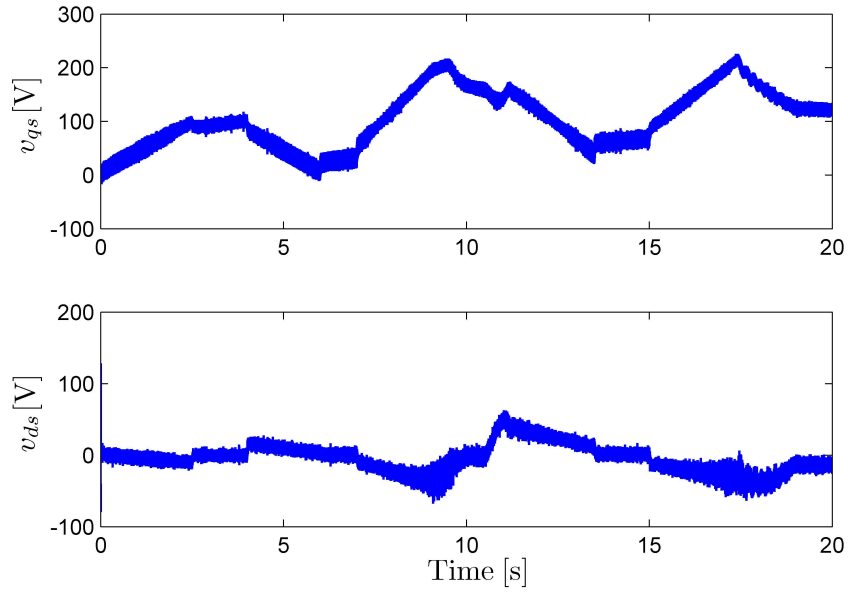
(a) With the flux controller
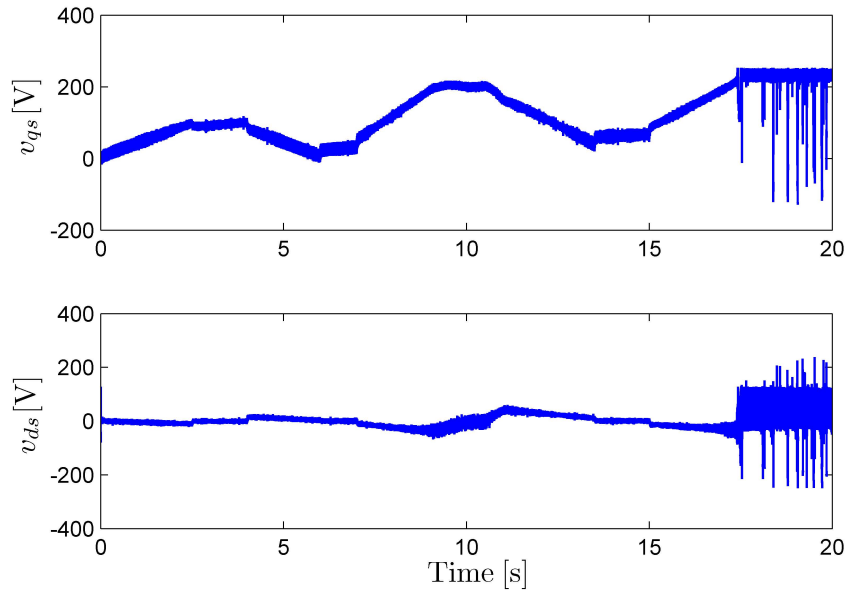
(b) Without the flux controller

Figure 5.20: Applied stator voltages during the IFO torque controller simulations

Chapter 6

Electric Vehicle System Model

In this chapter, the MapleSim vehicle dynamics model and electrical powertrain components that have been developed in the previous chapters are assembled in Simulink to create the full electric vehicle system. Different reference speed profiles, such as an urban driving schedule, a federal test driving schedule, and a high acceleration aggressive driving schedule are used to verify that the developed electric vehicle system model can simulate different driving scenarios.

6.1   Modelling the electric vehicle

To implement the electric vehicle system, the developed Simulink and MapleSim components from Chapter 3 to Chapter 5 are integrated as one system, and the electric vehicle system model is shown in Figure 6.1. The following section reviews the main components that were developed in the previous chapters.

Figure 6.1: Electric vehicle system model

6.1.1 Vehicle dynamics model

In Chapter 3, the Simulink longitudinal vehicle dynamics model and the high-fidelity MapleSim vehicle dynamics model were developed, and their simulation results were compared against each other to verify that the simulation results are similar. The high-fidelity MapleSim 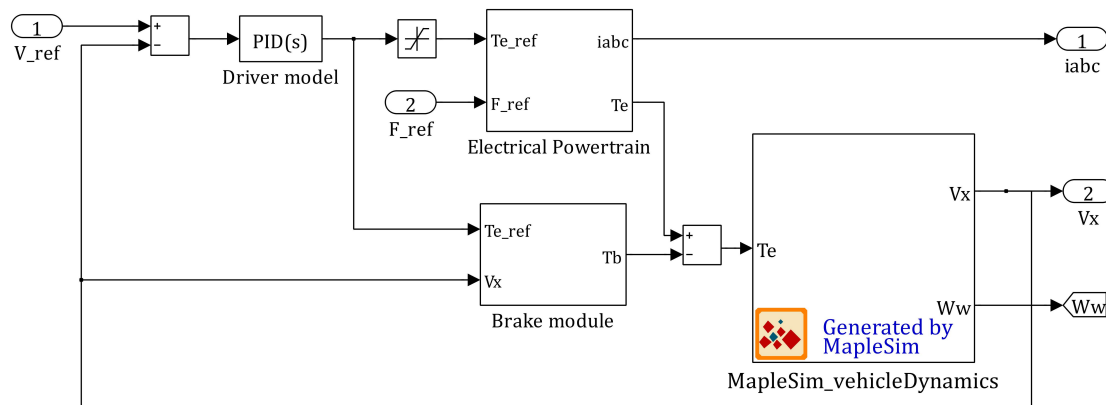model is exported as a Simulink component using a MapleSim Simulink component generation worksheet, so that it can be used in Simulink with the motor controllers developed in Simulink.
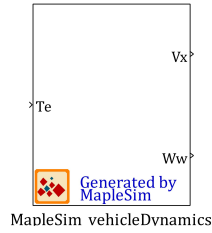
Figure 6.2: MapleSim vehicle dynamics model exported as a Simulink block

The input and outputs of the high-fidelity MapleSim vehicle dynamics model are shown in Figure 6.2. τ_e is the motor input torque coming from the AC induction motor component. The outputs are the vehicle's longitudinal speed v_x and the front wheel's angular speed ω_w which will be used as feedback signals. The complete list of vehicle dynamics parameters were listed in Table 2.2

6.1.2 Electrical powertrain components and controls

In Chapter 4, the development of the AC induction motor model in the synchronously rotating reference frame was explained in detail. The MapleSim model is exported as a Simulink component. Also, working principles of the 3-phase DC/AC PWM inverter were discussed, and the Simulink inverter model was developed.

AC induction motor

One minor modification is made to the AC induction motor model presented in Chapter 4. Previously the motor's angular speed ω_r is calculated using Equation (4.19), and it was one of the motor model's output variables. But, when the motor is mechanically connected to the front wheels, the angular speed of the front wheel should be proportional to the angular speed of the motor by the gear ratio. Thus, the motor's angular speed has become one of the input variables, and the motor's angular speed is calculated using the front wheel's angular speed feedback signal and the gear ratio.
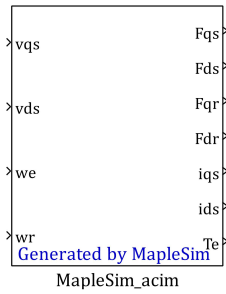
(a) MapleSim AC induction motor model
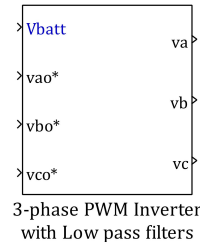
(b) Simulink 3-phase DC/AC inverter model

Figure 6.3: MapleSim and Simulink electrical powertrain component models

There are four input variables: the direct-quadrature components of the reference stator voltage (v_{ds} and v_{qs}), and the motor's synchronous and rotor speed (ω_e and ω_r). The output variables are: the stator and rotor flux linkages, the stator currents (F_{qs}, F_{ds}, F_{qr}, F_{dr}, i_{ds}, and i_{qs}), and the motor output torque τ_e. The input and output ports are shown in Figure 6.3(a).

3-phase DC/AC PWM inverter

The 3-phase DC/AC PWM inverter is used to convert the battery's DC voltage into 3-phase AC voltage signals which will be used by the AC induction motor model. The 3-phase PWM inverter's internal structure was shown in Section 4.2.2. The Simulink inverter model shown in Figure 6.3(b) displays the input and output variables. The input variables are the battery DC voltage, and the set of three control voltage signals (v_{ao}^*, v_{bo}^*, v_{co}^*). The output variables are the set of three inverted and filtered voltage signals (v_a, v_b, v_c).

Motor controllers

The main goal of the motor controller is to control the AC induction motor's output torque which will be delivered to the vehicle dynamics model. In Chapter 6, the three different motor control methods – open loop constant V/Hz speed control, IFO speed control, and IFO torque control – were explained and implemented in Simulink. The Simulink IFO torque controller block is shown in Figure 6.4(a), and it is used in the full electric vehicle system. There are four inputs to the IFO torque controller: the reference motor torque from the driver model, the motor torque and speed feedback signals, and the reference stator flux linkage. The output variables are: the reference stator voltages calculated from the IFO torque controller, and the estimated motor's

68

synchronous speed. The reference stator voltages in the d^e-q^e frame are converted to the 3-phase stationary signals, and they are used as the control signals for the 3-phase PWM inverter shown in Figure 6.3(b).

The Simulink electrical powertrain components discussed above are assembled into a single block to establish the electrical powertrain subsystem where the inputs are the reference motor torque and flux linkages, and the outputs are the motor terminal currents and the output torque produced by the AC induction motor.

(a) IFO torque controller　　　　(b) Electrical powertrain subsystem

Figure 6.4: Simulink IFO torque controller and electrical powertrain subsystem

All the powertrain components discussed previously are included in the electrical powertrain subsystem shown in Figure 6.5. The reference motor torque and flux linkages are processed by the motor controller which calculates the reference stator voltage required by the motor to produce a desired motor torque. The reference stator voltages are used by the 3-phase PWM voltage source inverter as its control signals to convert the battery DC voltage into AC voltage signals used by the induction motor.
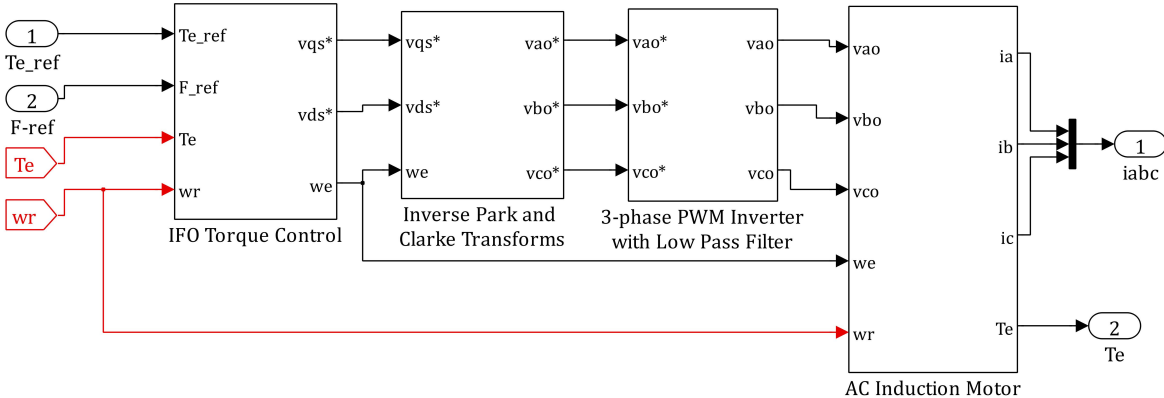
Figure 6.5: Inside the Simulink electrical powertrain component

6.2 Longitudinal driver model

A proportional-integral-derivative (PID) controller is used as a longitudinal driver model. The goal of the controller is to force the full electric vehicle's longitudinal speed to track a reference longitudinal speed. The PID controller processes the error between the reference speed and vehicle speed feedback signals, and calculates the reference motor torque as the output.
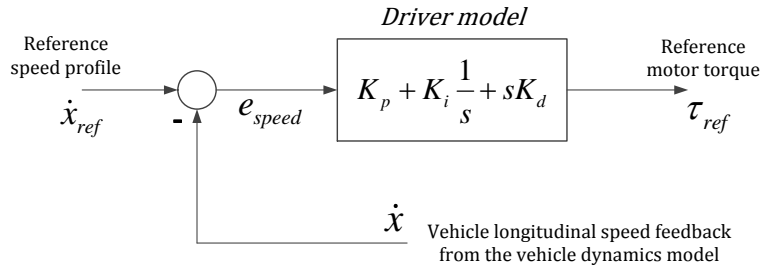
Figure 6.6: A PID longitudinal driver model

The control gains, mainly the proportional and integral gains, are manually tuned so that the error between the reference speed and actual vehicle speed is minimized. The complete electric vehicle system shown in Figure 6.1 with a simple ramp reference speed profile is simulated multiple iterations with different sets of PI control gains to find the set that resulted in the lowest speed error. The vehicle's longitudinal speed error responses for the different sets of PI control gains are plotted in Figure 6.7.
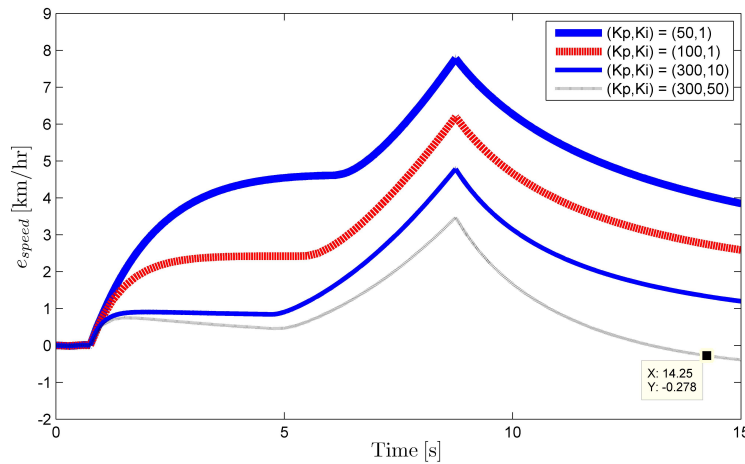
Figure 6.7: Vehicle speed error responses for the different sets of control gains

To tune the driver model's PI controller, the following set of PI gains, $K_p = 50$ and $K_i = 1$, is first used. The proportional gain is gradually increased until the vehicle speed error is minimized. Once the proportional gain is tuned, the integral gain is tuned to further minimize the vehicle speed error. However, increasing the integral gain excessively could result undesired undershoots or overshoots, so the gain is increased until no undershoots or overshoots are observed. For example, the vehicle speed error for the the following set of PI gains, $K_p = 300$ and $K_i = 50$, becomes negative near the steady-state speed which implies the vehicle response has overshoots as depicted in Figure 6.7.
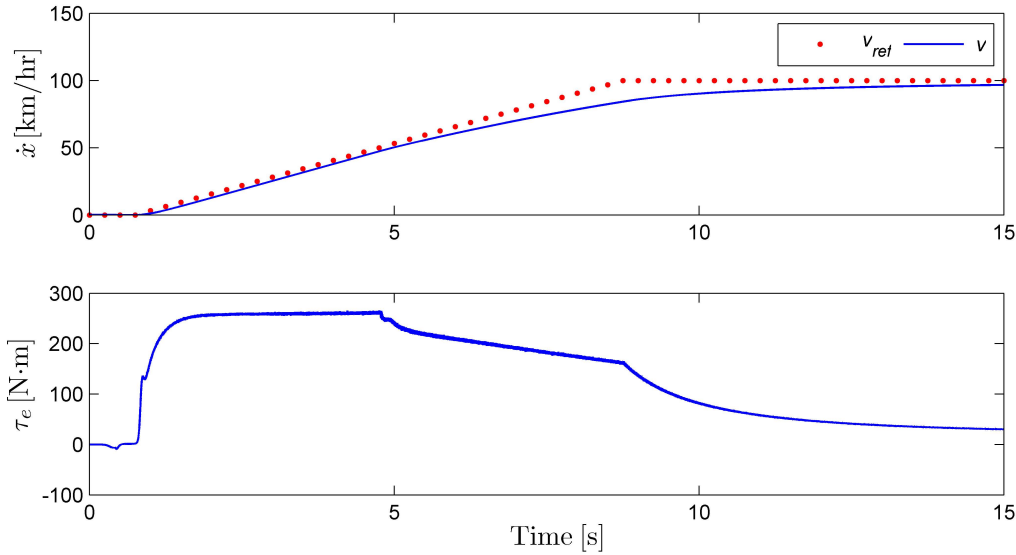
Figure 6.8: Simulation results – the vehicle model a ramp speed profile

The vehicle speed and motor torque responses for the control gains, $K_p = 300$ and $K_i = 10$, are plotted in Figure 6.8. The speed tracking response is satisfactory since the magnitude of speed error is small, and there are no overshoots that are seen from the response. The motor's field weakening region is seen from the torque response. The motor torque gradually decreases starting from around 5 seconds even though the rate of reference speed is increasing. This is due to the field weakening effect which causes the motor torque to decrease gradually when its speed is faster than the motor's base speed.

6.3 Brake module

In an electric vehicle, there are two sources of braking torque. A mechanical brake system provides braking torque at a wheel once a brake pedal is pressed by a driver. An electric motor can be operated as a generator to provide braking torque from the motor. This is called regenerative braking since kinetic and thermal energy that would have been dissipated by a mechanical brake can be recaptured as electrical energy by the electric motor and stored in the traction battery. To optimize an electric vehicle's energy efficiency, the regenerative brake system operates simultaneously with a mechanical brake system or operates as a standalone brake system to slow down a vehicle.

Implementing the regenerative brake system is simple since the developed AC induction motor model can be operated as a generator. When the driver model detects that a vehicle is decelerating, the reference motor torque calculated from the driver model would be negative since the feedback vehicle speed is greater than the reference speed. Using the vehicle's deceleration and reference motor torque values, the brake module splits required brake torque between the mechanical brake system and AC induction motor. For example, if a vehicle is decelerating at a slow rate, and the reference motor torque is smaller than the motor's maximum regenerative braking torque, then only the regenerative brake system is used to slow down a vehicle. For emergency braking situations where the deceleration rate is greater than a preset maximum deceleration rate, the regenerative brake system becomes inactive, and the mechanical brake system is only used to provide braking torque. Table 6.1 explains the operating principles of the mechanical and regenerative brake systems.

Table 6.1: Operating principles of the mechanical and regenerative brake systems

Is $\tau_{ref} < \tau_{regen_{max}}$?	Is $a_{decel} < a_{decel max}$?	Operation mode
Yes	Yes	Regenerative braking
Yes	No	N/A
No	Yes	Regenerative braking Mechanical braking
No	No	Mechanical braking

The mechanical and regenerative brake systems can be expanded by introducing different levels of the deceleration rate where they are used to divide the mechanical and regenerative braking torque proportion. For example, when the vehicle is decelerating at a fast rate, the mechanical brake system should provide most of braking torque while the regenerative brake system is active to provide limited braking torque to recapture

some amount of electrical energy. The complete electric vehicle shown in Figure 6.1 is simulated with a decelerating reference speed profile to observe the mechanical and regenerative brake system behaviours. For the first simulation, the vehicle is travelling at a constant 40 km/hr, and it is decelerated to 30 km/hr in 5 seconds. The motor's maximum regenerative torque is set to -50 N·m which is determined from the Toyota Rav4 EV's experimental data shown in Section 6.4. The reference motor torque calculated from the driver model is smaller than the motor's maximum regenerative torque, so the mechanical brake system is inactive as seen from the second plot of Figure 6.9.
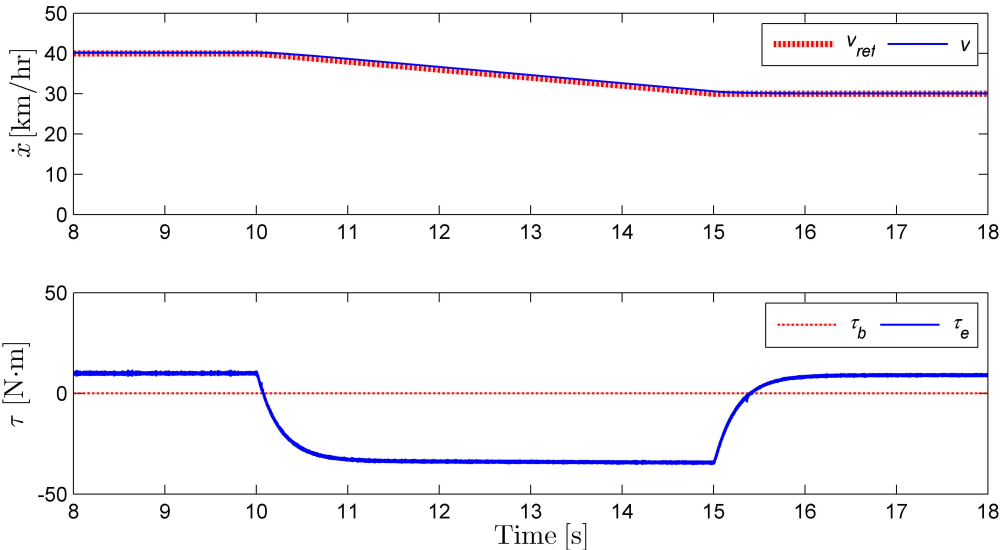
Figure 6.9: Simulation results – the vehicle model with slow deceleration

The second simulation is performed with a faster deceleration rate to show the regenerative brake system is working simultaneously with the mechanical brake system. The reference motor torque calculated from the driver model is greater than the motor's maximum regenerative torque which indicates that the motor is not capable of delivering braking torque by itself, so the mechanical brake system becomes active to deliver the rest of braking torque. The total braking torque required to track the reference speed profile on Figure 6.10 is about -110 N·m, so the regenerative brake system delivers -50 N·m while the mechanical brake system provides -60 N·m.

Figure 6.10: Simulation results – the vehicle model with fast deceleration

6.4 Experimental model validation

The reference vehicle, the Toyota Rav4 EV, is driven for different driving scenarios to collect experimental data which is used to validate the developed component models from the previous chapters. The reference vehicle has electronic control units (ECU) to control and manage its powertrain components. All the individual powertrain components, such as the traction battery and electric motor, and the inverter, are controlled by the ECUs provided by Tesla Mo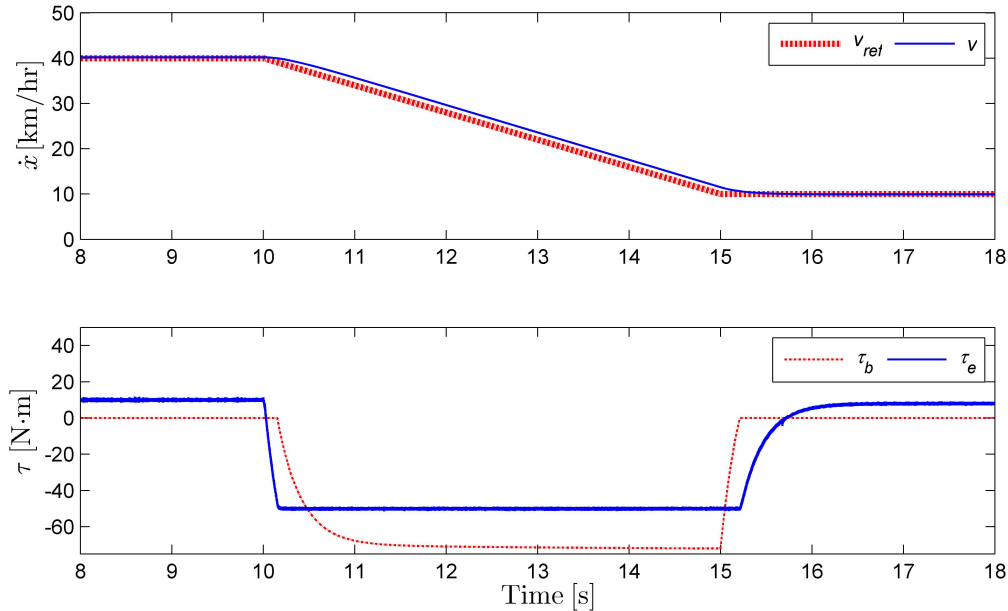tors, and the ECUs are inter-connected by the EV CAN bus as depicted in Figure 6.11. The Toyota's power management ECU controls the overall vehicle's power management, and the EV gateway ECU connects the Toyota ECU and the Tesla Motors ECUs. The EV CAN bus access point, DLC-R as depicted in the figure, is located at the rear of the vehicle which can be physically accessed to collect experimental powertrain data. The vehicle's electrical powertrain data is collected using bus interface and data logger called the Vector CANcaseXL. A portable computer is connected to the CANcaseXL via a USB cable, and the CANcaseXL is connected to the EV CAN bus access point. Raw collected data from the CAN bus requires decoding, and *Chris Shum* who is the research engineer in the Motion Research Group in the department of System Designs Engineering of the University of Waterloo has decoded the CAN bus messages. The detailed CAN bus decoding work is presented
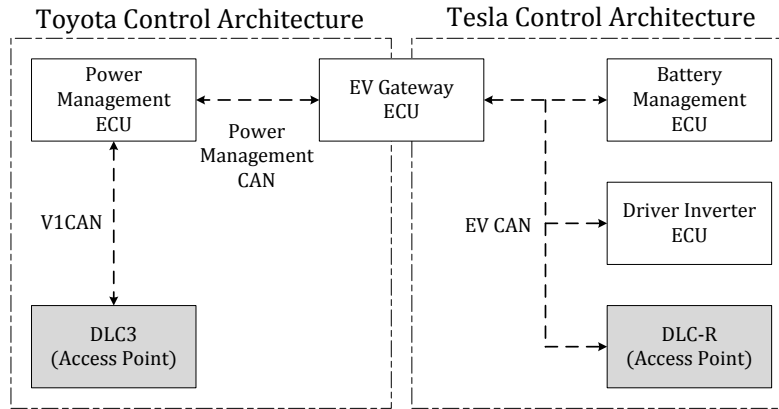
by C. Shum [48].

Figure 6.11: Toyota Rav4 EV control architecture

At the time of the Toyota Rav4 EV's vehicle experiment, the below variables from the EV CAN bus data are identified and scaled to engineering units.

- Vehicle's longitudinal speed [m/s]

- Motor speed [rad/s]

- Motor torque [N·m]

- Battery State-of-charge (SOC)

The vehicle testing was conducted on a test track at Toyota Motor Manufacturing Canada Inc. (TMMC) located in Cambridge, Ontario. The main focus of the vehicle testing was to collect the EV CAN bus data for various driving scenarios presented in Table 6.2. The experimental data collected from the coast down test is used to identify unknown vehicle dynamics parameters whereas the data collected from the acceleration and braking tests is used to validate and tune the developed AC induction motor model. The Toyota Rav4 EV has two drive modes: Normal and Sport. If the Sport mode is selected, the induction motor's maximum torque becomes higher compared to the case when the Normal mode is pressed. Also, there are two gear shift lever positions for the forward movement. Setting the gear shift lever to B allows the regenerative brake system to operate more frequently than setting the shift lever to D. During the acceleration test, a driver was instructed to press a brake pedal to hold the vehicle from moving, and switch his or her foot to an accelerator pedal quickly and press it at full throttle to accelerate the vehicle.

Table 6.2: Vehicle test plans for the TMMC vehicle testing

Test type	Drive mode	Gear shift lever position	Speed [km/hr]	# of iterations
Coast down test	Normal	D	100 - 0	5
	Normal	D	70 - 40	5
Braking test	Normal	B	60 - 0	5
	Sport	D	80 - 0	5
Acceleration test	Normal	D	0 - 80	5
	Sport	D	0 - 120	5

The Toyota Rav4 EV's experimental motor torque-speed curves are plotted in Figure 6.12. Multiple torque-speed curves are plotted using the measured motor data from a number of acceleration tests. Each of the torque-speed curves are slightly different since the acceleration's magnitude for each trial is not exactly the same.
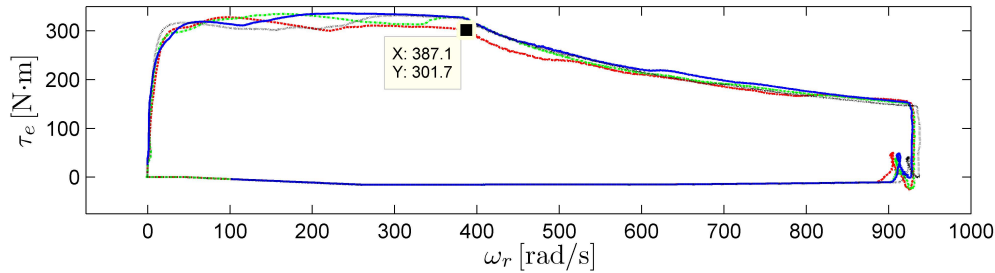
(a) Torque-speed curves using the data from the acceleration test
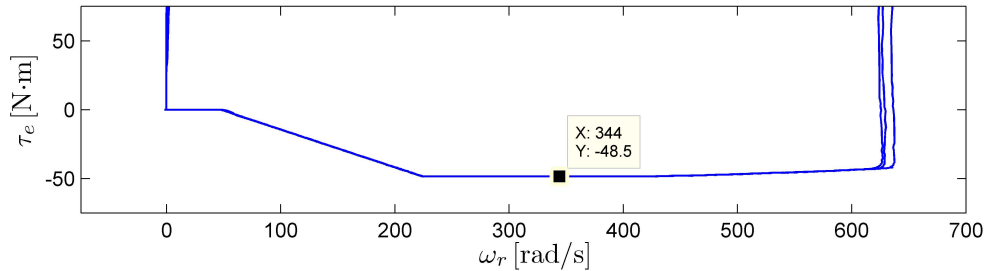
(b) Torque-speed curves using the data from the gentle braking test

Figure 6.12: Toyota Rav4 EV motor torque-speed curves from the experiments

From the torque-speed curves from the acceleration test, it can be seen that the field weakening regions for all the curves start at approximately the same motor speed. The gradual decrease in the motor torque starts at the motor's base or rated speed which is found to be 387 rad/s (61.6 Hz). In Chapter 4 and Chapter 5, the assumed base speed, 60 Hz, was used to simulate the AC induction motor. The simulations results

76

from Chapter 4 and Chapter 5 are still valid since the actual and assumed base speeds are very close. The maximum regenerative braking torque is found from the measured motor data from the braking tests listed in Table 6.2. The braking tests are divided for slow and fast deceleration braking cases. For the set of slow deceleration braking tests, the shift lever is set to B, and a brake pedal is pressed gently to maximize the usage of regenerative braking. The torque-speed curves for the slow deceleration braking tests are plotted in Figure 6.12(b) to find the maximum regenerative braking torque. From the torque-speed curves, the minimum developed motor torque is found to be -48.5 N·m, which is the maximum regenerative torque. Using the identified parameters from the experiments, the electric vehicle system shown in Figure 6.1 is simulated to collect the simulation results, and they are compared against the data collected from the vehicle testing.
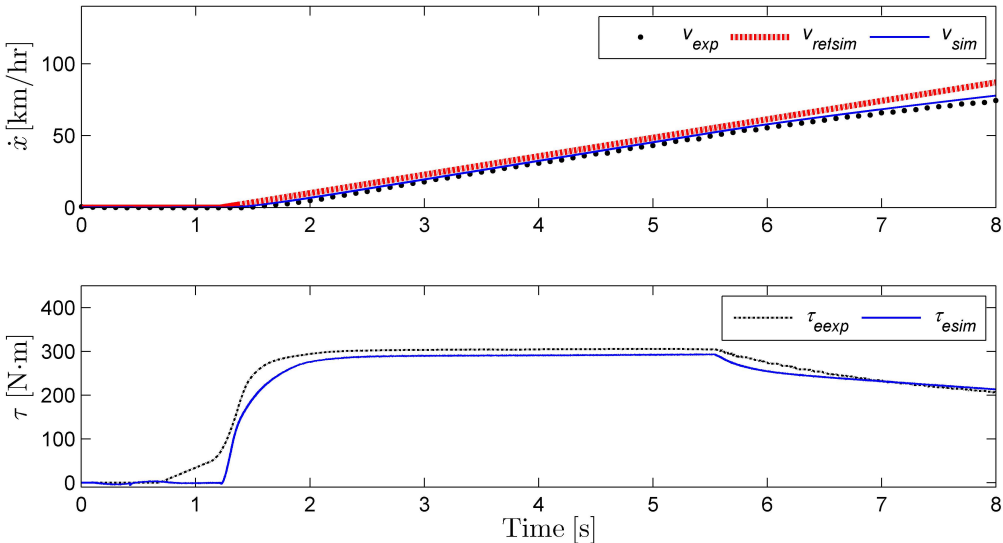
Figure 6.13: Comparison of the simulation and experimental results

Figure 6.13 shows a comparison of the simulation and experimental data. The reference speed profile v_{refsim} is generated so that the simulation vehicle speed v_{sim} becomes similar to the experimental vehicle speed v_{exp} profile. From the torque response plot, the experimental motor torque τ_{eexp} response has a positive magnitude even though the vehicle remains stationary. During the vehicle testing, the brake pedal was pressed to stop the vehicle from creeping forward. Even though the electric vehicle does not have an automatic transmission, the vehicle creeps forward when the accelerator is not pressed. This means that the motor provides a small amount of positive torque even

though the accelerator is not pressed, so that the electric vehicle behaves like a typical automatic vehicle. The experimental motor torque response and the simulation motor torque response τ_{esim} are similar in shape and magnitude, but, the rate of torque decrease in the field weakening region is different between the two data sets. In the experimental results the torque response decreases at a faster rate than the simulation torque response. The gain K_f in Equation (5.9) is gradually increased until the simulation torque response decreases at a similar rate in the field weakening region as the experimental torque response, and the corresponding simulation results are shown in Figure 6.14.
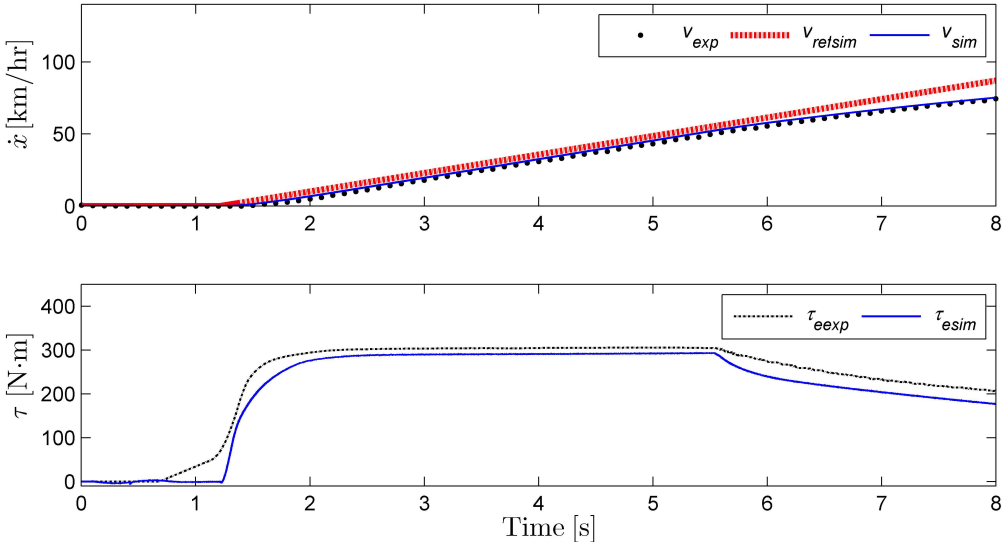
Figure 6.14: Comparison of the simulation and experimental results with modified parameters

6.5 Implementation and results

The Simulink components discussed in the previous sections are used to construct the full electric vehicle system, which was shown in Figure 6.1. There are three main subsystems included in the electric vehicle system model: the vehicle dynamics subsystem, the electrical powertrain subsystem, and lastly the brake module. The driver model is included in the system to track the reference speed profile.

The electric vehicle system's inputs are the reference speed profile and constant flux linkage listed in Table 5.1, and the outputs are the vehicle's longitudinal speed

and the motor's three-phase terminal currents. The electrical powertrain subsystem consists of the IFO torque controller, the 3-phase PWM voltage source inverter, and the AC induction motor. Its inputs are the reference motor torque calculated from the driver model, and the reference flux linkage. The subsystem's outputs are the developed motor torque and the motor's three phase currents. When the mechanical brake system becomes active for high deceleration situations, the brake module generates braking torque which is subtracted from the motor output torque, and the resultant torque is applied to the vehicle dynamics model. The vehicle dynamics subsystem processes the inputs from the electrical powertrain subsystem and the brake module, and the outputs are the vehicle's longitudinal speed and the front wheel speed.

The reference speed profiles are the driving cycle tests conducted by the US Environmental Protection Agency (EPA). Different driving cycles were standardized by the EPA to measure tailpipe emissions and fuel economy of passenger vehicles and trucks. The following EPA's city and highway driving cycles are used to simulate the electric vehicle system [49].

- The urban dynamometer driving schedule (UDDS)

- The federal test procedure (FTP-75)

- The highway fuel economy driving schedule (HWFET)

- The high acceleration and aggressive driving schedule (US06).

The first and second driving cycles represent city driving conditions where a vehicle is operating in a low speed range and encounters frequent stop-and-go situations. The third driving cycle represents highway driving conditions where a vehicle is travelling at around 100 km/hr without stopping. The last driving cycle represents high acceleration and aggressive driving conditions where a vehicle is accelerated rapidly and stops aggressively. The four driving schedules are plotted in Figure 6.15.

The simulation results for the UDDS driving cycle are shown in Figure 6.16 and Figure 6.17. From Figure 6.16, it can be seen that the vehicle tracks the reference speed profiles precisely throughout the entire driving cycle. When the vehicle is decelerating, the regenerative and mechanical brake systems are simultaneously active to provide negative braking torque as depicted in the second plot. To study the simulation results thoroughly, Figure 6.17 shows the simulation results between 400 and 600 seconds. By examining the close-up view of the simulation results it is clear to see that the vehicle tracks the reference speed profile very well, and there are no overshoots or undershoots
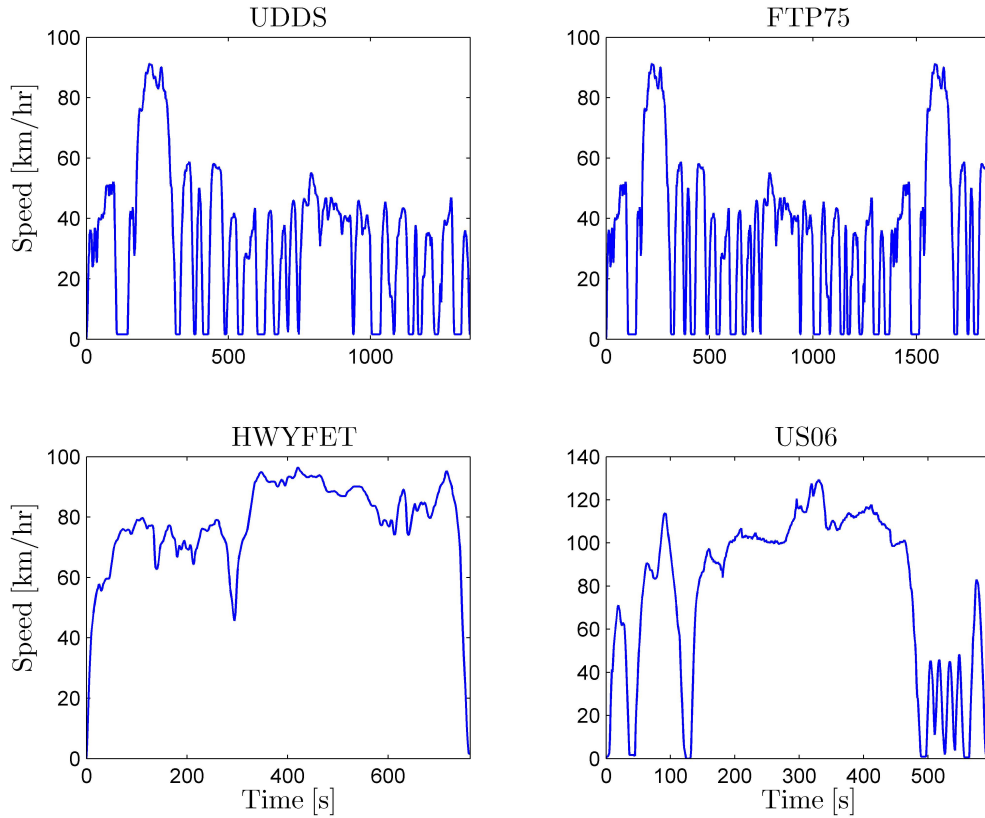
Figure 6.15: Reference speed profiles used in the electric vehicle simulations

in the vehicle speed response. Also, from the current response plotted in the Figure 6.17, one phase of the motor currents i_a is in accordance with the developed motor torque response. For example, as the magnitude of the developed motor torque increases, the magnitude and frequency of the current response increase.

The simulation results for the FTP75 driving cycle are shown in Figure 6.18 and Figure 6.19. The UDDS and FTP75 driving cycles are very similar, but the FTP75 driving cycle has an additional high speed profile near the end of its driving cycle. Similar to the UDDS driving cycle simulation, the vehicle tracks the reference speed profiles precisely throughout the entire FTP75 driving cycle. Figure 6.19 shows the simulation results between 700 and 1000 seconds. By examining the close-up view of the simulation results it is clear to see that the vehicle tracks the reference speed profile very well, and there are no overshoots or undershoots in the vehicle speed response.

The highway driving cycle's (HWYFET) simulation results are shown in Figure 6.20. Similar to the two city driving cycles' simulation results, the vehicle follows the reference
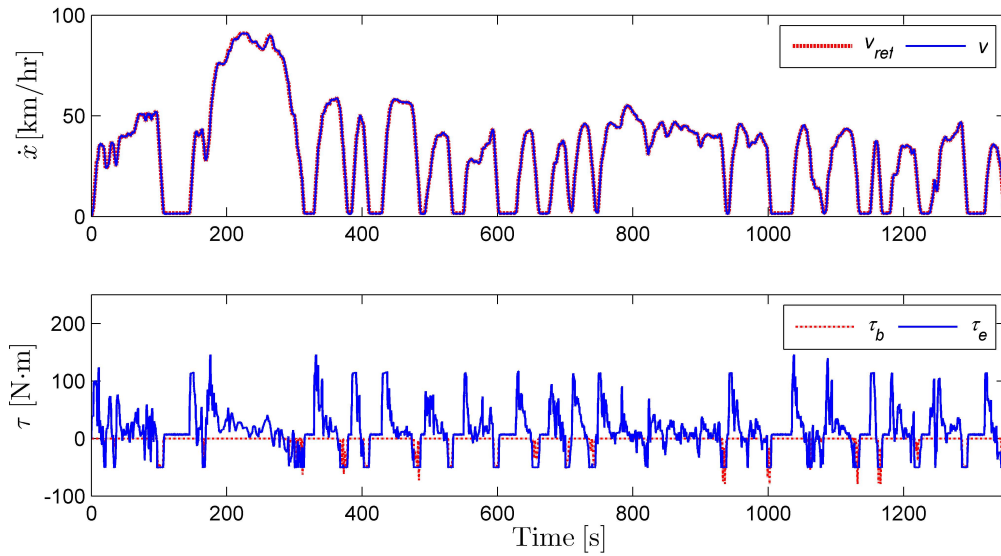
Figure 6.16: Simulation results – UDDS driving cycle

speed closely. When the vehicle is cruising at a high speed, the developed motor torque remains small, which is an expected result. The high acceleration and aggressive driving cycle's (US06) simulation results are shown in Figure 6.21. Near the end of the US06 driving cycle, the reference speed profile resembles a trapezoidal wave with a steep slope. The close-up view is shown in Figure 6.22 to examine the simulation results near the end of the driving cycle. The vehicle undergoes high acceleration followed by high deceleration, and the developed motor torque reaches about 200 N·m. The mechanical brake system provides most of the braking torque when the vehicle is decelerating at a high rate. By examining the simulation results of the four driving cycles, it can be seen that the developed electric vehicle system handles the different driving scenarios well, and the system works properly under different driving scenarios.

Figure 6.17: Simulation results – close-up view of UDDS driving cycle
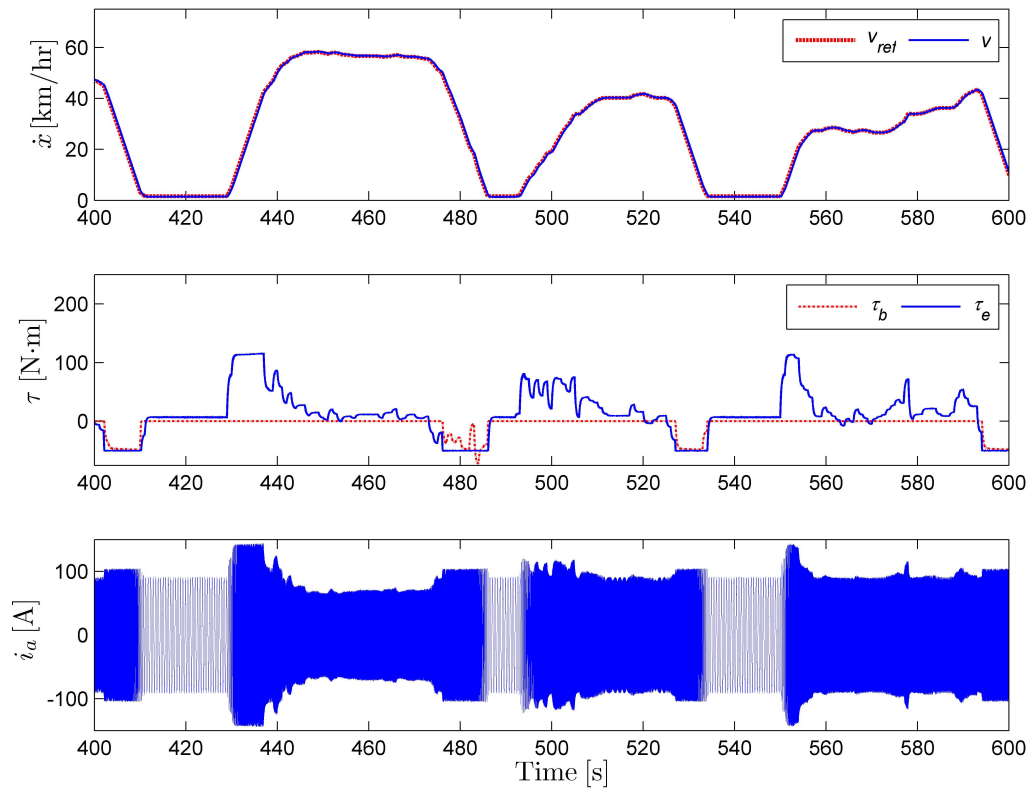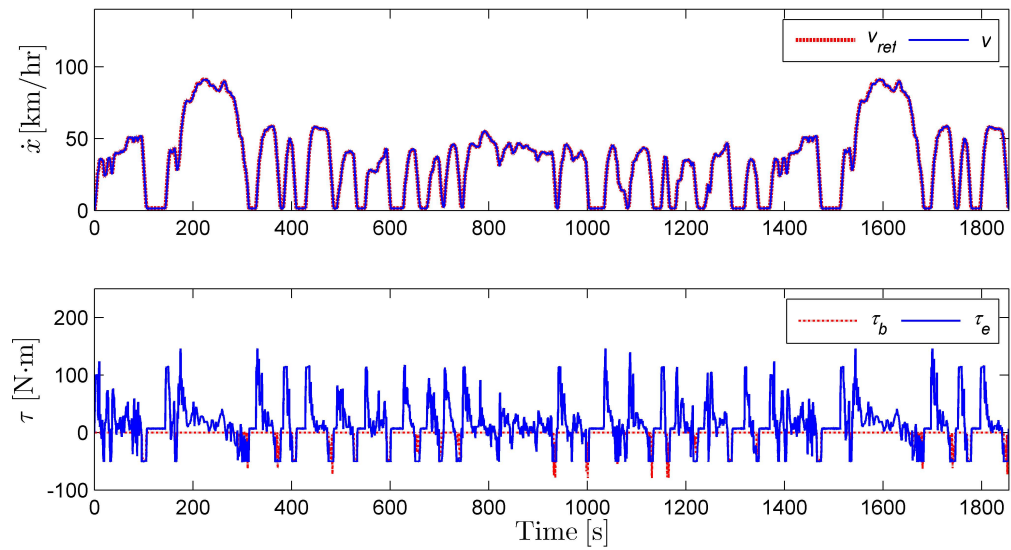

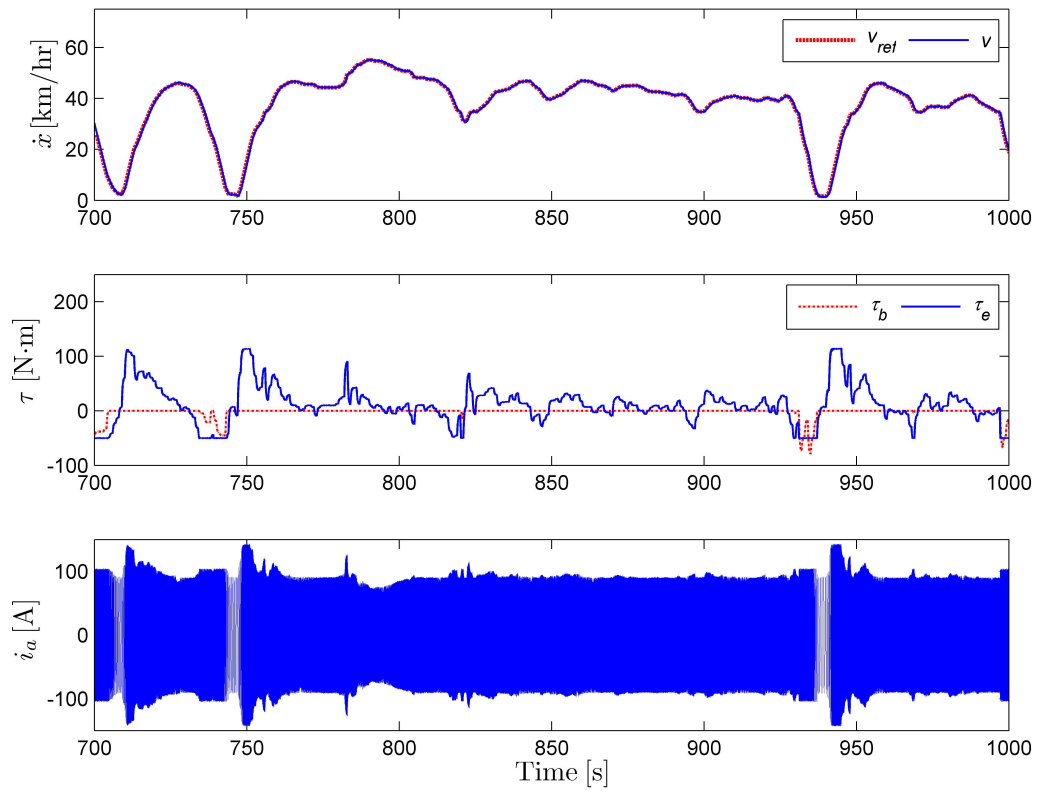Figure 6.18: Simulation results – FTP75 driving cycle

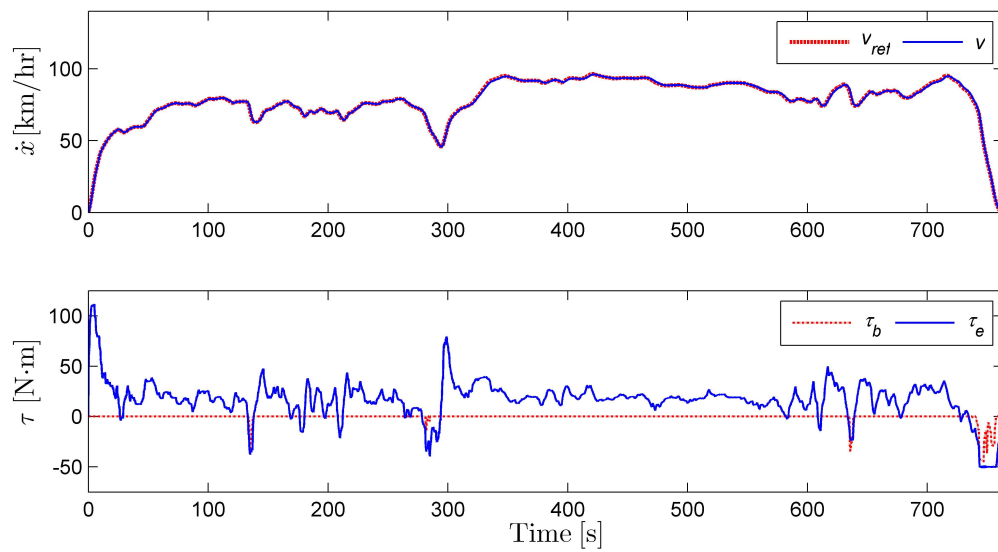Figure 6.19: Simulation results – close-up view of FTP75 driving cycle

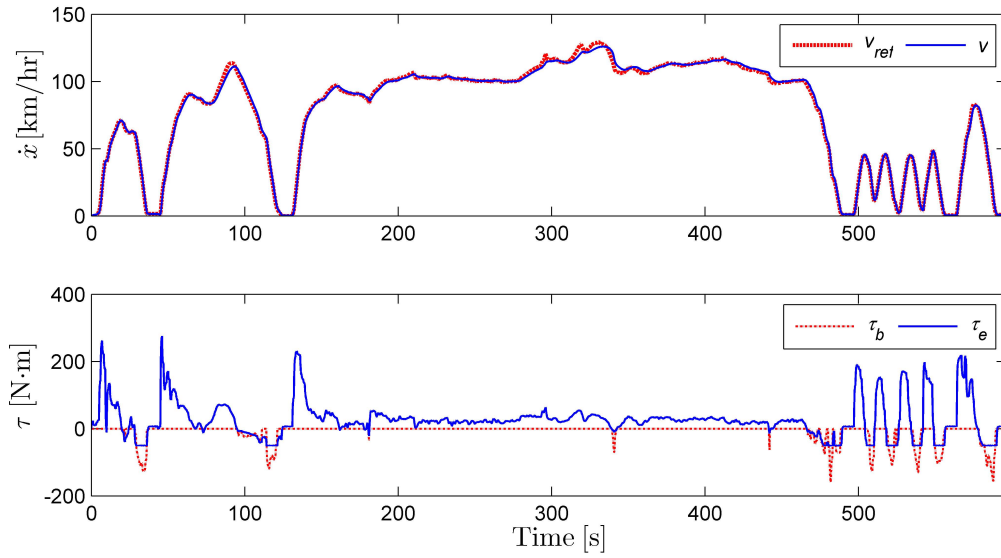

Figure 6.20: Simulation results – HWYFET driving cycle

83
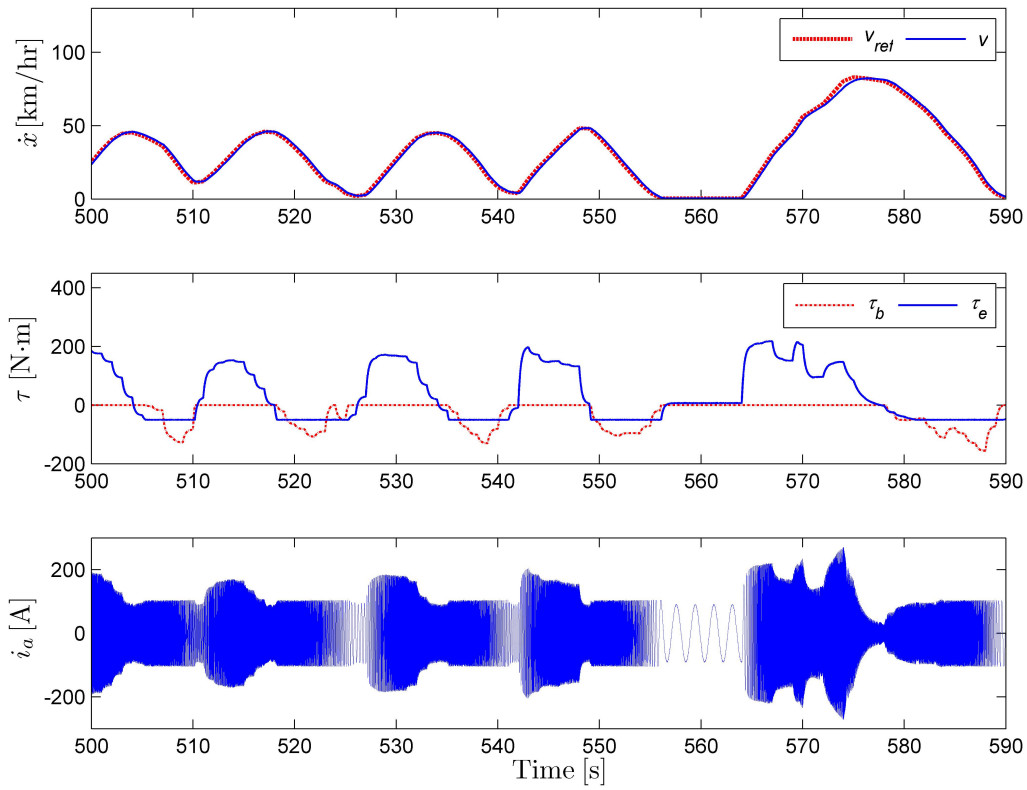
Figure 6.21: Simulation results – US06 driving cycle

Figure 6.22: Simulation results – close-up view of US06 driving cycle

Chapter 7

Conclusions

In this work, a high fidelity electric vehicle model has been developed in the modelling and simulation environments, and the simulation results obtained from the high-fidelity AC induction motor model were compared against experimental motor data collected from vehicle testing using the reference electric vehicle, the Toyota Rav4 EV. The developed high-fidelity electric vehicle model is comprised of two main subsystems: the high-fidelity vehicle dynamics model developed using MapleSim, and the high-fidelity electrical powertrain models consisting of the AC induction motor, the 3-phase DC/AC voltage source inverter, and the motor controllers. Finally, the high-fidelity electric vehicle system has been simulated for different driving scenarios to verify that the developed vehicle model is capable of operating under different driving scenarios.

The high-fidelity vehicle dynamics model was developed using the reference vehicle's mechanical specifications. In Chapter 3, the development of the high-fidelity MapleSim vehicle dynamics was explained in detail using the MapleSim components that were used to build the vehicle dynamics model in the user interface of MapleSim. A simple vehicle dynamics model was developed in Simulink using the FBD of a front-wheel driven vehicle and drivetrain dynamics including tire dynamics. The MapleSim vehicle dynamics and Simulink vehicle dynamics models were simulated using the same reference speed input and control gains, and the simulation results, such as the vehicle's longitudinal speed, wheel torque, and front tire normal forces, from the two models were compared and verified that the results are comparable.

The high-fidelity powertrain components found in the reference vehicle were developed next. Using the dynamic d-q equivalent circuit of the AC induction motor and the synchronously rotating reference frame, d^e-q^e, explained in Chapter 4, the AC induction motor's dynamic equations were derived. The AC induction motor model was

developed based on the d^e-q^e frame because R.H Park [26] and G. Kron [3] showed that the time-varying inductances can be eliminated from the motor's voltage equations, and the resulting motor variables, such as voltages, currents, and flux linkages, are in terms of DC quantities. Since the developed motor model was based on the d^e-q^e frame, the Park and Clarke transformations were used to convert the applied 3-phase voltage input signals into the two-phase synchronously rotating voltage signals. Using the derived dynamic equations listed in Section 4.1.4, the high-fidelity AC induction motor model was developed using a MapleSim custom component worksheet, and it was exported as a Simulink block to work with the motor controllers developed in Simulink. The developed motor model was simulated for a given 3-phase supply voltage, and its simulation results were studied and validated. Since the battery pack used in the reference vehicle provides DC power, the 3-phase PWM voltage source inverter was developed next. The voltage source inverter was developed because the developed AC induction motor was a voltage-based model.

The motor controllers were developed to control the motor speed or developed torque. Indirect field-oriented control originally presented by K. Hasses [5] was studied and implemented in Simulink to control the speed of the induction motor. The developed speed controller was then modified to control developed motor torque, and this controller was called the indirect field-oriented torque controller. The electrical powertrain subsystem was assembled by combining the AC induction motor model, the 3-phase PWM voltage source inverter, and the variable torque controller. The subsystem was simulated for different reference torque profiles, and the motor responses, such as the developed motor torque, terminal currents, and flux linkages, were studied and verified. At the time of the vehicle testing, the electrical powertrain data was recorded from the reference vehicle's CAN bus, and only the motor variables were identified and scaled. The developed AC induction motor parameter K_f was manually tuned using the experimental motor torque-speed curves. In Chapter 6, the electric vehicle system was created by combining the high fidelity MapleSim vehicle dynamics model with the electrical powertrain subsystem. The electric vehicle system was simulated for the city, highway, and aggressive driving schedules to verify that the vehicle system is capable of operating under different driving scenarios.

7.1   Contributions

The main contribution of this thesis is the development and implementation of the high-fidelity electric vehicle model in the modelling and simulation environments. The

key electrical powertrain components, which were the AC induction motor, the 3-phase PWM voltage source inverter, and the variable torque controller, were modelled, and the AC induction motor model was validated using the experimental data.

7.2   Future work

The electric vehicle is implemented and validated successfully in this thesis. Many areas in the electrical powertrain system, however, still have room for further improvement. The following approaches can be used to address some of those limitations and increase the overall accuracy of the models.

Traction battery and battery management system

The reference vehicle has lithium-ion battery packs to power the electrical powertrain system. A lithium-ion battery model was not included in the electric vehicle system, and instead a constant DC voltage was used. In MapleSim 7, different battery models are currently available, and with few modifications, a traction battery can be included in the electric vehicle system. A high-fidelity battery management system, however, will require extensive effort to implement. Brandl et al. [50] explained a general and flexible battery management system architecture for electric vehicles for lithium chemistry based batteries.

Improved AC induction motor model

The AC induction motor developed in this thesis used constant motor parameters, such as the stator and rotor's resistances and inductances. However, many motor parameters are dependent on the operating temperature, and should be modelled accordingly to ensure accurate simulation. Khalifa et al. [51] showed how the AC induction motor parameters vary when the motor's operating temperature increases. By including the effects of temperature on motor parameters, the dynamic response of the electric motor can be captured with greater detail and accuracy.

Improved 3-phase PWM voltage source inverter

The 3-phase PWM voltage source inverter developed in this thesis was built using the Simulink ideal switches. For an actual DC/AC power inverter, IGBTs are commonly used. Instead of using the ideal switches in Simulink, the next phase of development

of the 3-phase PWM voltage source inverter should incorporate the dynamics of IGBT switches.

Improved variable torque controller

The variable torque controller used in the electric vehicle model is designed by modifying the indirect field-oriented speed controller. The torque controller requires many feedback signals, such as developed motor torque, speed, and currents. The torque control design can be improved by implementing other control methods, such as direct torque control, which are known to use fewer feedback signals and offer comparable torque responses to vector control [32]. But, direct torque control generates flux and torque ripple which may be undesirable effects for electric vehicle applications [2].

Bibliography

[1] P. C. Krause, S. D. Sudhoff, and O. Wasynczuk, *Analysis of electric machinery.* IEEE Computer Society Press, 1995.

[2] B. K. Bose, *Modern Power Electronics and AC Drives.* Prentice Hall PTR, 2002.

[3] G. Kron, *Equivalent circuits of electric machinery.* J. Wiley & Sons, 1951.

[4] F. Blaschke, "The principle of field orientation as applied to the new transvektor closed-loop control system for rotating field machines," *Simens Review*, vol. 34, pp. 217–220, 1972.

[5] K. Hasse, *Zur Dynamik drehzahlgeregelter Antriebe mit stromrichtergespeisten Asynchron-kurzschlußläufermaschinen.* PhD thesis, Technische Hochschule Darmstadt, Germany, 1969.

[6] L. James and L. John, *Electric vehicle technology explained.* Wiley, 2003.

[7] D. E. Nye, *Electrifying America: Social meanings of a new technology.* MIT, 1990.

[8] C. Sulzberger, "An early road warrior: electric vehicles in the early years of the automobile," *Power and Energy Magazine, IEEE*, vol. 2, no. 3, pp. 66–71, 2004.

[9] M. Eshani, Y. Gao, S. E. Gay, and A. Emadi, "Modern electric, hybrid electric and fuel cell vehicles," *Fundamentals, Theory, and Design. Boca Raton, FL: CRC*, 2005.

[10] Z. M. Salameh, M. A. Casacca, and W. A. Lynch, "A mathematical model for lead-acid batteries," *Energy Conversion, IEEE Transactions on*, vol. 7, no. 1, pp. 93–98, 1992.

[11] A. Taniguchi, N. Fujioka, M. Ikoma, and A. Ohta, "Development of nickel/metal-hydride batteries for evs and hevs," *Journal of Power Sources*, vol. 100, no. 1, pp. 117–124, 2001.

[12] P. Rong and M. Pedram, "An analytical model for predicting the remaining battery capacity of lithium-ion batteries," *Very Large Scale Integration (VLSI) Systems, IEEE Transactions on*, vol. 14, no. 5, pp. 441–451, 2006.

[13] M. Chen and G. A. Rincon-Mora, "Accurate electrical battery model capable of predicting runtime and iv performance," *Energy conversion, IEEE transactions on*, vol. 21, no. 2, pp. 504–511, 2006.

[14] T.-S. Dao, C. P. Vyasarayani, and J. McPhee, "Simplification and order reduction of lithium-ion battery model based on porous-electrode theory," *Journal of Power Sources*, vol. 198, pp. 329–337, 2012.

[15] A. Seaman, T.-S. Dao, and J. McPhee, "A survey of mathematics-based equivalent-circuit and electrochemical battery models for hybrid and electric vehicle simulation," *Journal of Power Sources*, vol. 256, pp. 410–423, 2014.

[16] L. Lu, X. Han, J. Li, J. Hua, and M. Ouyang, "A review on the key issues for lithium-ion battery management in electric vehicles," *Journal of power sources*, vol. 226, pp. 272–288, 2013.

[17] C. Chan, "The state of the art of electric, hybrid, and fuel cell vehicles," *Proceedings of the IEEE*, vol. 95, no. 4, pp. 704–718, 2007.

[18] J. Larminie, A. Dicks, and M. S. McDonald, *Fuel cell systems explained*, vol. 2. Wiley New York, 2003.

[19] S. Aso, M. Kizaki, and Y. Nonobe, "Development of fuel cell hybrid vehicles in toyota," in *Power Conversion Conference-Nagoya, 2007. PCC'07*, pp. 1606–1611, IEEE, 2007.

[20] V. Gupta and A. Deb, "Speed control of brushed dc motor for low cost electric cars," in *Electric Vehicle Conference (IEVC), 2012 IEEE International*, pp. 1–3, IEEE, 2012.

[21] P. Pillay and R. Krishnan, "Modeling, simulation, and analysis of permanent-magnet motor drives. i. the permanent-magnet synchronous motor drive," *Industry Applications, IEEE Transactions on*, vol. 25, no. 2, pp. 265–273, 1989.

[22] L. Zhong, M. F. Rahman, W. Y. Hu, and K. Lim, "Analysis of direct torque control in permanent magnet synchronous motor drives," *Power Electronics, IEEE Transactions on*, vol. 12, no. 3, pp. 528–536, 1997.

[23] M. Kamiya, "Development of traction drive motors for the toyota hybrid system," *IEEJ Transactions on Industry Applications D*, vol. 126, no. 4, p. 473, 2006.

[24] R. Lee, P. Pillay, and R. Harley, "D, q reference frames for the simulation of induction motors," *Electric power systems research*, vol. 8, no. 1, pp. 15–26, 1984.

[25] H. C. Stanley, "An analysis of the induction machine," *Electrical Engineering*, vol. 57, no. 12, pp. 751–757, 1938.

[26] R. H. Park, "Two-reaction theory of synchronous machines generalized method of analysis-part i," *American Institute of Electrical Engineers, Transactions of the*, vol. 48, no. 3, pp. 716–727, 1929.

[27] B. Ozpineci and L. M. Tolbert, "Simulink implementation of induction machine model-a modular approach," in *Electric Machines and Drives Conference, 2003. IEMDC'03. IEEE International*, vol. 2, pp. 728–734, Ieee, 2003.

[28] Y.-R. Kim, S.-K. Sul, and M.-H. Park, "Speed sensorless vector control of induction motor using extended kalman filter," *Industry Applications, IEEE Transactions on*, vol. 30, no. 5, pp. 1225–1233, 1994.

[29] T. Ohtani, N. Takada, and K. Tanaka, "Vector control of induction motor without shaft encoder," *Industry Applications, IEEE Transactions on*, vol. 28, no. 1, pp. 157–164, 1992.

[30] D.-C. Lee, S.-K. Sul, and M.-H. Park, "High performance current regulator for a field-oriented controlled induction motor drive," *Industry Applications, IEEE Transactions on*, vol. 30, no. 5, pp. 1247–1257, 1994.

[31] C. Lascu, I. Boldea, and F. Blaabjerg, "A modified direct torque control for induction motor sensorless drive," *Industry Applications, IEEE Transactions on*, vol. 36, no. 1, pp. 122–130, 2000.

[32] I. Takahashi and Y. Ohmori, "High-performance direct torque control of an induction motor," *Industry Applications, IEEE Transactions on*, vol. 25, no. 2, pp. 257–264, 1989.

[33] S. Dilmi and S. Yurkovich, "Nonlinear torque control of the induction motor in hybrid electric vehicle applications," in *American Control Conference, 2005. Proceedings of the 2005*, pp. 3001–3006, IEEE, 2005.

[34] T. Kataoka, Y. Sato, and A. Bendiabdellah, "A novel volts/hertz control method for an induction motor to improve the torque characteristics in the low speed range," in *Power Electronics and Applications, 1993., Fifth European Conference on*, pp. 455–458, IET, 1993.

[35] C. Szabo, I. Incze, and M. Imecs, "Voltage-hertz control of the synchronous machine with variable excitation," in *Automation, Quality and Testing, Robotics, 2006 IEEE International Conference on*, vol. 1, pp. 298–303, IEEE, 2006.

[36] S. Boschert, *Plug-in hybrids: The cars that will recharge America*. New Society Publishers, 2006.

[37] Toyota, "2012 rav4 ev brochure," 2012.

[38] Toyota, "Toyota technical information system," 2015.

[39] R. N. Jazar, *Vehicle dynamics: theory and application*. Springer, 2008.

[40] H. Pacejka, *Tire and vehicle dynamics*. Elsevier, 2005.

[41] A. M. Trzynadlowski, *Control of induction motors*. Academic Pr, 2001.

[42] W. Duesterhoeft, M. W. Schulz, and E. Clarke, "Determination of instantaneous currents and voltages by means of alpha, beta, and zero components," *American Institute of Electrical Engineers, Transactions of the*, vol. 70, no. 2, pp. 1248–1255, 1951.

[43] M. Mirošević, "The dynamics of induction motor fed directly from the isolated electrical grid," *INTECH Open Science Open Mind*, 2012.

[44] S. Chapman, *Electric machinery fundamentals*. Tata McGraw-Hill Education, 2005.

[45] R. C. Dorf and J. A. Svoboda, *Introduction to electric circuits*. John Wiley & Sons, 2010.

[46] R. P. Sallen and E. L. Key, "A practical method of designing rc active filters," *Circuit Theory, IRE Transactions on*, vol. 2, no. 1, pp. 74–85, 1955.

[47] R. S. Hiware and J. G. Chaudhari, "Indirect field oriented control for induction motor," in *Emerging Trends in Engineering and Technology (ICETET), 2011 4th International Conference on*, pp. 191–194, IEEE, 2011.

[48] C. Shum, "Toyota rav4 ev: Reverse engineering and control system modification," tech. rep., University of Waterloo, 2014.

[49] EPA, "Vehicle chassis dynamometer driving schedules," tech. rep., United States Environmental Protection Agency (EPA), 2013.

[50] M. Brandl, H. Gall, M. Wenger, V. Lorentz, M. Giegerich, F. Baronti, G. Fantechi, L. Fanucci, R. Roncella, R. Saletti, *et al.*, "Batteries and battery management systems for electric vehicles," in *Proceedings of the Conference on Design, Automation and Test in Europe*, pp. 971–976, EDA Consortium, 2012.

[51] F. Khalifa, S. Serry, M. Ismail, and B. Elhady, "Effect of temperature rise on the performance of induction motors," in *Computer Engineering & Systems, 2009. ICCES 2009. International Conference on*, pp. 549–552, IEEE, 2009.